UiT
THE ARCTIC UNIVERSITY OF NORWAY

FACULTY OF SCIENCE AND TECHNOLOGY

Department of Geology

Structural and Stratigraphic Setting and Fluid Flow Features of the Svyatogor Ridge, a Sediment Drift South of the Molloy Transform

—

Ingvild Myrvang Westvig

EOM-3901 Master Thesis in Energy, Climate and Environment
July 2015

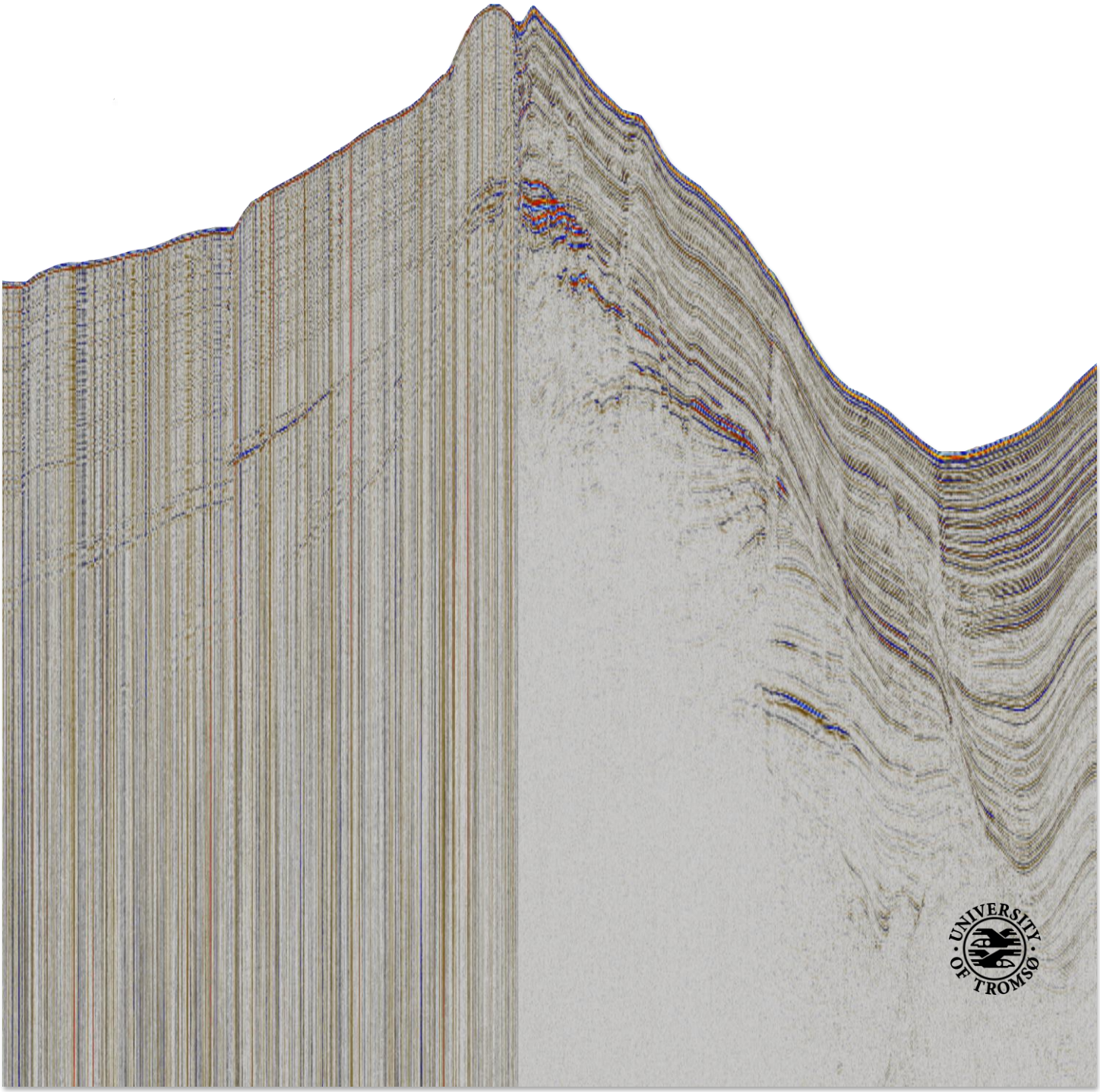

Abstract

High-resolution two-dimensional (2D) multichannel seismic data was acquired in 2014 from the Svyatogor Ridge, a sediment drift on the northwestern flank of the Knipovich spreading ridge. Seismic data is here processed, and together with multibeam bathymetry data and a correlation with Ocean Drilling Program (ODP) Hole 909, an interpretation of the structural and stratigraphic framework of the Svyatogor Ridge is established. The Svyatogor Ridge is highly influenced by tectonic processes from both the ultraslow spreading Knipovich Ridge and its northward intersection with the Molloy Transform Fault. From this interpretation a gas hydrate system has been identified by a prominent Bottom-Simulating Reflector (BSR) and pockmark features on the seafloor with evidence of fluid pathways underlain. The underlying young oceanic crust is possibly serpentinized, and hypothesized to provide the overlying sediments with abiotic gas though large basement faults, here interpreted as detachment faults, and a series of normal faults pervading most of the sedimentary stratigraphy on the west of the ridge apex.

Acknowledgements

I would like to thank Assoc. Prof. Stefan Bünz for his excellent supervision and advice regarding this thesis. I would also like to thank Andreia Plaza Faverola for her guidance and for all the time spent in the search for the right coordinates, it is greatly appreciated.

I would like to direct my appreciations to Sandra Hurter for the help with the SeisSpace PROMAX software, and to Sunil Vadakkepuliyambatta for providing help on locational illustrations.

I am also very grateful to Kate Alyse Waghorn for guidance on both the RadExPro software and SeisSpace PROMAX, and all for all the late night discussions that have provided me with greater insight that have been valuable for this thesis.

I greatly appreciate all the support and friendships that have been extended to me by the faculty, staff and students during my time at the University of Tromsø.

With great gratitude,

Ingvild Myrvang Westvig

Table of Contents

1 Introduction

1.1 Objective

The main aim of this project is processing and interpretation of newly acquired high-resolution, two-dimensional (2D) multichannel seismic data from the Svyatogor Ridge, south of the Molloy Transform Fault (MTF) offshore west Svalbard (Figure 1). The data was acquired with the P-Cable system configured for 2D surveys during a field campaign with R/V Helmer Hanssen in 2014, and integrated with multibeam bathymetric data. The objective of this integration is a joint interpretation of the data to delineate stratigraphic units based on a correlation of ODP borehole data, interpretation of structural features, mapping the distribution of the BSR as an indicator of gas hydrates, and identifying other fluid flow features in the area of study.

1.2 Motivation

The Svyatogor Ridge, comprising the study area of this thesis, is located in the eastern extent of the Greenland-Spitsbergen Plateau, at the northwestern edge of the Knipovich Ridge (Figure 1). The Molloy Transform Fault junctions the northern extent of Knipovich Ridge and the southern extent of the Vestnesa Ridge (Figure 1).

The Knipovich Ridge, a segment of the Mid Atlantic Ridge system, is characterized to be an active ultraslow spreading ridge. The Vestnesa Ridge and the Svyatogor Ridge have been found to have once been the same system, before breaking apart by the Molloy Transform about 2Ma ago due to the northward extension of the Knipovich spreading ridge. The Vestnesa Ridge hosts an active gas hydrate system, where the gas was hypothesized to have an abiotic origin (Johnson et al., 2015).

The main objective of this thesis is to gain a better understanding of how tectonic regimes of the Molloy Transform Fault and Knipovich Ridge have influenced structural and stratigraphic evolution, and fluid systems on Svyatogor Ridge and investigate if these systems show similar characteristics as systems found on the Vestnesa sediment drift.

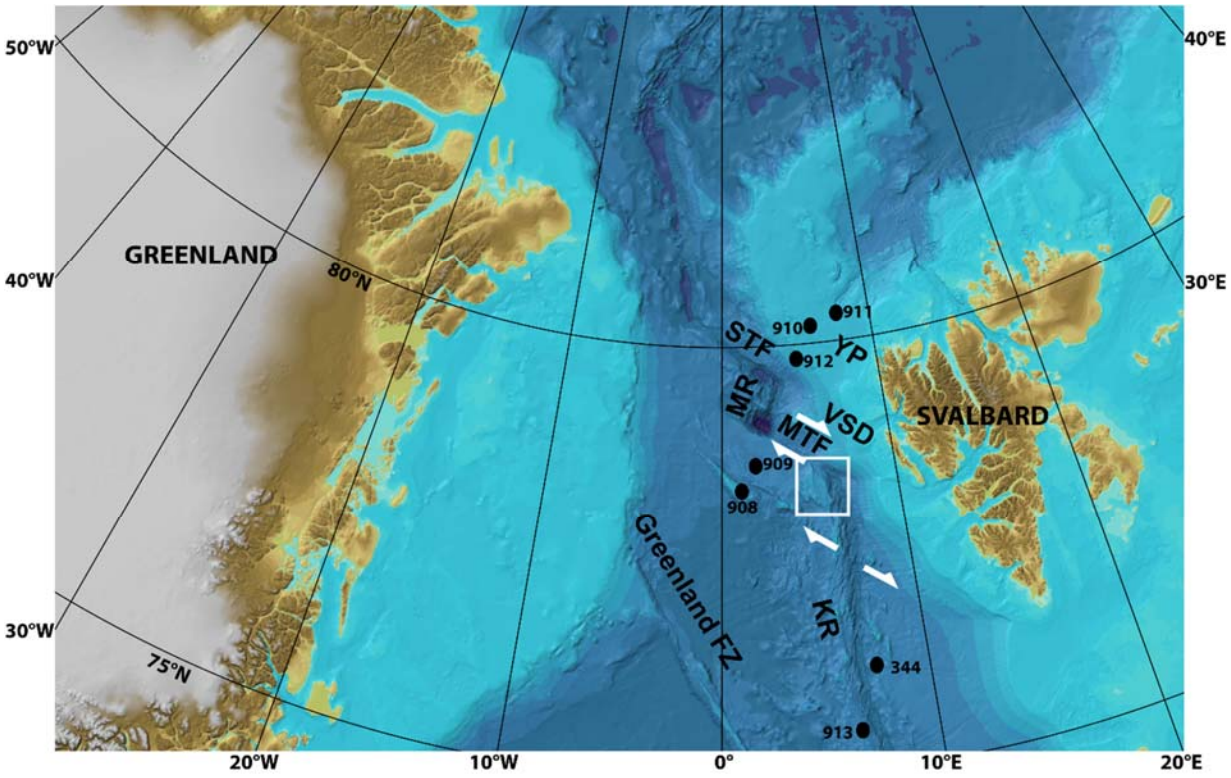

Figure 1. Regional location of the study area (white box) in the Fram Strait on the western Svalbard margin. Location of ODP boreholes: 912, 911, 910, 909, 908, 344 and 913. YP - Yermak Plateau; VSD - Vestnesa Sediment Drift; STF – Spitsbergen Transform Fault; MR – Molloy Ridge; MTF – Molloy Transform Fault; KR – Knipovich Ridge.

1.3 Basic Mechanisms of Fluid Flow

Subsurface fluid flow is the movement of water, mantle derived fluids and hydrocarbons in the subsurface. An understanding of fluid flow is of great interest due to their effects on the sub seafloor, geological features on the seafloor, marine biological processes, commercial abilities and the general composition of the oceans (A. Judd & Hovland, 2007).

Today's technology provides us with a better understanding of how fluids in the subsurface migrate and how they can form features with different characteristics on the seafloor. Fluidal migration through the subsurface towards the seafloor can happen both quietly and explosively, through both continuous and episodic events (A. Judd & Hovland, 2007; Løseth, Gading, & Wensaas, 2009).

Three physical laws can generally sum up the basic mechanisms of fluid flow. These laws are; Darcy`s law, Fick`s law and the mechanisms of advective flow.

1.3.1 Darcy`s Law

Darcy`s law, formulated by Henry Darcy, is possibly the most important law for studying fluid flow in porous and permeable sediments (C. Berndt, 2005). Vincent, Muthama, and Muoki (2014) defined Darcy`s law as follows;

> *"Darcy`s law is a simple proportional relationship between instantaneous discharge rate through a porous medium, the viscosity of the fluid and the pressure drop over a given distance"*

This is also described using its physical equation;

$$qv = -\frac{k \cdot A}{\eta} \nabla p$$

Where k is the rock permeability, η is the fluid viscosity coefficient, and ∇p is the pressure gradient in the direction of flow (Lien & Løvhøiden, 2010).

This means that for a fluid to flow through a specific rock, it is dependent of the rock properties; the rock needs to have the ability to conduct fluids (K). This property relates to porosity and permeability i.e. the amount of space between grains so that fluids are able to pass through. The pressure difference and hydraulic gradient between pore water in- and out-flow is important when considering fluid migration, as fluids will flow from high- to low hydraulic potential (C. Berndt, 2005; Bjørlykke, 1993).

1.3.2 Fick`s Law of Diffusion

Diffusion represents the amount of particles moving due to thermal motion. Thermal motion results in a redistribution of molecules in both fluids and solids, although the rate of movement in solids is much less than that of fluids (Krooss & Leythaeuser, 1996). Considering diffusive flow in porous media, such as sedimentary rock, the law of diffusion is often formulated as follows (Krooss & Leythaeuser, 1996):

$$J = -D_{eff} grad\ C_{bulk}$$

Where D_{eff} is the effective diffusion coefficient and C_{bulk} is the bulk volume concentration.

Fick`s law of diffusion works in a similar way to Darcy`s law. Instead of fluid movement induced by pore-pressure differences, here movement is induced by a diffusive flux (C. Berndt, 2005). This means that pore-fluid constituents containing differences in concentrations will have a net movement of individual particles from an area of high concentration to an area of low concentration.

1.3.3 Advective Flow

Advective flow refers to the movement of fluids through fractured rocks or rocks of high permeability, induced by pressure and density gradients (bulk flow) (Moore & Wilson, 2005). The flow rate of advective flow is higher than that of Darcy flow. The bulk flow can be caused by local conditions such as hydrothermal vents at the margins between continent and ocean, or from land by e.g. coastal submarine springs (Moore & Wilson, 2005).

1.4 Origin of Hydrocarbons

"A hydrocarbon is an organic compound consisting of carbon and hydrogen only" (Speight, 2010). Origins of hydrocarbons in the marine environment fall into three categories: biogenic (microbial methane), thermogenic and abiogenic (A. Judd & Hovland, 2007). The following two sections investigates these categories.

1.4.1 Biogenic and Thermogenic Origin

The formational process of hydrocarbons with an organic matter based origin are divided into two main groups. For organic material to become what we call hydrocarbons, it needs to be degraded either by (1) microbial decay in the shallow subsurface, through methanogenesis, or by (2) thermogenic degradation (A. Judd & Hovland, 2007).

Photosynthetic production of organic material from CO_2 occurs predominantly in the upper tens of meters in the water column. This formation of organic material can be summed by this chemical equation (A. Judd & Hovland, 2007):

$$6CO_2 + 6H_2O \rightarrow C_6H_{12}O_6 + 6O_2$$

Here $C_6H_{12}O_6$ are carbohydrates represented by sugars, a biopolymer. A small portion of the marine organisms fall to the seafloor where they become part of the sediments. At this stage, microbial processes decompose the biopolymers. With decomposition and depth (decrease of oxygen), methanogens[1] will to a point become dominant (A. Judd & Hovland, 2007).

1.4.1.1 Methanogenesis

The occurrence of methanogenesis requires specific conditions, e.g., anoxic environment, low temperatures, low sulphate concentration etc. (A. Judd & Hovland, 2007). Methanogenesis can occur in three pathways. The most dominant of the three pathways is the reduction of carbon dioxide. This pathway produces methane through the reduction of CO_2 by hydrogen gas stated by the following equation (A. Judd & Hovland, 2007):

$$CO_2 + 4H_2 \rightarrow CH_4 + 2H_2O$$

1.4.1.2 Thermogenic degradation

Microbial methanogenesis will with burial, and hence increasing temperatures, at some point stop and thermogenic degradation takes place. At this point some of the organic material can still be intact, often the organic compounds that are less soluble. This material will form condensed polymers, and later, kerogen. Through thermal cracking of kerogen, hydrocarbons are produced (A. Judd & Hovland, 2007).

1.4.2 Abiogenic Origin

Abiogenic gas, in contrast to other formation mechanisms, is not formed by degradation of organic matter, but rather through chemical reactions in ultramafic rocks (Cannat, Fontaine, & Escartín, 2013). Abiogenic methane can form in the subsurface in several ways. According to Etiope and Sherwood Lollar (2013), at least nine specific mechanisms of the production of abiotic CH_4 appears in scientific literature (including theoretical and experimental). These mechanisms are categorized into magmatic processes and gas-water-rock reactions. The mechanism that might be the most widely recognized and occur naturally is the Fischer-Tropsch Type Reactions (FTT), especially in

[1] Methanogens – Methane-producing microorganisms

regards to serpentinization (Etiope & Sherwood Lollar, 2013). FTT reactions fall under the category of gas-water-rock reactions which are "*inorganic syntheses independent of the presence of magma or magma-derived fluids"* (Etiope & Sherwood Lollar, 2013).

The synthesis of Fischer-Tropsch is an industrial process where CO_2 reacts with H_2 and results in the formation of hydrocarbon (M. E. Berndt, Allen, & Seyfried, 1996), and can both be dependent and independent of serpentinization (Etiope & Sherwood Lollar, 2013).

Ultramafic rock is a result of crystallization of mantle-derived magma, or by partial crystallization from magma ocean as cumulates (Müntener, 2010). Ultramafic rock is often exposed in areas of slow and ultraslow spreading ridges, mountain belts with tectonically active zones, and alongside passive margins that are magma-poor. The main components of ultramafic rocks is olivine and pyroxenes (Müntener, 2010).

Serpentinization is a metamorphic process where hydration and oxidation of ultramaphic rocks (olivine and/or pyroxene) produces serpentinites (which is composed of at least one serpentine group mineral) (Etiope & Sherwood Lollar, 2013; Sleep, Meibom, Fridriksson, Coleman, & Bird, 2004). In the presence of carbon dioxide, serpentinite has the ability to form methane through this chemical reaction:

$$CO_2 + 4H_2 = CH_4 + 2H_2O$$

This reaction shows how mixing of water derived serpentinite and water rich in CO_2 results in the formation of methane (CH_4) (M. E. Berndt et al., 1996; Sleep et al., 2004).

1.4.3 Identification of Origin

The identification of origin (organic or inorganic) of hydrocarbons can be achieved by measuring the value of $\delta^{13}C$ (typically in CH_4). Hydrocarbons with a high content of $\delta^{13}C$ (about –27‰) are characterized to be of inorganic origin, while a low content of $\delta^{13}C$ (< –30‰) characterizes organic origin (Zou, 2012). Figure 2 illustrates how these isotopic characteristics can be of aid for a determination of origin between biotic and abiotic gas. This schematic differentiation can be of aid for a determination, but cannot reveal if the gas is solely abiotic or biotic, or a mixture of the two (Etiope & Schoell, 2014).

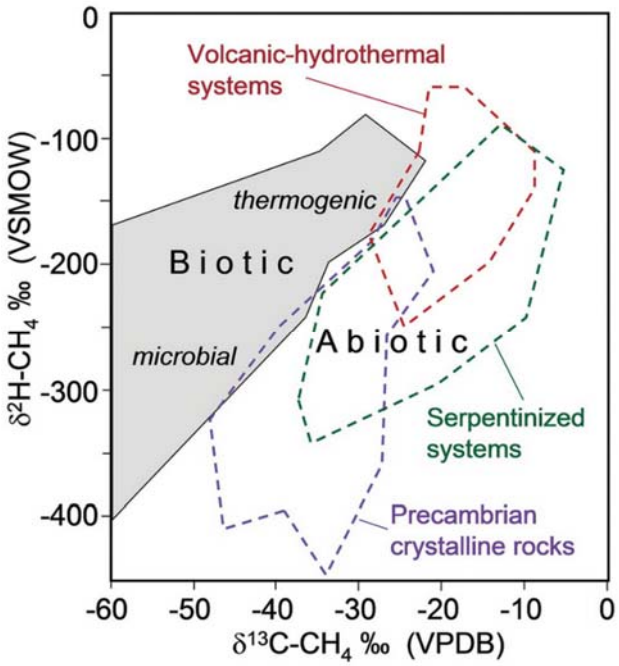

Figure 2. Diagram of $\delta^{13}C$ versus $\delta^{2}H$ for methane, known as a "Schoell Plot". The plot illustrates four general isotopic fields: biotic methanes (thermogenic and microbial), and three abiotic methanes (volcanic and geothermal systems, Precambrian crystalline rocks, and serpentinized ultramafic rocks) (Etiope & Schoell, 2014)

1.5 Fluid Flow Features

1.5.1 Pockmarks

Pockmarks were first discovered by King and MacLean (1970) on the Scotian Shelf after the introduction of the side-scan sonar, which enabled them to survey the seafloor in a new manner. Pockmarks are craters on the seabed formed by seepage of gas and liquids through the seafloor, and generally serve as an indication of focused fluid flow (M. Hovland et al., 2002; Martin Hovland & Judd, 1988). This description of pockmarks provided by M. Hovland et al. (2002) does not discriminate between the type of fluid that forms the pockmark, and establishes that they can form under a wide variety of circumstances, with morphological diversity. The occurrence of pockmarks on the seabed is generally restricted to environments of fine-grained, low permeability sediments (Martin Hovland & Judd, 1988). Depressions on the seabed are not by definition pockmarks, although the definition of pockmarks is broad. Pockmarks are features that are erosive by nature, which is the agent that distinguishes them from other features on the seafloor. Upward migration of fluids and bottom currents functions as erosive agents (A. Judd & Hovland, 2007).

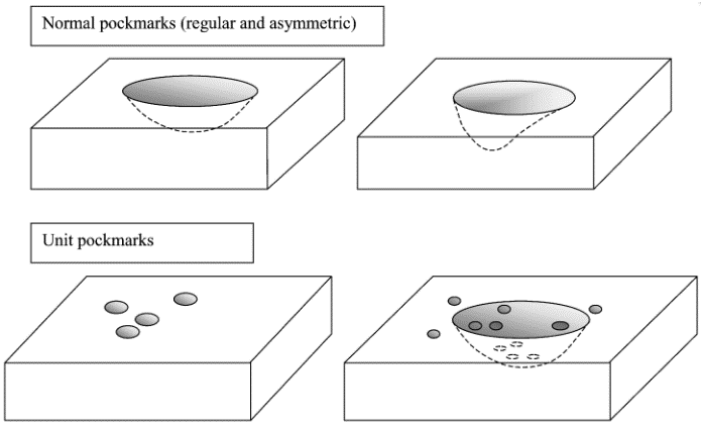

Figure 4. Illustration of the shape of normal pockmarks (both regular and asymmetric), and the shape of unit pockmarks, occurrence in groups and in association with normal pockmark (M. Hovland et al., 2002)

Although the diversity of morphology of pockmarks is great, there are some shapes and sizes that are more common than others, and which can be summed into six classes of morphology (M. Hovland et al., 2002). *Unit pockmarks* (Figure 4) are often a result of a single expulsion of fluids, and occur as small depressions. They are considered the smallest of the six classes (generally 1-10 m in diameter, and < 0.5 m deep). These pockmarks can be found as isolated depressions, in groups, or adjacent to normal pockmarks (M. Hovland et al., 2002; A. Judd & Hovland, 2007). *Normal pockmarks* (Figure 4) occur as circular craters, with a size that generally varies from 10-700 m in diameter and depth between 1 m and 45 m. These pockmarks vary in form of their cross-section. Some occur as asymmetrical with steep walls, while others have low-angled walls (M. Hovland et al., 2002). *Elongated pockmarks* (Figure 3) are found to occur in areas with fault structures, strong bottom currents, and on slopes, and have a more elongated shape than normal pockmarks. This elongated shape is seen by one axis being longer. This type of pockmark can also occur as *composite pockmarks*, which are depressions that have merged, forming a depression of more complex shape (M. Hovland et al., 2002; A. Judd & Hovland, 2007). *Eyed pockmarks* (Figure 3) are identifiable with a characteristic high-reflective region in the centre of depression. This reflection can be caused by coarse material, biological activity, or

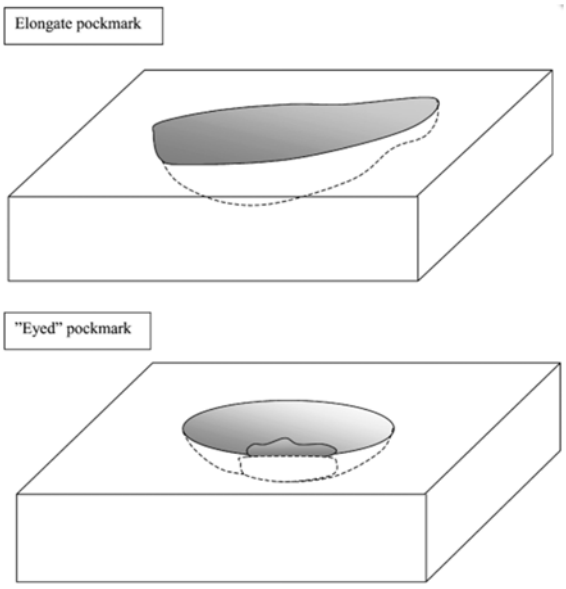

Figure 3. Illustration of elongated pockmark and eyed pockmark (M. Hovland, Gardner, & Judd, 2002)

precipitation of authigenic carbonate (M. Hovland et al., 2002). *Strings of pockmarks* are also relatively common on the seabed, and are composed of several unit pockmarks or small pockmarks that are organized in curvilinear chains, up to several kilometres long (M. Hovland et al., 2002).

1.5.2 Seismic Indications of Gas

Seismic (geophysical) data is a valuable tool that can remotely investigate the sub-seafloor and provide direct evidence of shallow gas. The presence of gas in the sub-surface can take many forms on seismic data, and seismic reflection indicators may be found as single features, in association with each other, and/or in association with features on the seafloor (A. G. Judd & Hovland, 1992). These indications are results of an acoustic impedance contrast between the properties of different materials. Acoustic impedance is a product of density and compressional wave velocity, (V_P) (P-wave velocity) (Andreassen et al., 2007).

1.5.2.1 Enhanced Reflections

Enhanced reflections are reflections that for parts of their lateral extent show increased amplitudes that often indicate gas accumulations. This type of reflection often occurs in relations with acoustic turbidity, where increased amplitudes extends from the zone of turbidity (Martin Hovland & Judd, 1988; A. G. Judd & Hovland, 1992). A common form of enhanced reflections are *bright spots* (Figure 5 andFigure 6). These are strong negative phase reflections, which indicate the upper boundary of gas charged sediments, i.e., free gas. Because of this negative reflection coefficient, the reflection will be phase reversed relative compared to the seafloor, where the impedance contrast is positive. This strong negative reflection is often followed by a strong positive reflection, a *flat spot* (Figure 5), from an underlying gas-water contact, if the gas filled section is thick enough (Andreassen et al., 2007; A. G. Judd & Hovland, 1992; Ligtenberg, 2005). It is noteworthy that a concentration of 4 % gas within the pore spaces results in the largest drop in P-wave velocity. Seismic data is therefore a valuable tool for indications of small concentrations of gas, but does not distinguish much in variations of concentrations (Andreassen et al., 2007).

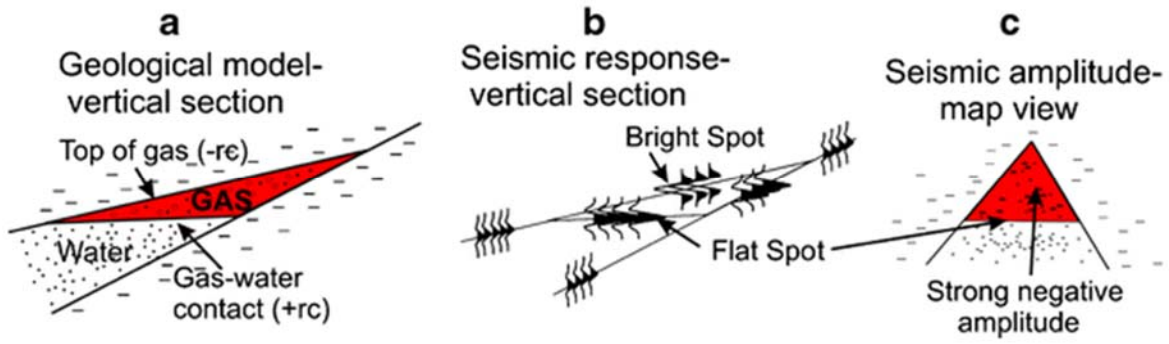

Figure 5. Illustration of seismic indications of gas. a) Sketch of a vertical section with a gas-bearing fan overlying water-filled sediments. b) Vertical section illustrating the seismic response of the gas wedge in a). Horizontal illustration (map-view) of the gas-wedge in a), where strong negative amplitudes are shown in red (Andreassen, Nilssen, & Ødegaard, 2007).

1.5.2.2 Acoustic Turbidity/Acoustic Masking

Acoustic turbidity on seismic sections is a result of scattering of energy, and appears as chaotic reflections. These chaotic reflections will eliminate other underlying reflections (Figure 6). Clay rich, impermeable sediments with finely spread gas will appear as acoustic turbidity in seismic data (A. G. Judd & Hovland, 1992). Reflections in proximity and extending towards sections of acoustic turbidity often experience a *pull down* effect where the reflections are deflected downwards (Figure 6). This is due to the decrease of acoustic velocity (V_P) in the gas-bearing zone (A. G. Judd & Hovland, 1992).

1.5.2.3 Columnar Disturbances

Vertical features of disturbed or destroyed reflections are often referred to as *seismic chimneys* or *acoustic pipes* (Figure 6), and are results of the upward migration of fluids, usually gas (Andreassen et al., 2007; Martin Hovland & Judd, 1988). Both seismic chimneys and acoustic pipes are acoustic masking, but they differ in their appearance in seismic sections. Seismic chimneys are vertical zones, while acoustic pipes are sub-vertical, circular, and narrower zones of acoustic masking. Acoustic pipes can be discontinuous as they are often disrupted along their vertical extent (Andreassen et al., 2007).

1.5.2.4 Acoustic Blanking

Acoustic blanking appears as small areas where reflections are weak or absent. These patches can be due to migration of pore fluids that disrupts the sedimentary stratification, but also from gas-charged sediments above that can absorb much of the penetrating energy (A. G. Judd & Hovland, 1992). In the case of pore fluids, a *pull-up* structure can occur in the upper section of the acoustic blanking. This pull-up structure occurs in association with gas hydrates or authigenic carbonate concretions (Lee, Baek, Ryu, Riedel, & Hyndman, 2005; Riedel, Spence, Chapman, & Hyndman, 2002). Another resulting factor can be overlying harder sediments. Energy through hard sediments will experience an energy loss and the returning energy has lower amplitudes (A. G. Judd & Hovland, 1992).

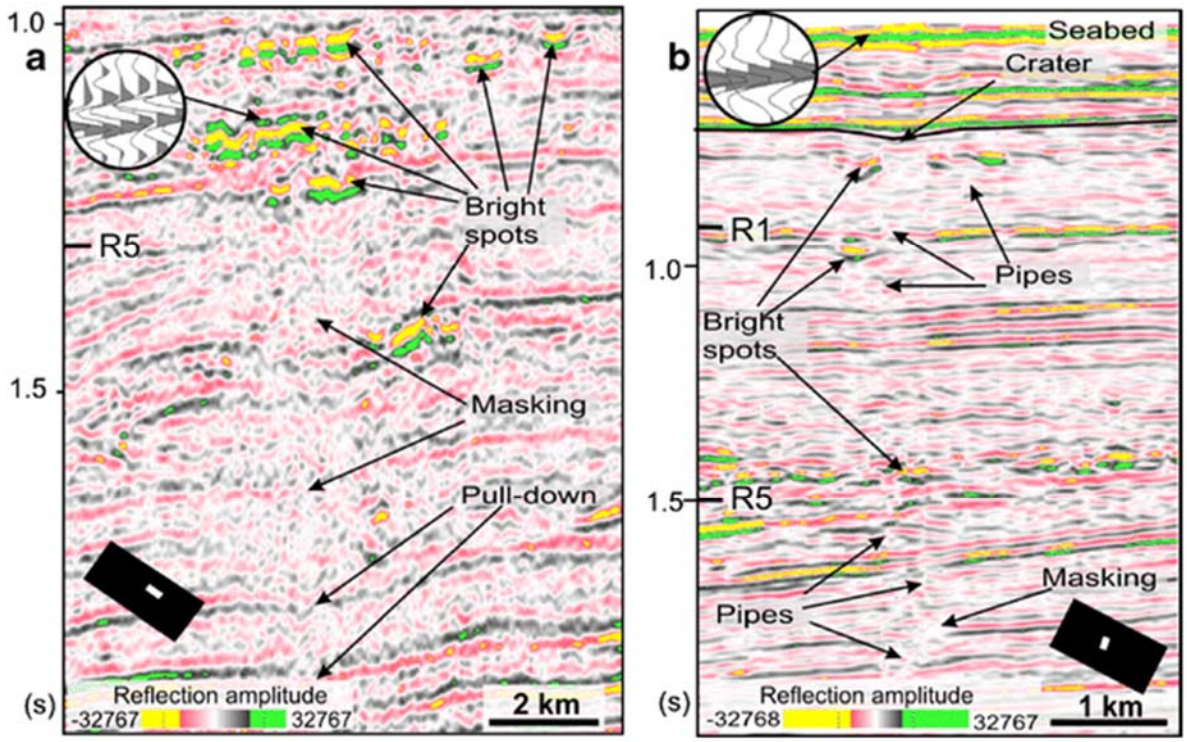

Figure 6. a) Seismic section imaging bright spots, acoustic masking, and the pull down effect. b) Seismic section imaging acoustic pipes representing migration of gas-bearing fluids, with associated bright spots and acoustic masking. The wiggle-trace in the upper left corner of a) shows the wiggle trace for bright spot, and in b), the seafloor reflection (Andreassen et al., 2007)

1.6 Fault Related Fluid Migration

Faults serve as an important conduit for fluid migration in the subsurface (Ligtenberg, 2005). On seismic data, fault zones are in general too narrow to be imaged. Indications of faults are therefore identified as discontinuities in reflections that can be traced through a seismic profile (Løseth et al., 2009). Faults can be categorized as being non-conductive (fully sealed) or conductive (fully open), although studies have shown that fluids tend to migrate through weak sections of faults (Ligtenberg, 2005). Bright spots or larger zones of enhanced amplitudes along faults can be an indicator of a leaking fault (Ligtenberg, 2005; Løseth et al., 2009). Distribution of fluids through fault can often occur irregular, and fluids will often migrate through faults into intersecting permeable layers (Løseth et al., 2009).

Build-up of stress in sedimentary rock can often cause faulting, folding and fracturing. A build-up of stress is often a result of local or regional tectonic processes. Faults, and often its interconnected fracture zones, can greatly increase permeability and cause high flow rates (Løseth et al., 2009).

1.7 Gas Hydrate System

1.7.1 Gas Hydrates

Gas hydrates are ice-like structures composed of water and gas, primarily methane. A recent global estimate of the amount of methane sequestered in gas hydrates was done by Dickens (2011) and valued to be between 170-12,700Gt. The gas molecules (guests) are surrounded by hydrogen-bonded water molecules (host) and form a framework called a clathrate (Martin Hovland, 2005). Figure 7 illustrates this framework.

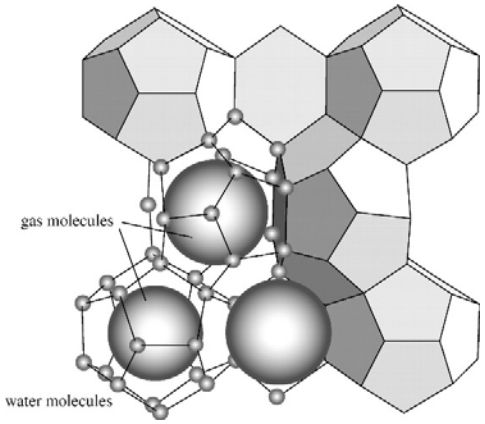

Figure 7. Typical structure of gas hydrate, showing gas molecules surrounded by hydrogen-bonded water molecules (Maslin et al., 2010)

The formation, hence stability, of gas hydrates are constrained to specific conditions e.g. high pressure and relatively low temperatures (usually <10˚C), with a sufficient amount of both gas and water. Other factors also affect the formation, such as seawater salinity, texture and type of sediment. These conditions are common in regions of permafrost and continental margins

at depths greater than 300-500m (Martin Hovland, 2005; Maslin et al., 2010; Nealon, 2006). Gas hydrates are often sensitive to changes in pressure-temperature regimes. A reduction of pressure or an increase in temperature can cause instability in the structure that can result in a phase change from solid to liquid gas. Causes of pressure and/or temperature changes include; sea-level changes, shrinking of ice-sheets, increase in bottom water temperature, or advection or diffusion (see section 1.3) of the methane towards the seafloor. The GHSZ[2] is determined by pressure and temperature and indicates the area in which the gas hydrates are stable. Beneath this zone there is often free gas, indicated by the BSR[3] (Martin Hovland, 2005; Maslin et al., 2010; Nealon, 2006). Figure 8 illustrates the GHSZ for polar regions. This figure shows that the stability of gas hydrates extends into the water column; however, gas hydrates will not form in seawater (without direct connection to the seafloor). This is due to circulation and the high solubility of methane in seawater (Martin Hovland, 2005). Previously, scientists assumed that within the GHSZ all gas molecules are trapped within hydrate structures. Today's consensus is that there is a constant migration of free gas through this zone, both through sediments and hydrates, which are porous in nature (Liu & Flemings, 2007).

1.7.2 Bottom-Simulating Reflector (BSR)

A bottom-simulating reflector (BSR) refers to a specific type of seismic reflection at shallow depths which mimics the seafloor (C. Berndt, Bünz, Clayton, Mienert, & Saunders, 2004). The most common geological processes that results in a BSR are 1) diagenesis of siliceous sediments in the opal A to opal CT and quartz conversion zones, called diagenesis-related BSR and 2) the difference in velocity characteristics between the free gas zone and the GHSZ, called gas hydrate-related BSR (C. Berndt et al., 2004; Nealon, 2006).

1.7.2.1 Diagenesis-Related BSR

Diagenesis refers to all the processes that result in changes in sediments or sedimentary rocks after deposition. The nature of these processes can be physical, chemical and/or biological (Berner, 1980; Milliken, 2003).

[2] GHSZ – Gas Hydrate Stability Zone
[3] BSR – Bottom-Simulating Reflector

Introduction

The processes and nature behind diagenesis-related BSRs are less studied than BSRs related to gas hydrates. One reason for this is the commercial possibilities of gas hydrates and their effects on global climate (MacKay, Jarrard, Westbrook, & Hyndman, 1994). Diagenesis-related BSR is a result of the diagenesis of siliceous sediments in its different stages (opal-A, opal-CT and quartz) (C. Berndt et al., 2004). Kastner, Keene, and Gieskes (1977) introduced the following diagenetic sequence:

Opal-A (siliceous ooze) → Opal-CT (porcelanite) → chalcedony or cryptocrystalline quartz (chert) → mega-quartz (chert)

In the initial phase, the silica is biogenic in most deep-sea siliceous sediments. This phase is a hydrated amorphous form of silica, known as opal A. During diagenesis the deposit will undergo mineralogical changes to form opal-CT, and later with further burial (higher temperatures) opal-CT transforms to microcrystalline quartz, a stable phase of silica (Kastner et al., 1977).

The BSR related to this diagenesis is a result of the positive acoustic impedance contrast between the different stages of the siliceous sediments. This BSR has the same polarity as the seafloor reflection (C. Berndt et al., 2004).

1.7.2.2 Gas Hydrate-Related BSR

BSR is the most commonly used identifier for gas hydrates. It occurs at shallow depths, just a few hundred meters below the seafloor, parallel to the seafloor (Andreassen, 2009; Haacke et al., 2007; Nealon, 2006).

The BSR related to gas hydrates has strong negative impedance contrasts with reversed polarity relative to the seafloor (Figure 9). The reversed polarity is a product of the contrast between the high velocity hydrate-bearing layer and the low velocity free gas zone below (Figure 9). The BSR follows the surface topography and lies at a constant depth below it (A. Judd & Hovland, 2007; MacKay et al., 1994). In areas where subsurface sedimentary stratigraphy deviates from that of the seafloor the BSR will crosscut the stratigraphy. Reflections underlying the BSR often shows a trend of having high amplitudes, and thus being well defined (C. Berndt et al., 2004; A. Judd & Hovland, 2007; MacKay et al., 1994). Overlying reflections are often less defined and have low amplitudes,

being “seismically transparent”. This can be due to cementation of gas hydrates (A. Judd & Hovland, 2007). The pore spaces in the free gas zone, below the GHSZ, is partially filled with free gas. The BSR can form from as little as 1-2% free gas in pore spaces, and underlie sediments that contain minor amounts of gas hydrates. The BSR can be a result of the high-velocity gas hydrates above the BSR, or by the low-velocity free gas below the BSR (Andreassen, 2009; C. Berndt et al., 2004; A. Judd & Hovland, 2007; MacKay et al., 1994; Nealon, 2006). Although the BSR is a good indication of the presence of gas hydrates, hydrates may also occur without the BSR indicator if there is no accumulation of free gas at the BGHSZ (Holbrook et al., 2002).

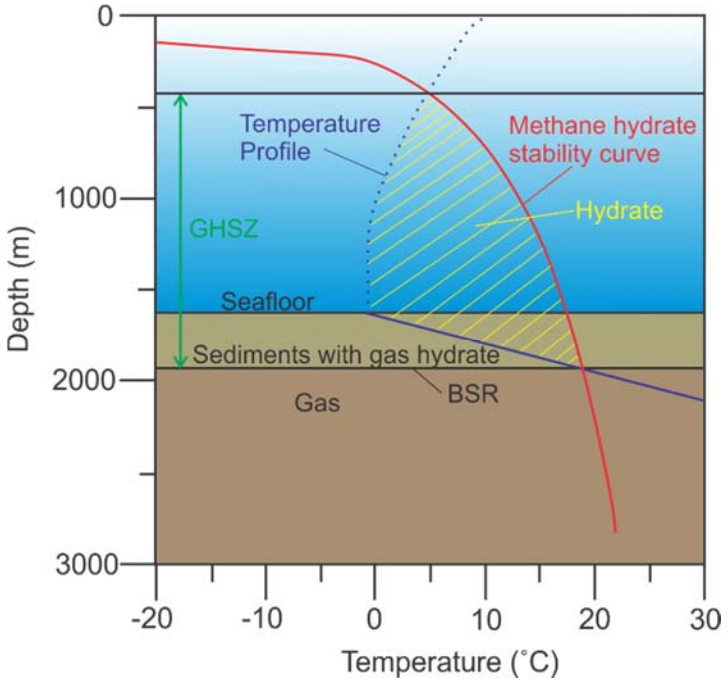

Figure 8. GHSZ for Polar Regions in a depth-temperature diagram, modified from (Chand & Minshull, 2003). This figure is based on an example from offshore Norway with a geothermal gradient of 50˚C km^{-1}

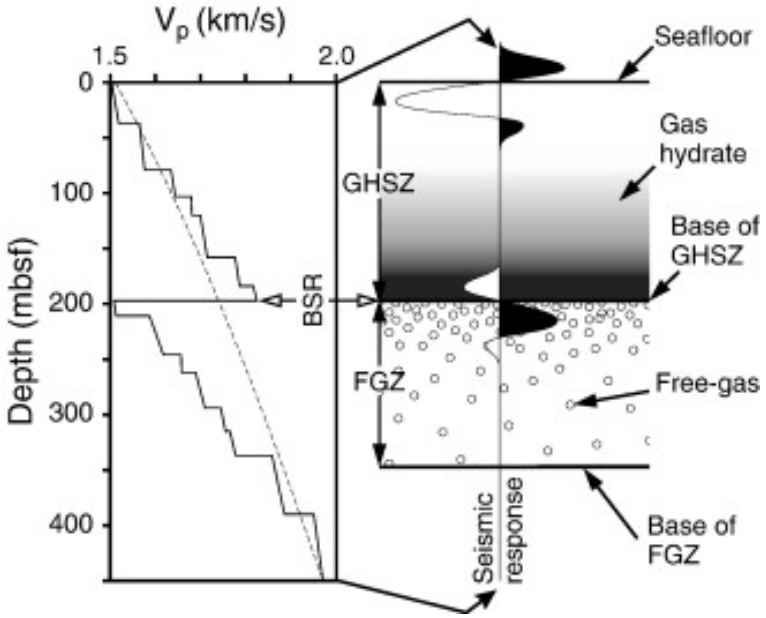

Figure 9. Illustration of a seismic trace through a sedimentary section containing a zone of free gas (FGZ) below the BSR and gas hydrates above. The P-wave velocity (V_p) indicates a decrease of free gas with depth. The reflection of the BSR marks the base of the GHSZ. This reflection shows the reverse polarity of the BSR (Haacke, Westbrook, & Hyndman, 2007)

2 Geological Framework

The data discussed and interpreted in this thesis was acquired on the Svyatogor Ridge (Figure 1). This ridge is a sediment drift that is located in the northern Knipovich Ridge, an oceanic ridge system in the Atlantic Ocean, south of the Molloy Transform Fault (MTF).

2.1 Tectonic Background

The Knipovich Ridge is a segment of the Mid Atlantic Ridge system, and is bounded by the Mohns Ridge to the south and the Molloy Ridge in the north, the two being separated by the Molloy Transform Fault (Kandilarov, Mjelde, Okino, & Murai, 2008; Yampol'skiy & Sokolov, 2012). The ocean-basin of the Norwegian-Greenland Sea is very young in a geological timescale. This has enabled scientists to study the early development of mid-ocean ridges, as stages of rifting and spreading (Crane et al., 2001).

2.1.1 Knipovich Ridge

The Knipovich Ridge has a length of ~500 km, extending from the Mohns Ridge at ~73˚50´ to ~78˚30´ where it junctions with the Molloy fracture zone (Kandilarov et al., 2008). This junction with the Molloy Transform lies in direct vicinity of Spitsbergen, the western border of the Eurasian plate (Peive & Chamov, 2008), and comes as close as 80 km to the coastline of Svalbard (Thiede, Pfirman, Schenke, & Reil, 1990). The rift valley of the ridge is V-shaped and the western and eastern flanks shows varying angles alongside the strike. The walls of the ridge, as well as the valley, are divided by an abundancy of oblique faults, and the walls are further complicated by terrace-shaped scarps (Peive & Chamov, 2008). Figure 10 illustrates the tectonic complexity of the faults in the area.

The development of the ocean-ridges in the Norwegian-Greenland Sea have a complex history, as indicated by the complexity of the plate boundaries and migration of spreading axes (Crane et al., 2001; Eldholm, Sundvor, & Wissmann, 1980). The Paleo-Spitsbergen Fault has undergone regimes of both extension and compression (Peive & Chamov, 2008). Spreading of the Knipovich Ridge is thought to have originated from the northward extension of the Mid Atlantic Ridge, when the spreading propagated into the Spitsbergen Shear Zone (Crane et al., 2001; Talwani & Eldholm,

1977). According to studies done on dating fauna, Talwani and Eldholm (1977) found that the propagation of the Mid Atlantic Ridge into the Fram Strait started in the Early Oligocene (33 Ma). The ridge later had an eastward migration, and migration to its present location was about 5-6 Ma ago (Eldholm et al., 1980). This propagation into the Fram Strait resulted in an asymmetrical, ultra-slow spreading that is oblique to the plate boundary in the Knipovich Ridge (Crane et al., 2001; Crane, Sundvor, Buck, & Martinez, 1991; Kandilarov et al., 2008; Talwani & Eldholm, 1977).

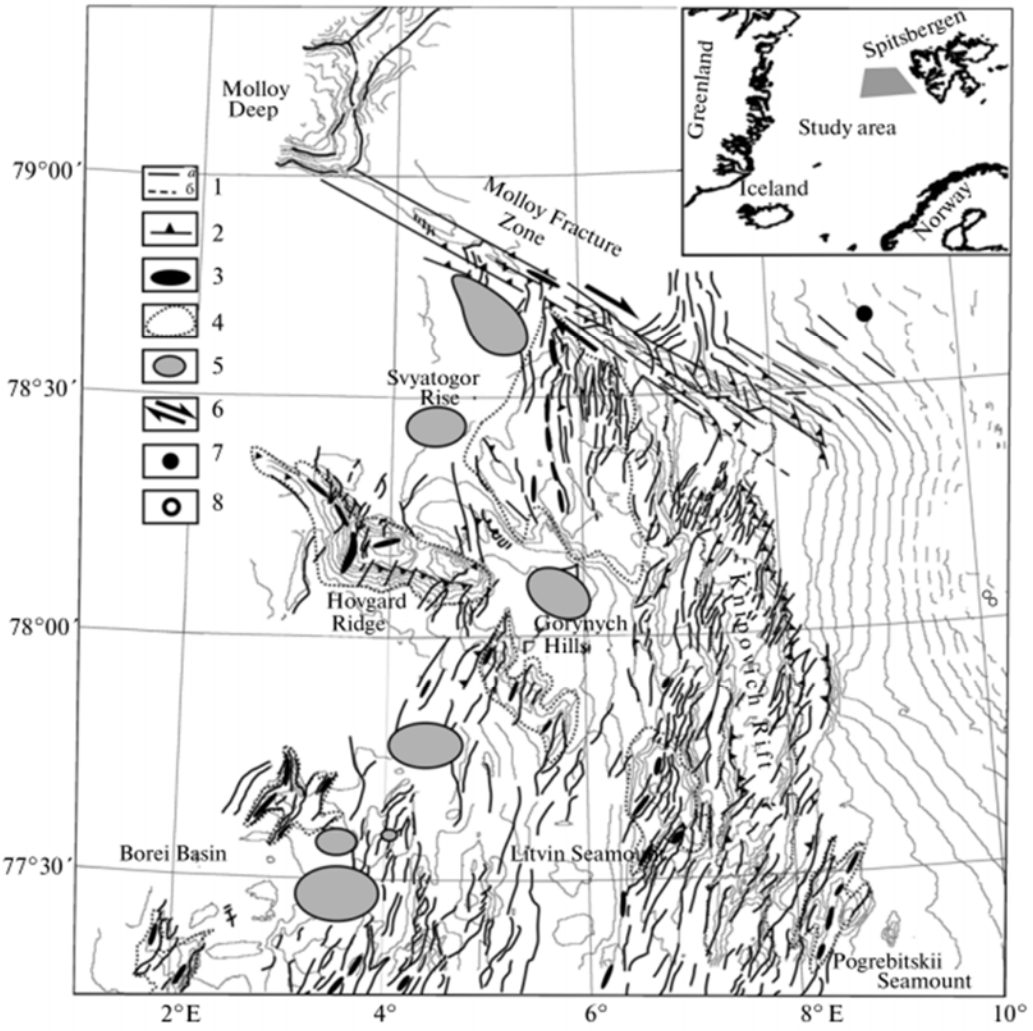

Figure 10. Illustration of the tectonic setting in the northern area of the Knipovich Ridge, and the Molloy Fracture Zone. (1) Faults (generally strike-slip); a) observed, b) assumed. (2) Down dip-strike-slip faults and normal faults. (3) Strike of positive structures. (4) Contours of morphological structures. (5) Areas of dominant deformations. (6) Direction of movement along strike-slip faults. (7, 8) Interruption in the sedimentary cover, assumed to be related to fluid discharge. (7) The central-type structure. (8) Areas of subsidence. (Chamov et al., 2010)

Due to magnetic anomalies in the Knipovich Ridge area, estimation of spreading using magnetic data have proved to be difficult, so thermal modelling is used instead, although thermal modelling is proven to be less accurate than magnetic modelling (Crane et al., 1991; Ljones et al., 2004). Crane et al. (1991) suggests an asymmetrical spreading rate of 7 mm/year for the western flank of the Ridge, and 1 mm/year for the eastern flank. In the studies made by Kandilarov et al. (2008), this variation in spreading is indicated to be a result of a more rapid movement of the North American plate relative to the more stationary Eurasian plate. The depths of the flanks about the spreading centre throughout the Knipovich Ridge shows an antisymmetric trend, where the western flank is 300 m shallower on average than the eastern flank (Crane et al., 2001). At the junction with the Molloy Transform Fault, the rift valley increases in depth, which corresponds to a widening of the valley (Crane et al., 2001).

The western flanks of the Knipovich Ridge have complicated structures with folding and unconformities that is a result of tectonic deformation (Zayonchek et al., 2011). In general, the orientation of second-order structures on this ridge is a product of the rotation and closure of the Knipovich Rift Valley at its intersection with the Molloy Fracture Zone (Chamov et al., 2010). The Svyatogor Ridge is located on the western flank in the northern Knipovich Ridge (Figure 10), and the crest extends in a near meridional direction (Chamov et al., 2010). The ridge has an asymmetrical structure where its eastern flank shows a relief with stepped faults and the western flank have a gradual slope towards the Greenland-Norwegian Plateau (Chamov et al., 2010).

2.1.2 The Molloy Transform Fault

The Molloy Transform Fault is the northern termination of the Knipovich Ridge (Crane et al., 2001) (Figure 10), and extends in a north-west direction with an average width of 700m, and depths at average ranging from 2600-2650m, but with deeper sections in the middle of the fault (Zayonchek et al., 2011). In the studies done by Zayonchek et al. (2011) they found several faults and flexures in the top sections of the sedimentary cover. Side scan sonar studies show a 130 km double transform fault, trending 305°, in addition to 12 anastomosing faults with a complex structure (Crane et al., 2001). These faults were found to have a variation in length between 3.6-66 km. The faults on the western flank in the northern part of the Knipovich ridge curve into the Molloy

transform, and their orientations are shifted as much as 50° (Crane et al., 2001). This trend is also found in the eastern flank as well as the rift valley, with a curving towards the north-west. Along the transform fault, the faults on both sides are close to parallel to their strike. Rectilinear faults to the north of the Molloy Fracture Zone, with strikes paralleling both the Knipovich Ridge and the Molloy Transform Fault, cut of the Vestnesa Ridge. An assumption is that the propagation of the rift north of the transform can result in a deactivation of the Molloy Ridge and the Molloy Transform Fault (Crane et al., 2001).

2.2 Geological Setting

2.2.1 Sedimentary Stratigraphy

The western flank of the Knipovich Ridge shows a much greater topographic relief than that of the eastern flank, which is almost completely covered in sediments. This is due to the lack of sedimentary deposition in this area from the continental margin of east Greenland (Rajan, Mienert, Bünz, & Chand, 2012; Talwani & Eldholm, 1977). Amundsen, Blinova, Hjelstuen, Mjelde, and Haflidason (2011) suggest that sediments on the western flank is originated partly from the western Svalbard - north-western Barents Sea margin, where they have been deposited in the rift valley before being transported west through tectonic activity and spreading.

Three stratigraphic units has been defined on the southern Yermak Plateau: YP[4]-3. YP-2 and YP-1 (Eiken & Hinz, 1993; Geissler & Jokat, 2004). A chronostratigraphic framework for the Yermak Plateau, gathered from ODP Leg 151 (Sites: 911, 910 and 912), correlates with the chronostatigraphy found on ODP Sites 908 and 909 (Knies et al., 2009; Mattingsdal et al., 2014). Locations of ODP sites is shown in Figure 1. The Vestnesa sediment drift lies in the southern extent of the Yermak Plateau. A tectonic reconstruction by Johnson et al. (2015) shows that the Svyatogor Ridge is an extent of the Vestnesa ridge, with an offset of 30 km. This reconstruction is illustrated in Figure 11. The reconstruction shows that sedimentary deposition of the Svyatogor Ridge started just prior to the breakup from Vestnesa Ridge at 2Ma.

[4] YP – Yermak Plateau

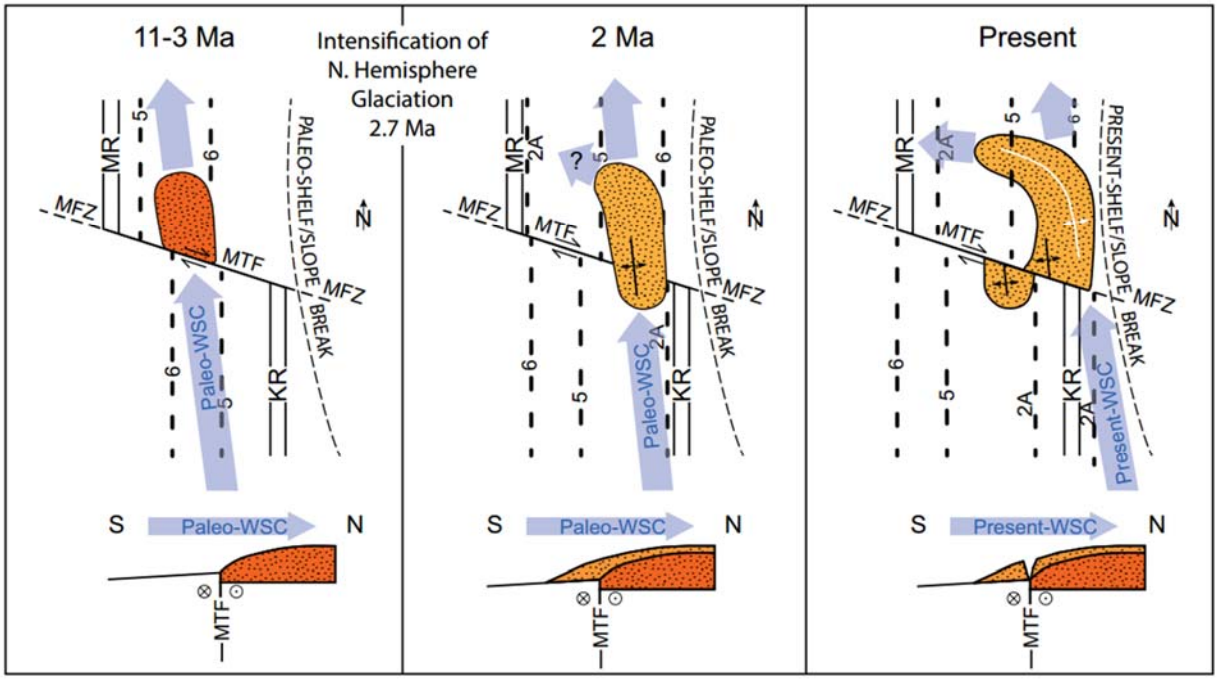

Figure 11. Tectonic reconstruction of the separation between the Vestnesa sediment drift (north of the MTF) and the Svyatogor sediment drift (south of the MFT), from 11 m.y ago till present day. MTF: Molloy transform fault, MFZ: Molloy fracture zone, MR: Molloy Ridge, KR: Knipovich Ridge, WSC: West Spitsbergen Current. Dashed lines indicate magnetic anomaly chrons. White axis north of the MTF indicate the eastward growth of the drift (Johnson et al., 2015)

YP-3 is the youngest sedimentary unit with the base of the stratigraphy dated to the Pleistocene (Table 1). Internal structures reflect deposition during a changing glacial regime (Knies et al., 2009; Schlüter & Hinz, 1978). These structures consist of muds that alternate with turbidites and sands. The transition from YP-3 to YP-2 is marked by a distinct unconformity (Schlüter & Hinz, 1978). YP-2 is of Pleistocene to Pliocene age (Knies et al., 2009; Mattingsdal et al., 2014) (Table 1). The unit is found to be generally comprised of slump masses, and is characterized by diffractions, as well as discontinuous and irregular reflectors (Schlüter & Hinz, 1978). A second unconformity marks the transition from YP-2 to YP-1. The YP-1 stratigraphic unit is from Pliocene to Miocene age (Table 1), and deposited directly on oceanic crust (Knies et al., 2009). Johnson et al. (2015) reported that this sequence encompass synrift and post-rift structures. The crust beneath the Svyatogor Ridge is younger than that below the Vestnesa ridge (Figure 11). Due to this age difference, the YP-1 sedimentary sequence might not be present here.

Stratigraphic Unit	Age Range	Epoch	Depositional Environment
YP-3	~1.5 Ma	Pleistocene	Contourite deposition with glacial influence and erosion from ice (berg and/or grounded)
YP-2	2.7- ~1.5 Ma	Pleistocene - Pliocene	Contourite deposition with glacial influence
YP-1	~11- 2.7 Ma	Pliocene - Miocene	Contourite deposition

Table 1. Stratigraphic units with corresponding age and epoch, as well as depositional environment for the Yermak Plateau as presented by Knies et al. (2009) and Mattingsdal et al. (2014)

2.2.2 Crustal Structure

The crustal structure of the Knipovich Ridge can be divided into three oceanic layers, hereby referred to as Layer 1, Layer 2, and Layer 3 (Kandilarov et al., 2010; Kandilarov et al., 2008). Oceanic Layer 1 is magmatic crust, directly underlying sedimentary layers. Layer 2 is an extrusive layer, consisting of basaltic rock, and is considered normal oceanic crust (Kandilarov et al., 2010). The thickness of this layer varies and thins out from ~3km at the ridge axis to below 1km. Seismic velocities of this layer is found to be low, and varies from 2.5-4.0 km/s. This layer was found to be influenced by fractures, cracks, fluid circulation and possible thermal expansion (Kandilarov et al., 2010). Oceanic Layer 3 consist of gabbro. This layer were found to be thermally expanded with possible serpentinization (Kandilarov et al., 2010). The thickness of this layer varies from less than 2 km to about 7 km. Seismic velocity of Layer 3 shows little variations and found to be around 6 km/s. The low seismic velocities in vicinity to the ridge of this layer were thought to be a result of seawater circulation, fractures and fissures, thermal expansion and possibly serpentinization (Kandilarov et al., 2010). A sketch of the oceanic crust of the Knipovich Ridge as well as an adjacent tectonic setting is illustrated in Figure 12. This figure shows a setting which is located south of the area of interest here, and may therefore have deviations from that found further north.

Never the less, this illustration shows the general crust with serpentinization and fractures reported above to be found in the northern Knipovich.

The low thickness of the crust in the northern Knipovich Ridge is a result of low rates of spreading according to White, McKenzie, and O'Nions (1992). The vast majority of the earth's oceanic ridge systems have spreading rates of more than 15 mm/yr, often ~20 mm/yr. This spreading rate generates an average of 7.1 ± 0.8 km thick crust (White et al., 1992). White et al. (1992) found that the thickness of crust showed very little variations at full spreading, but at lower rates of spreading, the thickness of the oceanic crust decreases significantly. They reported that this decrease might result from the conductive heat loss from the mantle underlying the spreading axes.

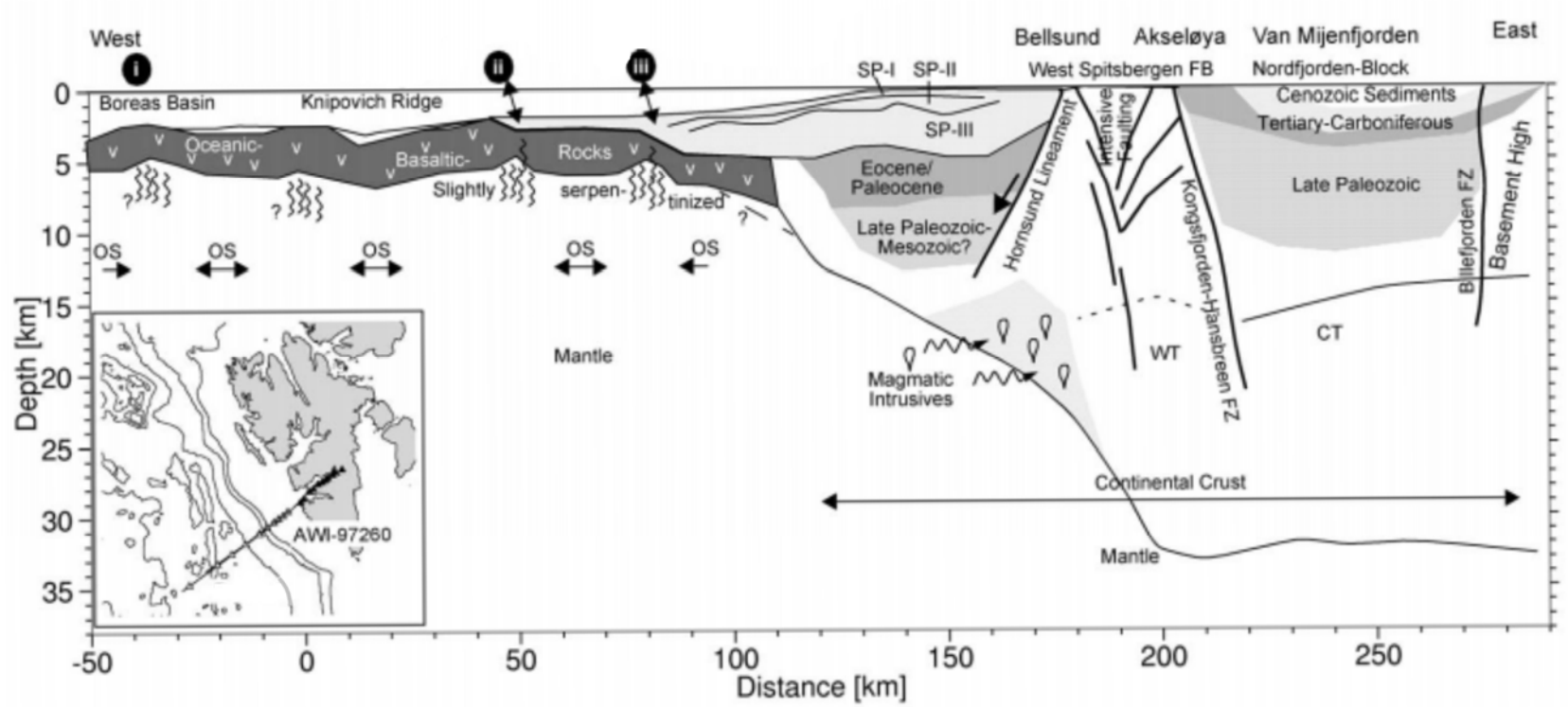

Figure 12. Interpretation of a velocity model by (Oliver Ritzmann, Jokat, Mjelde, & Shimamura, 2002). The location of this transect is imaged as AWI-97260 in the map. White color indicate crystalline continental crust and dark grey indicates oceanic crust. The sedimentary stratigraphic units SP-1, SP-2 and SP-3 are indicated. Black circles i to iii indicates thinning of oceanic crust in correspondence to crustal topography (black arrows). OS: Oceanic Segments, WT: Western Terrane, and CT: Central Terrane of Svalbard. Modified from (Oliver Ritzmann et al., 2002)

3 Data and Methods

The data used in this thesis consist of raw seismic data in a SEG-D format, a finished processed line (referred later to as Line 12, and a line that fills a gap in this line), bathymetric data, and four major regional stratigraphic boundaries resulting from a correlation with ODP-site 909 (Myhre, Thiede, & Firth, 1995). The stratigraphic correlation was kindly provided by Jochen Knies from NGU and Rune Mattingsdal from NPD.

3.1 Seismic Reflection Data

High-resolution multichannel seismic reflection data was acquired with the P-Cable system configured for 2D surveys during a field campaign with R/V Helmer Hanssen in 2014. The gun system used consisted of 2xmini-GI (15/15 in3) & (40/40 in3) with a shooting pressure of ~160-170 bar and shooting rate of 5-6 sec.

3.1.1 2D Multichannel Seismic Data

The high-resolution seismic data consist of 15 two-dimensional (2D) seismic lines gathered in the northern area of the Knipovich Ridge, on the western side of Svalbard. The processing of 13 of these lines is presented in chapter 4. Two additional lines, which cross the Molloy Transform (referred to as Line 12, and a line that fills a gap in in Line 12) were acquired during a later field campaign, and included in the interpretation. Figure 14 shows the relative position of these lines.

The survey in which the seismic 2D data was gathered consisted of one large solid-state steamer of 100 m, composed of four individual streamers each of 25 meters. Each of these four streamers have eight channels, 32 channels in total. The gun system has a perpendicular offset of 10 m relative to the streamer. Figure 13 illustrates the acquisition geometry of this survey. Speed of the vessel during acquisition was ~4kn.

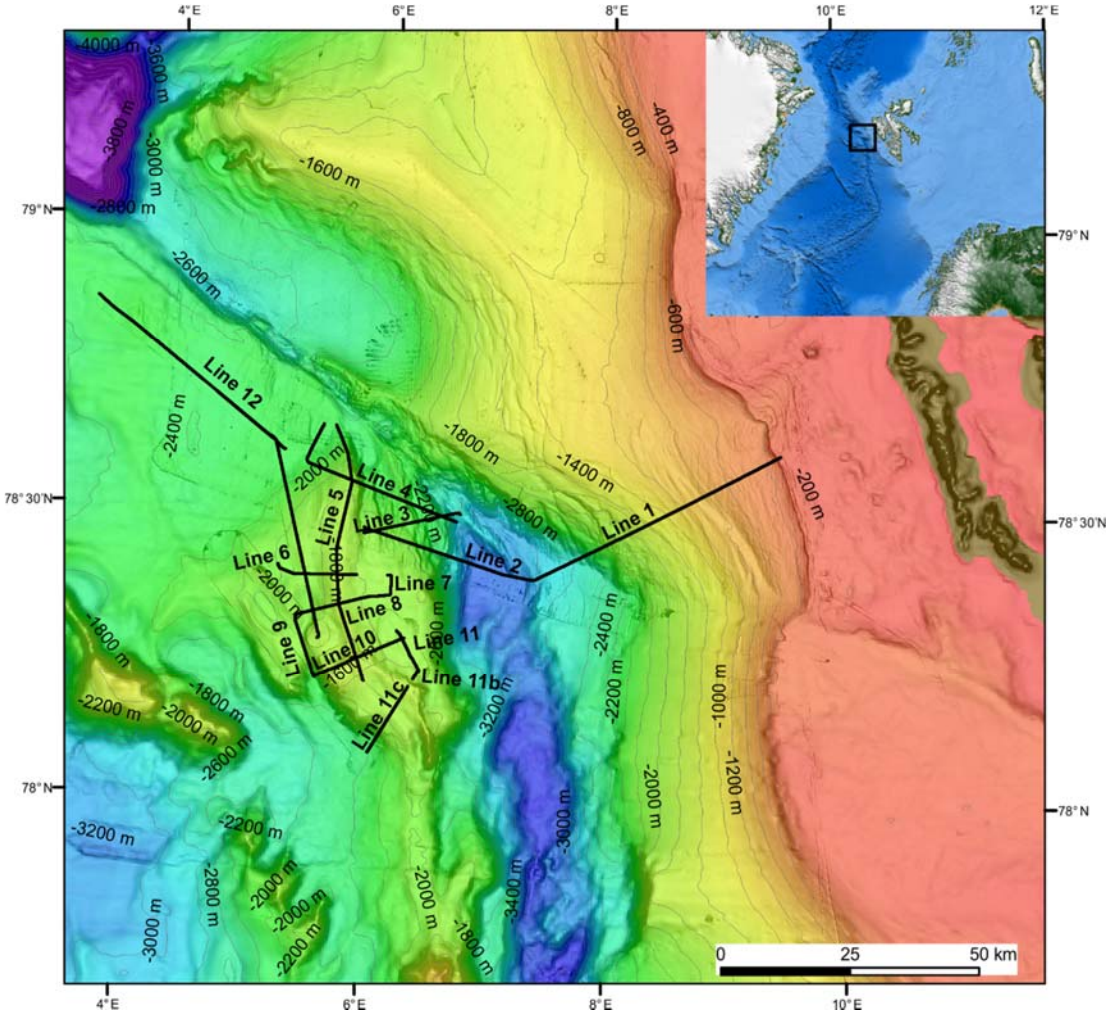

Figure 14. Overview of the relative positions of all 15 seismic lines composing the high-resolution seismic data used. Regional location of these lines is indicated in upper right corner with a black box.

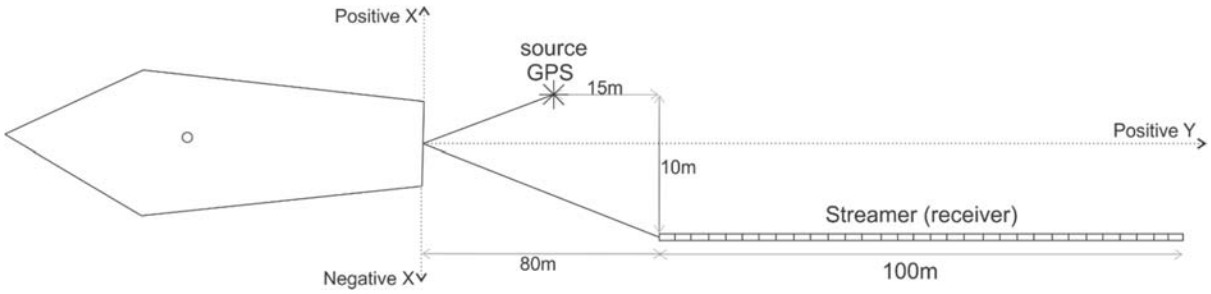

Figure 13. Illustration of the acquisition geometry used on the field campaign with R/V Helmer Hanssen in 2014. The receiver hydrophone have a length of 100m, 80m behind the vessel. The gun system offsets the streamer with 10m and is towed 65m behind the vessel. The positive and negative axes, as well as the location of the GPS, is used as reference for the direction of offsets in regards to the geometry used for processing.

3.1.2 Seismic Resolution

Seismic Resolution is a measure of how thick a layer needs to be in order to be visual on seismic records (Rafaelsen, 2005; Upadhyay, 2013).

When calculating seismic resolution the dominating frequency is commonly used (Rafaelsen, 2005). Figure 15 shows a spectrum analysis of the 2D multichannel seismic data. This spectrum shows that the peak frequency of the data lies at approximately 80 Hz.

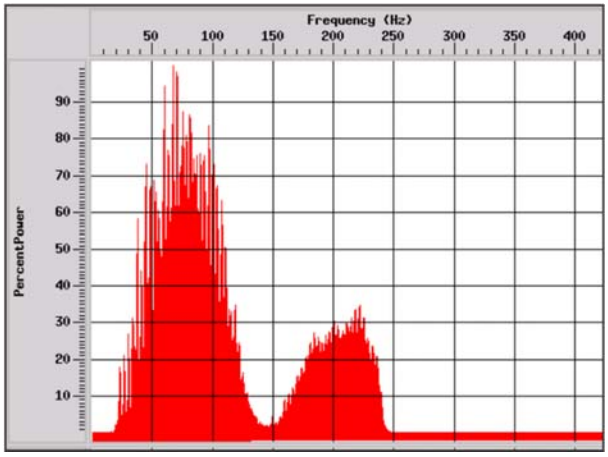

Figure 15. Spectral analysis from the 2D high-resolution multichannel seismic data, after filtering.

3.1.2.1 Vertical Resolution

Vertical resolution operates with the seismic data's ability to separate two reflecting surfaces closely spaced together. The controlling factors of the vertical resolution is the relation between wavelength and vertical distance between two surfaces (Upadhyay, 2013). The *resolvable limit* is the minimum separation thickness between two surfaces to differentiate them in a seismic record. This limit is commonly ¼ of the wavelength (Figure 16), but may be as small as λ/30 (Upadhyay, 2013).

3.1.2.2 Horizontal Resolution

Horizontal resolution operates with how large the horizontal extent of a structure needs to be in order to be visible on the seismic record (Upadhyay, 2013). On unmigrated sections, this width is often taken to be width of the first *Fresnel zone,* the extent of the circular area in which the wavefront is reflected from (Andreassen, 2009). Energy spread within the Fresnel zone is focused after migration of the data through re-arranging misplaced reflections (more on migration in section 4.2.7). This will have an improvement of ¼ wavelength on the horizontal resolution (Rafaelsen, 2005). This means that on a perfectly migrated section, the horizontal resolution will in theory be equal to the vertical resolution. The diameter of the zone is increasing with depth, lower frequency and increasing velocity, which can be seen from the equation of rf in Figure 16. Resolution is

decreasing proportional with increasing diameter (Andreassen, 2009). Table 2 shows the wavelength, vertical resolution and radius of the Fresnel zone calculated for the seafloor at the crest of the Svyatogor Ridge.

Wavelength: $\lambda = V/F$

Vertical Resolution: $\lambda/4$

Magnitude of Fresnel Zone: $rf = V/2\ (T/F)^{1/2}$

λ = Wavelength (m)
F = Seismic frequency (Hz)
V = Seismic velocity (m/s)
T = Two-way travel time (s)
rf = Radius of the Fresnel Zone (m)

Figure 16. Equations for calculation of wavelength, vertical resolution, and the magnitude (radius) of the Fresnel Zone. Based on information from Andreassen (2009) and Rafaelsen (2005).

	Wavelength	Vertical Resolution	Radius of the Fresnel Zone
Crest of the Svyatogor Ridge	18.7 m	4.7 m	121.5 m

Table 2. Calculations of wavelength, vertical resolution and the radius of the Fresnel Zone of the crest of the Svyatogor Ridge. Seismic velocity: 1500 m/s, TWT: 2.1 s, seismic frequency: 80 Hz.

3.2 Bathymetric Data

Bathymetric data of the Svyatogor Ridge was acquired during the R/V Helmer Hanssen field campaign in 2014 using a Kongsberg Simrad EM300 multibeam echo sounder.

3.2.1 Kongsberg Simrad EM300

The Kongsberg Simrad EM300 sends pulses of acoustic energy from a transducer in the hull of the vessel. These pulses have a sonar frequency of 30 kHz, and produces a fanned shape narrow beam with a high range towards the seafloor. The beam is composed of 135 single beams with a width of 1 degree per ping. The resulting beam have an angular coverage of 150 degrees and maps the morphology and acoustic backscatter of the seafloor in water depths from 10m to 5000m.

Optimal resolution is dependent on water depth and sediments on the seafloor. Varying pulse length and range sampling for water depth, and swath width for sediments as well as water depth correct for these variables. In general, a swath width of 5 times the water depth is used for shallow waters (< 500m) and a width of 4-5 km is used for depths down to 2000m.

3.2.2 Svyatogor Ridge Multibeam Survey

During the 2014 field campaign, the multibeam data was recorded using a WGS-84 datum. During the survey, the following parameters were logged: depth, seabed imaging, vessel position, vessel attitude, and sound speed. Range and angle data was converted to xyz triplets, and corrections applied for sound speed and vessel attitude variations. The transducer in the hull of the vessel is protected from contact with ice with a protective housing. This housing attenuates the amplitudes slightly at approximately 6dB.

Surface interpolation and conversion from depth to TWT was done using Petrel Software in order to correlate bathymetric data with seismic data. The algorithm used to create the bathymetric surface was a convergent interpolation, a standard algorithm in Petrel. The acoustic velocity used for this conversion is 1482 m/s. The bathymetric data after these applications is illustrated in Figure 17a. Figure 17b shows the relative position of seismic data to bathymetric data, and the regional location of the data. This polygon outline (pink) of the bathymetric data is later used to indicate locations of seismic profiles.

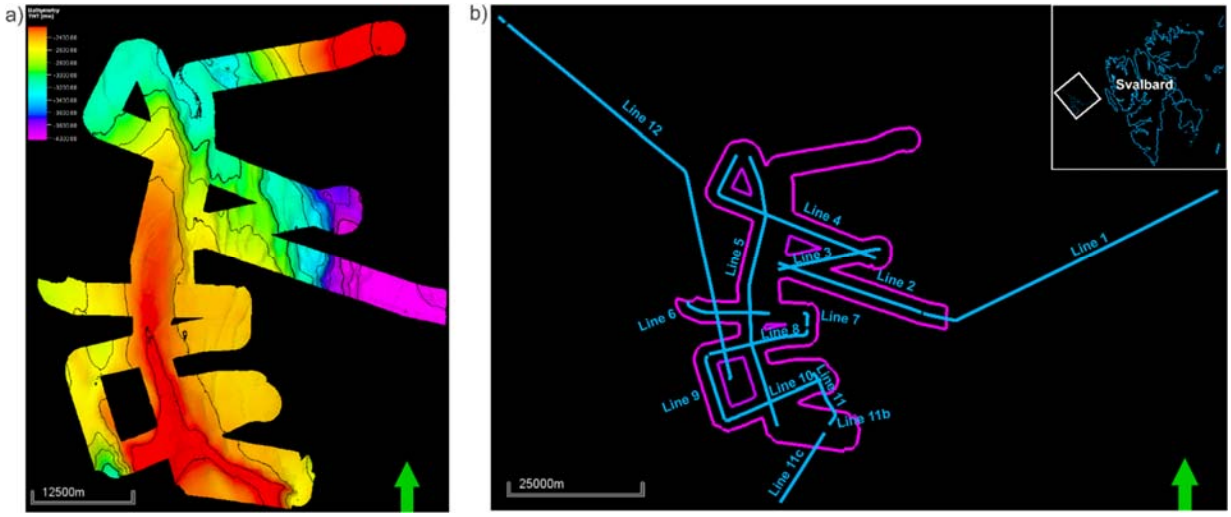

Figure 17. a) Multibeam bathymetric data gathered from the Svyatogor Ridge. Data imaged after convergent interpolation and depth conversion. Color differences corresponds to differences in depth as showed in the legend in upper left corner. b) Locations of seismic data relative to the position of bathymetric data. Regional location indicated in upper right corner.

3.3 Processing Software's

Two processing software's have been used to process the 2D high-resolution multichannel data. For initial processing of headers and geometry the processing software RadExPro, provided by Deco Geophysical Software Company, have been used, and for attenuation of noise and enhancement of signals SeisSpace ProMAX, provided by Landmark, a subsidiary of Halliburton, have been used. Chapter 4 provides a full overview of the processing flow used.

3.3.1 RadExPro

Raw seismic data in SEG-D format was imported to the RadExPro software where adjustments as trace header math and recording delays were accounted for. Navigation files holding coordinates, shot numbers and times of the data was imported and merged with SEG-D data to define the geometry of the data. These processes was done in RadExPro due to the software`s compatibility with the short offset, high-frequency data. The seismic data was exported in SEG-Y format.

3.3.2 SeisSpace ProMAX

SEG-Y files have been imported to SeisSpace ProMAX from RadExPro for continuation and completeness of processing. This includes processing with the aim of attenuation of noise and

enhancement of signals of interest. Figure 20 and Figure 21 illustrating spectral analysis, as well as Table 4 showing a velocity model is captured directly from this software.

3.4 Interpretation and Visualization Software

SEG-Y files of processed 2D lines have been imported and integrated with multibeam bathymetric data in the Petrel Software, provided by Schlumberger. All seismic- and bathymetric data is interpreted using Petrel (2014 edition). Petrel provides opportunities for both visualization and interpretation of processed seismic data.

3.4.1 Petrel Software

All figures imaging seismic data and bathymetric data are captured using the Petrel Software. Seismic data is illustrated with default settings for the colour spectra for reflection amplitudes. Positive amplitudes have colour spectra that ranges from red to yellow, where yellow indicates the highest positive. Negative amplitudes have colour spectra from dark blue to light blue, where light blue indicates the highest negative amplitudes. Zero and near zero amplitudes ranges in a white-grey spectra. Numerical values from reflection amplitude legend are not of great interest, and therefore removed.

Seismic attributes and seismic horizon is two functions provided by Petrel, which is used here to enhance specific sections in the seismic and to track reflections in the subsurface.

3.4.1.1 Seismic Attributes

Seismic volume attributes used are Trace AGC[5] and Structural Smoothing. *Trace AGS* have been used to enhance reflections deeper in the seismic profiles. This is used for structural interpretations from the transition from sedimentary section to basement. *Structural Smoothing* is used to compensate for effects of Trace AGC. It increase the continuity of reflectors that might be lost from applying a Trace AGC. For figures illustrating seismic sections in which these attributes have been used, it is specified in the figure caption.

[5] AGC – Automatic Gain Control

3.4.1.2 Seismic Horizon

Seismic horizons have been used to trace stratigraphic boundaries from the correlated ODP borehole data. For this tracking, a manual interpretation method has been used to ensure full control over the interpretation. This proved important, as opposed to a guided auto tracking, as the data often shows discontinuous layering and weak amplitudes in the lower parts of the seismic profiles, and therefore requires interpretation to track.

4 Processing of 2D Seismic Multi-Channel Data

The main objective of seismic processing is to enhance desired information in a seismic section to produce a seismic image of the subsurface that reveal true geological structures and a good signal to noise ratio (Al-Shuhail, 2011; Zhou, 2014).

The general sequence of processing steps is called a processing flow. Conventional steps often include stacking, sorting, velocity analysis, migration etc. (Zhou, 2014). The main processing flow applied in this study is shown in Table 3 below.

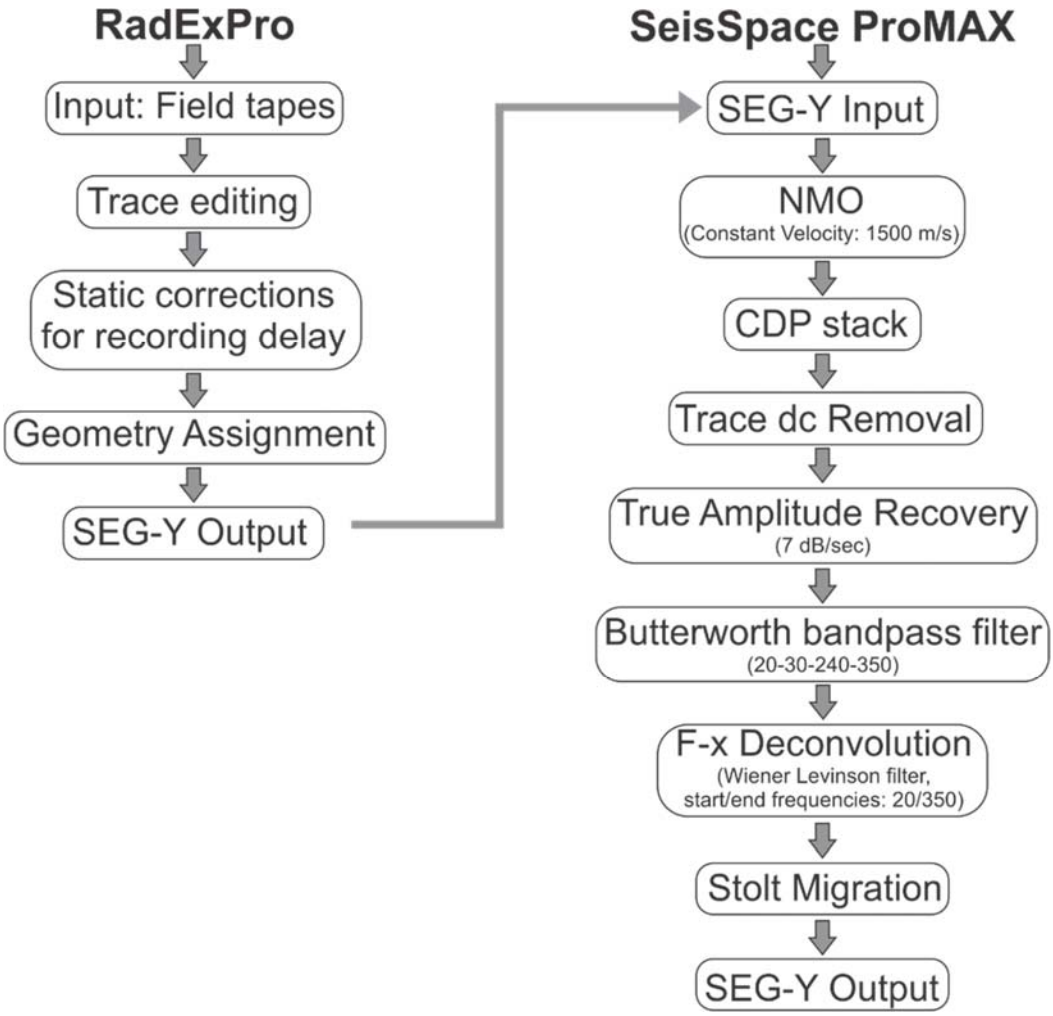

Table 3. Flow chart showing the general processing steps used for the 2D multi-channel seismic data

4.1 Geometry Assignment and Trace Editing

During acquisition of the seismic lines there were variations in sampling interval, water depths (some to the extent where adjustments in initial recording delay were necessary), and recording length. These variables have been accounted for in RadExPro, in addition to a geometry assignment.

The vast majority of the seismic data was during acquisition recorded at a 0.25ms (0.00025s) sample interval. Sampling is taking small data points on an analogous signal. The higher the interval between these samples (sample interval), the more accurately the signals will be represented. The minimum amount of samples required to get this accurate representation is two samples per cycle, though the recommended amount is four (Andreassen, 2009; Wiederhold, 2006). The theoretical maximum of frequencies that can accurately be restored is called the Nyquist frequency. The Nyquist frequency is defined as half the sampling frequency (Andreassen, 2009; Wiederhold, 2006);

$$Nyquist\ ferquency\ (f_{Nyq}) = \frac{1}{2\Delta t}$$

This yields a theoretical maximum frequency of 2000Hz that can accurately be recorded in this dataset;

$$Sampling\ frequency\ (f) = \frac{1}{Period\ (T)} = \frac{1}{0.00025s} = 4000Hz$$

$$f_{Nyq} = \frac{Sampling\ frequency\ (f)}{2} = \frac{4000Hz}{2} = 2000Hz$$

Frequencies above the Nyquist frequency can experience aliasing e.g. loss of definition and reappearance as false low frequencies (Andreassen, 2009; Wiederhold, 2006). As shown in Figure 20 the frequency domain for this data lies between 20Hz and 350Hz i.e. below the Nyquist frequency.

During acquisition, increasing water depth caused a necessity of variation in sampling interval. With a great increase in water depth, sampling interval was raised to 0.5ms. This was done due to disk space restrictions. With a higher sampling interval, less data is retrieved.

For variations in recording delay, a static shift correction, in the form of a bulk shift, was applied, and trace length adjusted for this. Static correction is a fixed time correction that can be applied to an entire trace. Sheriff (1991) defined static corrections as *"corrections applied to seismic data to compensate for the effects of variations in elevation, weathering thickness, weathering velocity, or reference to a datum"*. Here the shift compensate for the cutting of water column samples during acquisition.

Geometry assignment is based on information on receiver geometry from the survey protocol kept during acquisition, and all ship navigation data (time and ship GPS) is imported. An illustration of the field geometry for the survey in which this data was acquired is shown in Figure 13 in chapter 3.

4.2 Normal Moveout (NMO) and Stacking

Andreassen (2009) gives this definition of Normal moveout; "*Normal Moveout (NMO) = is the difference between two-way time at a given offset and the two-way zero-offset time"*

This means that the difference in arrival time of wave propagation between the first and last receiver induces a delay for a horizontal surface. Plotting the arrival times with increasing offset will have a hyperbolic shape. Normal moveout corrects for this hyperbolic shape and brings the reflections back up horizontally (Figure 18). The NMO is dependent on a series of variables that include the velocity above the reflector, offset, two-way zero offset time (in association with reflection event), reflector dip, degree of complexity (of near surface and medium above reflector), and the orientation of the seismic line relative to the reflector dip (Andreassen, 2009). Appropriate moveout velocity is important in order to achieve a horizontal reflection after NMO correction. Velocities lower than the appropriate value can result in an overcorrected gather, and hence too high velocities can result in under-corrected gather (Andreassen, 2009).

The SeisSpace software applies normal moveout corrections according to this formula:

$$T_x = \sqrt{\left[T_0^2 + \left(\frac{X}{V}\right)^2\right]}$$

T_x = Reflection time of a seismic event due to NMO effects

T_0 = Zero offset reflection time

X = Source-receiver offset distance

V = NMO or stacking velocity

The operation in which this equation is based on calculates and applies NMO corrections to CDP traces using linear interpolation. A sample-by sample velocity function allows interpolation between several locations of different velocities. To do these assumptions of a velocity that will be appropriate it is necessary to do some interpretations on the lithology of the area. O. Ritzmann et al. (2004) did a study of velocity structures in the Svyatogor area. This gives insight on low velocities in the upper sedimentary layers, which functioned as a basis for the constant velocity function of 1500m/s used for the 2D seismic data here. A constant velocity is enough to correct for the NMO at different depths in this dataset due to the short offset (seen from acquisition geometry in Figure 13).

Stacking in seismic processing means that multiple traces are summed together to form one single trace (Figure 18). The purpose of this step is to enhance the signal to noise ratio (SNR) (Zhou, 2014). Noise in seismic data is all parts of the signal that are unrelated to the primary reflections. The noise in the signals will be random, and by stacking traces together, some of this noise is cancelled out. In addition, the stacking process increases the strength of primary reflection. These two functions will result in an increase of the SNR (Andreassen, 2009). The number of traces that are stacked together is the fold. The size of the data is therefore reduced by the factor of the fold (Zhou, 2014). For this data, a CDP[6] stack was created. Each trace was sorted into bins. The width

[6] CDP – Common Depth Point

of the bins is usually half the receiver station ($\frac{100m}{32\ channels} = 3.125$), and therefore set to be 1.56 ($\frac{3.125}{2} = 1.5625$), which forms the CDP gather that are stacked to one trace (Zhou, 2014).

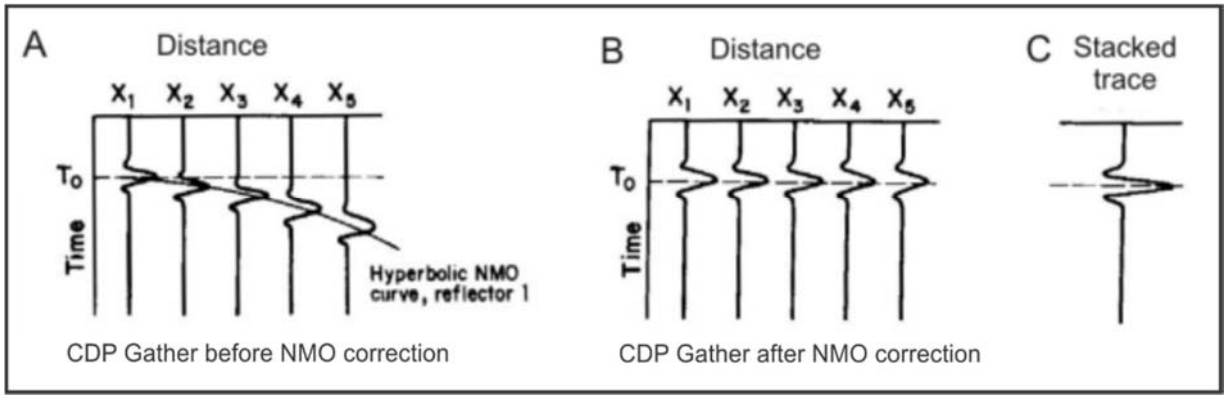

Figure 18. Illustration of the stacking process and normal moveout correction. A) CDP Gather before NMO correction. B) CDP Gather after NMO correction. C) Stacked trace. Modified from Andreassen (2009)

4.3 Signal Processing

4.3.1 Trace dc Removal

Trace dc Removal is a tool used to remove dc bias or offset from input traces (Rumpfhhuber, 2008). To calculate the level of the dc component in the data, the mean of the samples are used as the central value. This function is used in order to avoid amplitude values fluctuating with an offset above or below a centerline representing zero amplitude, as this can result in a presence of unwanted noise in the lowest frequencies.

4.3.2 True Amplitude Recovery

During processing of seismic data, one of the most important tasks is the reconstruction of amplitudes that have been distorted. This distortion can be summed in three categories: spherical divergence, absorption, and transmission loss (Russel, 1988). True Amplitude Recovery was applied to compensate for loss of amplitudes as a result of attenuation and wavefront spreading. True Amplitude Recovery was applied post stack due to short offsets and deep waters. This is achieved using a dB/sec correction with the gain correction: $g(t) = 10^{t \times C/20}$, where C is the dB/sec correction constant and t is time. The dB/sec correction constant used is 7dB/sec. In the seismic data used here, this tool provides a better imaging of the deeper parts of the data, revealing more features. This application can be seen on Figure 19 below where a seismic section without true amplitude recovery is shown on the left, and the same section with a gain using the correction constant of 7dB/sec on the right. The image on the right shows a significant increase in amplitudes

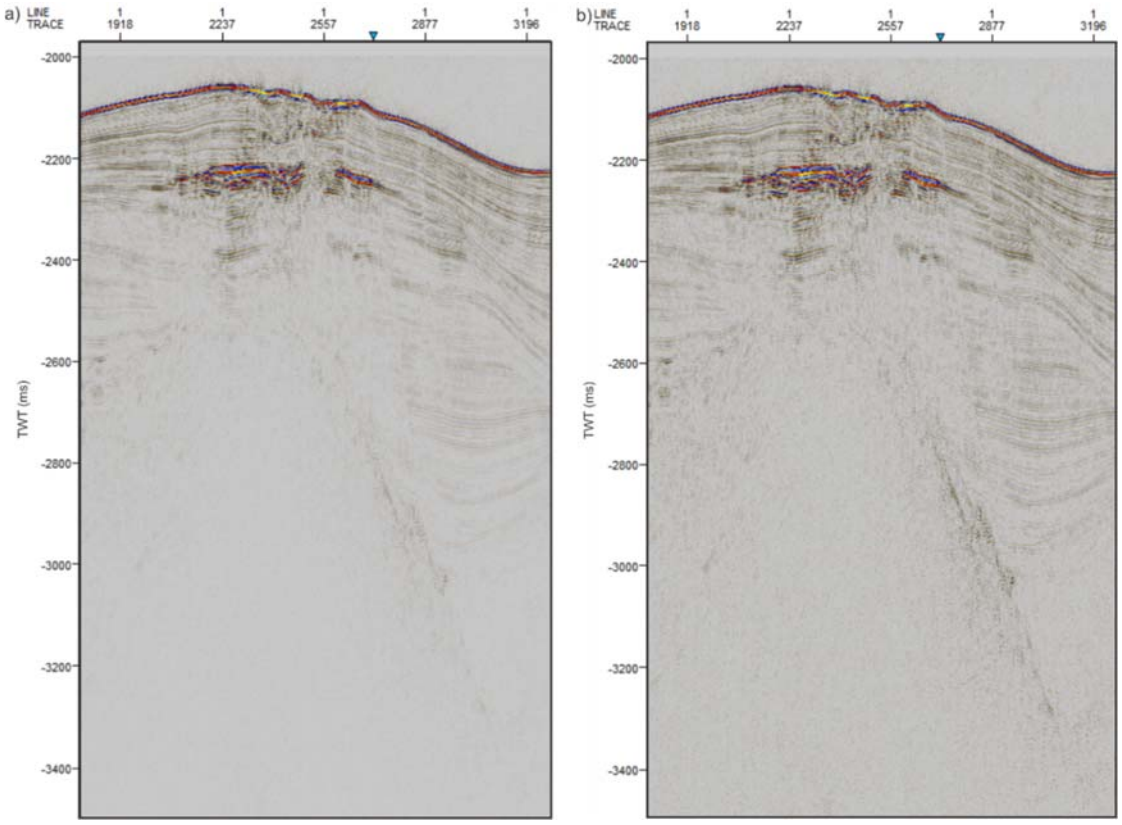

Figure 19. Seismic section imaging the effect of True Amplitude Recovery. a) Section without True Amplitude Recovery. b) Same section with True Amplitude (using a 7dB/sec correction constant).

that result in better imaging of the structures as far down as -3400ms (TWT[7]) as well as clearer layering through the whole section.

4.3.3 Filtering

Filtering is one way of reducing unwanted information that is considered noise in the data, and amplifying signals of interest (Al-Shuhail, 2011; Everett, 2013).

4.3.3.1 Butterworth bandpass filter

Bandpass filters uses specified bands that aims to attenuate amplitudes of frequency components of signals that lie outside these bands, and preserve the ones than lie inside (Everett, 2013). A bandpass filter applies a frequency filter to each trace that is imported. The Butterworth bandpass filter is arranged by four integers; 3dB low frequency – low slope – (-)3dB high frequency – high slope.

Figure 20 shows a spectral analysis of a 2D seismic line after True Amplitude Recovery was applied. In this graph, we see that the majority of the frequency content lies between 20- and 350Hz. The frequencies within this range contain the valuable information in the data, and the frequencies outside this band are to be filtered. The filter frequencies used to clean this spectra are; 20-30-240-350 Hz, and the result can be seen on Figure 21. In this figure, the frequencies below 20Hz and above 240Hz are greatly reduced i.e. low frequencies from surface waves and other unwanted noise do not influence the data as greatly.

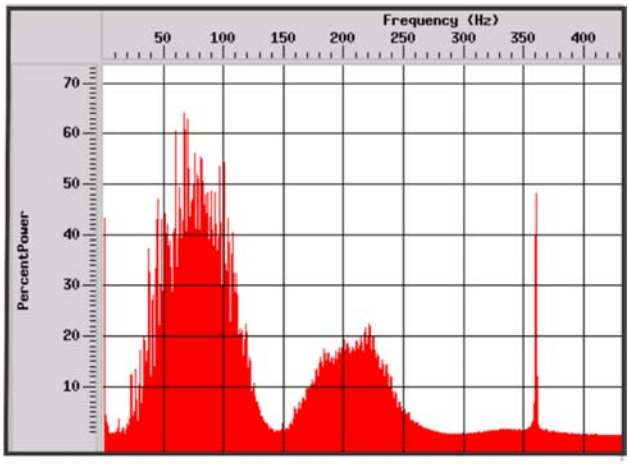

Figure 20. Spectrum analysis after the application of True Amplitude Recovery (7dB/sec)

[7] TWT – Two Way Travel Time

The frequency spectra shows a notch with its center at approximately 200Hz. This notch can indicate a ghost in the data. A ghost is a short-path multiple that originates when energy travels upward from the source and reflects back down to the receiver. A ghost notch can roughly be calculated by considering the travel times for energy from the source to the surface, and down again (Andreassen, 2009):

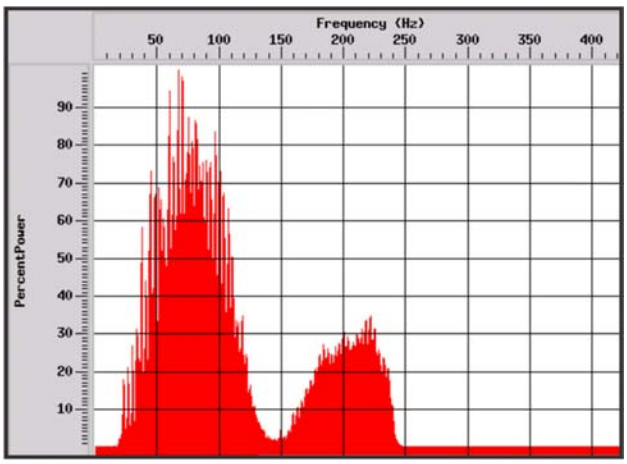

Figure 21. Spectrum analysis after the application of Butterworth bandpass filter using 20-30-240-350 integers

$$d = \frac{1}{2}\lambda \Longrightarrow \lambda = 2d = 2 \times 1.75m = 3.5m$$

d= source depth, λ= signal wavelength. This gives us the frequency in which a ghost will appear in the spectra:

$$f = \frac{V}{\lambda} = \frac{1500m/s}{3.5m} = 428.5$$

Where V is the P-wave velocity in water. This frequency is higher than the spectra where the notch lies, but cannot fully exclude the notch from being a ghost signal. The survey protocol gives information of good weather and calm seas, meaning that the fluctuations of streamer and gun should be at a minimum. The depth of the receiver can often be of importance to attenuate multiples, and the streamer depth used during acquisition (1.75m below sea-surface) can have been deeper than what was protocolled.

4.4 Data Enhancement and Noise Suppression

4.4.1 F-X Deconvolution

For every trace in an input ensample or stacked data, the f-x Deconvolution applies a Fourier Transform. In a specific range of frequencies, it will apply a complex Wiener Levinson prediction filter. This is done in order to predict the signal one trace beforehand. The resulting frequency trace will be inverse transformed back to the time domain. The frequency range used for the seismic data

is the 3dB low frequency and high slope values from the Butterworth bandpass filtering, yielding a start frequency of 20Hz and end frequency of 350Hz.

The result of the f-x Deconvolution is imaged in Figure 22 below. On the left, Figure 22a), shows a seismic section after bandpass filtering and True Amplitude Recovery, and on the right (Figure 22b) is the same section after the application of f-x Deconvolution. The layering in the images shows a substantial difference. Left image is noisier, and the f-x deconvolution has removed this noise as seen in the image on the right.

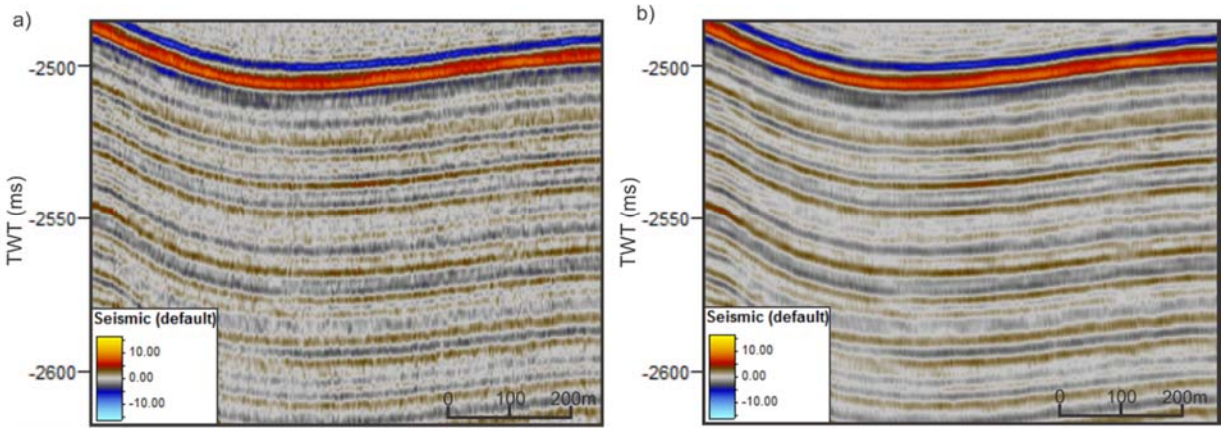

Figure 22. Illustration of the effects of f-x Deconvolution. a) Seismic section before the application of f-x Deconvolution. b) The same seismic section after f-x Deconvolution have been applied

4.5 Migration

Migration moves dipping reflections to their correct positions. When interpreting reflections, knowing from which direction waves are propagating can be difficult. For this reason, all reflections are placed beneath the point at which they are recorded. For some features, this plotting will be incorrect, as dipping planes will reflect energy sideways. For such events, like fault planes, their true position will be to the side of where they are placed. Migration corrects for these incorrectly placed dipping reflections and moves them to their right position (Brown, Hawkesworth, & Wilson, 1992).

F-k migration (Stolt migration) transforms the seismic data to the FK domain and applies migration equations. This results in a vertical shift of data in the frequency axis and a transformation of this data onto the migrated dip (Zhou, 2014). For the f-k migration it is important to have an accurate as possible velocity model, as with any method of migration. O. Ritzmann et al. (2004) studied p-wave velocities on sedimentary cover east of the Molloy transform fault, and suggest 1.7-1.8 km s^{-1} for upper sediments. A velocity model using 1500m/s for sedimentary layers (interpreted to be the majority of the data) has proven to function well for the migration of this 2D seismic data. A more thorough analysis is carried out for data of specific interest, especially lines through the ridge crest showing higher amplitudes. Table 4 shows the velocity model used here. A result of migration using the velocity model in Table 4 is shown in Figure 23b). Figure 23a) shows scattering of energy in the form of diffractions. The Stolt migration corrects for these diffractions.

Mark Block	CDP	X Coor	Y Coor	TIME	VEL_INT
1	19702.0	421473.9	8686415.0	2000.0	1500.0
2	19702.0	421473.9	8686415.0	2800.0	2000.0
3	21654.0	427007.6	8688652.0	2000.0	1500.0
4	21654.0	427007.6	8688652.0	2600.0	2000.0
5	21798.0	427404.8	8688865.0	2000.0	1500.0
6	21798.0	427404.8	8688865.0	2500.0	2000.0
7	21875.0	427616.6	8688979.0	2000.0	1500.0
8	21875.0	427616.6	8688979.0	2200.0	1700.0
9	21875.0	427616.6	8688979.0	2300.0	1500.0
10	21875.0	427616.6	8688979.0	2400.0	2000.0
11	22210.0	428561.8	8689425.0	2000.0	1500.0
12	22210.0	428561.8	8689425.0	2600.0	2000.0
13	22454.0	429264.9	8689720.0	2000.0	1500.0
14	22454.0	429264.9	8689720.0	2800.0	2000.0
15	22627.0	429761.9	8689932.0	2000.0	1500.0
16	22627.0	429761.9	8689932.0	3000.0	2000.0
17	22881.0	430493.4	8690239.0	2000.0	1500.0
18	22881.0	430493.4	8690239.0	2800.0	2000.0
19	23117.0	431174.2	8690523.0	2000.0	1500.0
20	23117.0	431174.2	8690523.0	2800.0	2000.0
21	23475.0	432204.2	8690958.0	2000.0	1500.0

Table 4. Velocity model for Stolt migration

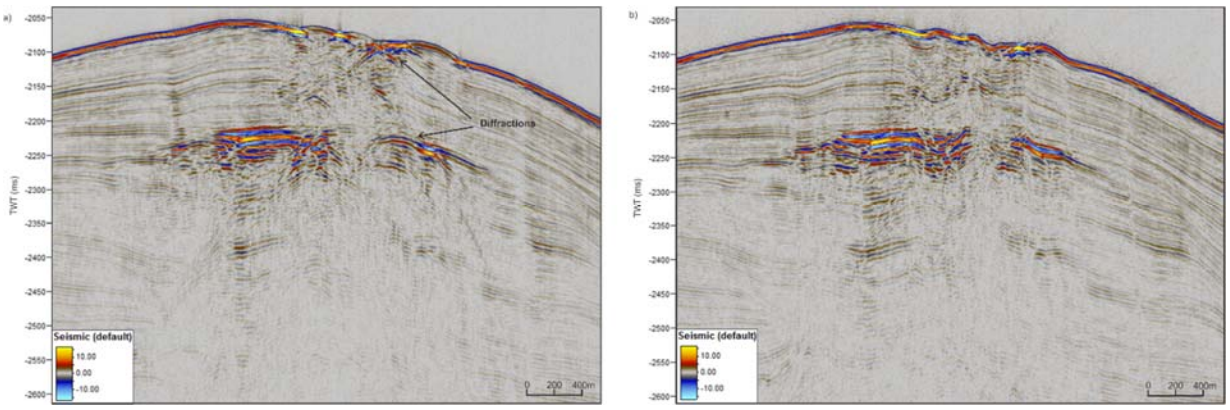

Figure 23. Seismic section illustrating the effect of Stolt fk migration and the velocity model in table 2. a) Seismic section without migration. b) The same seismic section with migration (using the velocity model in table 2)

4.6 Automatic Gain Control (AGC)

Gain control is often used in processing as a tool for removing or attenuating the influence of factors that are causing decay of amplitudes, and effectively improving the image of the data. This enhancement of data is achieved true balancing of variations in time-variant amplitudes. AGC is a gain control that is statistically based, and balances the amplitudes of a section, i.e., enhancing zones of weaker reflections (Yilmaz, 2000; Zhou, 2014). Because AGC is statistically based, it can be of harm to seismic data where the variations in amplitudes are of great importance (Zhou, 2014).

AGC is used here after f-x deconvolution for a small portion of the data where the seafloor and stratigraphy below contain amplitudes that are too weak for interpretational purposes. In Figure 24 below, the effects of this tool are illustrated. In Figure 24a), the amplitudes appear weak, and the stratigraphy is barely visible. Figure 24b) shows the same section after AGC have been applied, and shows a clearer stratigraphy below the seafloor.

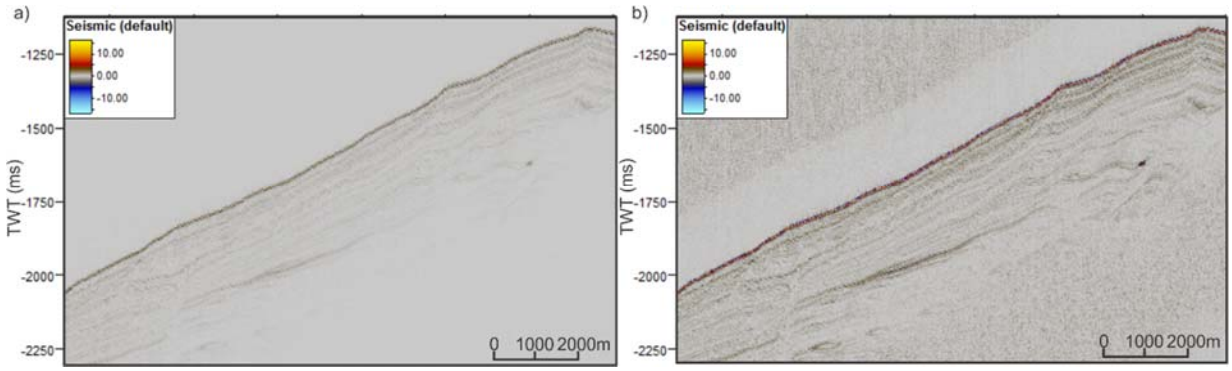

Figure 24. Illustration of AGC in a seismic section. a) Shows a section after f-x deconvolution have been applied, and b) shows the same section after AGC is applied.

4.7 Seismic Quality

There is always room for further processing of seismic data, and to greater improve the data. The type of quality enhancements used during the processing is dependent on the aims of interpretation (Zhou, 2014). In this data there are especially two processes that could have been considered; removing multiples (demultiple) and removing ghosts (deghosting). Deghosting was discussed in section 4.3.3, where it was improved using a Butterworth filter. Multiples occur in a small part of the data. On Figure 25, an image of how this is visualized in the data is illustrated. These multiples are very clearly a repetition of the seafloor, but does not disturb the real data too much as the penetration is shallower than the occurrence of the multiple. Removing multiples can be a comprehensive job, and was here not a priority, as the multiple does not interfere with any interpretations. Deghosting is also considered a job that is too comprehensive compared to the interpretational value it would result in.

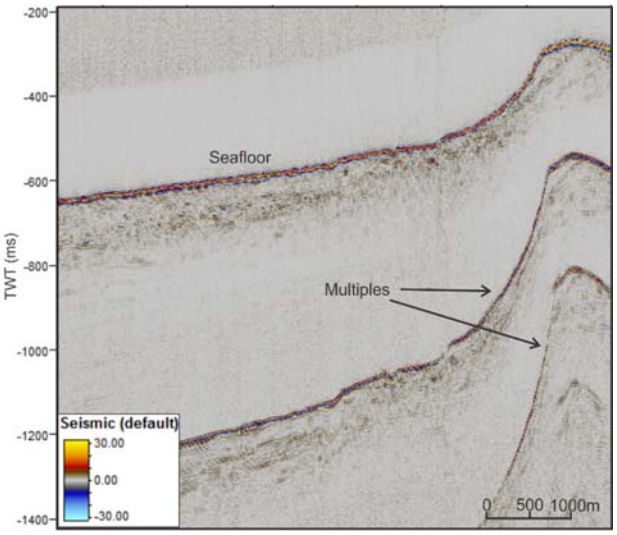

Figure 25. Illustration of multiples found in the 2D seismic data.

5 Results

The results presented are based on interpretations and observations of shapes and distribution of seismic anomalies using the Petrel Software. The high-resolution P-cable seismic processed and discussed in the previous chapter, as well as bathymetric data is used to interpret and map structural settings and fluid systems on the Svyatogor Ridge. Stratigraphic units are traced and interpreted using an interphase from a correlation with ODP site 909 (courtesy of Jochen Knies (NGU) and Rune Mattingsdal (NPD)).

5.1 Stratigraphy

A geological timeframe for the sedimentary units represented on the Yermak Plateau and Vestnesa Ridge have been carried out by Mattingsdal et al. (2014). The correlation from ODP Hole 909 (location in Figure 1) can provide age determination of the sedimentary units on Svyatogor Ridge, and a relative interpretation between the age of this drift and the Vestnesa sediment drift.

The boundary between the two stratigraphic units YP-3 and YP-2 is traced from the initial intersection with Line 12 (white circle in Figure 26a). The fill-in line is here used as aid to trace the boundary through the gap (Figure 26b). From Line 12 this boundary intersects with both Line 6 and 8 (marked with crosses on Line 12 in Figure 26a). The YP-3/YP-2 boundary for Line 10 is inferred from Line 8 which is adjacent and shows stratigraphic similarities in terms of high amplitude reflectors (lowermost occurring ~2900ms (TWT) for Line 10 and ~2900ms (TWT) for line 8). Line 5 intersects these three lines, and functions as a connection to the other seismic lines. Line 5 has limited penetration, below 350ms (TWT) beneath the seafloor, and is acquired at the crest of the ridge where the sedimentary deposition is thinner. This means that beyond Lines 12, 10, 8 and 6, the YP-3/YP-2 boundary is difficult to trace with a degree of accuracy.

Correlation of older seismic units, such as YP-1 found present at the Vestnesa Ridge, has been impossible as it junctions with Line 12 deeper than there is seismic data. As this unit is not traced to the ridge, there is an uncertainty of whether or not this unit is present at the ridge.

Stratigraphic unit YP-3 shows for the most part a well-defined stratigraphy with high amplitudes and continuous reflections on the walls of the ridge. Faulting and gas influence causes some

disturbance along the axis of the crest. Underlying YP-3 is the YP-2 unit. From the junction with Line 12 and through the perpendicular lines acquired from the crest of the ridge, this unit have a poorer resolution than YP-3 due to the greater depth. Both stratigraphic units are highly faulted, where faults often crosscuts both units. Faults through the ridge looks to be more prominent on the eastern side of the ridge. This side also show a trend of being more sedimented (Figure 29, Figure 30 and Figure 31Figure 31).

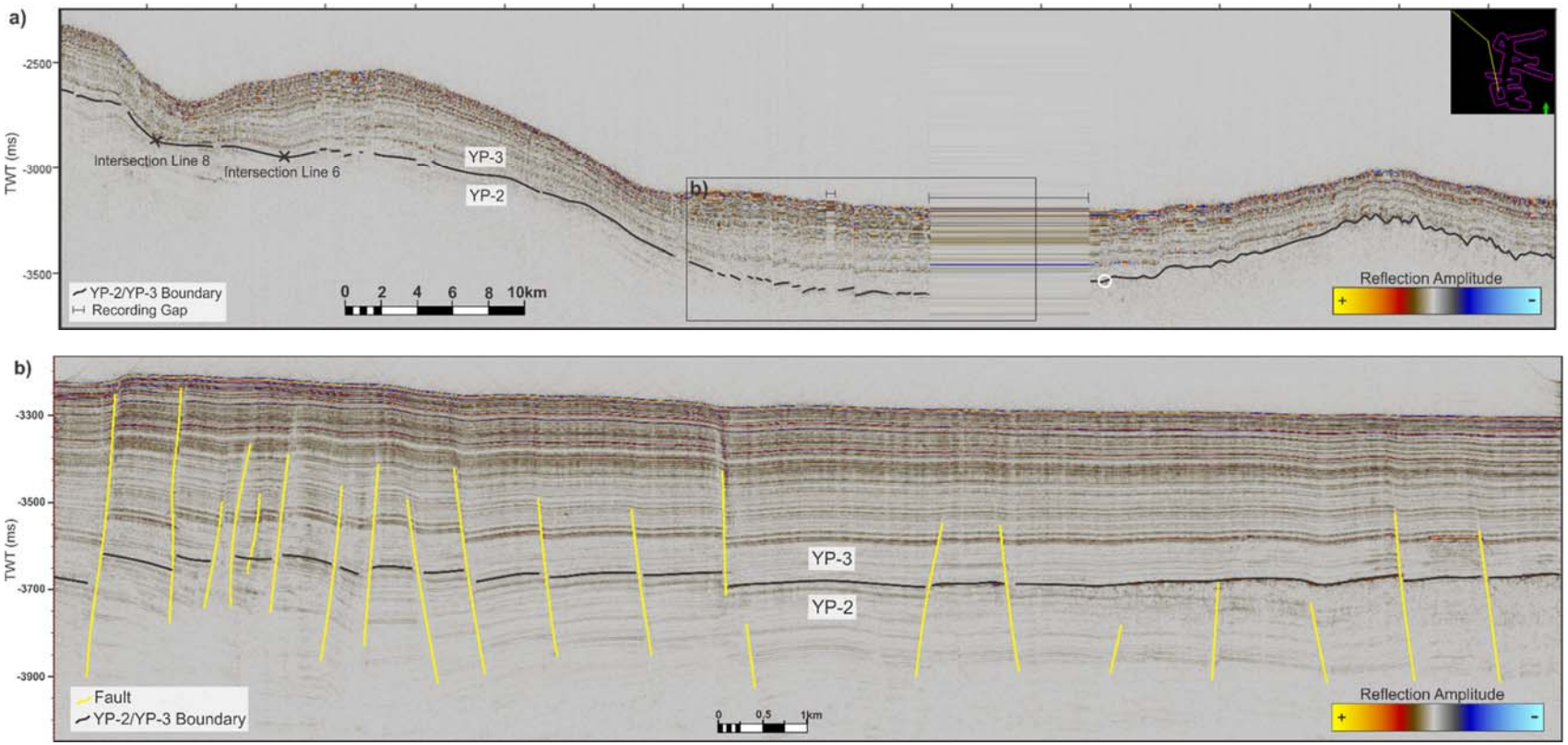

Figure 26. a) High resolution seismic Line 12. White circle indicates the intersection between Line 12 and the correlated boundary between stratigraphic units YP-3 and YP-2 by Jochen Knies (NGU) and Rune Mattingsdal (NPD). Black line indicates the interpreted continuation of this boundary. Two crosses on this interpreted boundary indicates the intersection with Lines 8 and 6. There are two recording gaps in this profile, the largest of approximately one hour of recording. This gap is attempted to fill inn during the CAGE cruise in October 2014, which is indicated by a black square, and imaged in b). b) This seismic profile fills some of the recording gap in Line 12. The same boundary as in a) is indicated here, and used as a tool for better interpretation for the continuation south of the white circle. This area is highly faulted which is indicated in this profile.

5.2 Faults

The 2D seismic data indicates that the Svyatogor Ridge is highly faulted. This is shown in the previous figure (Figure 26b), and is evident in several of the other processed seismic lines seen in figures in the following subchapters. Figure 29, Figure 30 and Figure 31 shows seismic profiles acquired perpendicular to the crest of the ridge where the stratigraphy is highly influenced by faults (indicated by yellow lines). These faults are seen to be steeply dipping with a downward displacement of the hanging wall, interpreted to be predominantly normal faults (Fossen, 2010), where the down-thrown blocks are generally on the eastern side of the faults. These faults extend from the lowermost stratigraphy and many reach close to the seafloor. Acoustic blanking in the lower zones on the seismic profiles limits the interpretation on the depth of the faults, although some faults can be seen displacing strata close to the basement in areas where there is deeper seismic penetration (Figure 27). Additionally, a number of faults create scarps on the seafloor, on the eastern side of the ridge, that are visible in the bathymetry data (Figure 33). In seismic Line 10, two of these scarps are seen (Figure 29). These faults are deep and displace basement. These faults have been interpreted to be detachment faults (Lister & Davis, 1989).

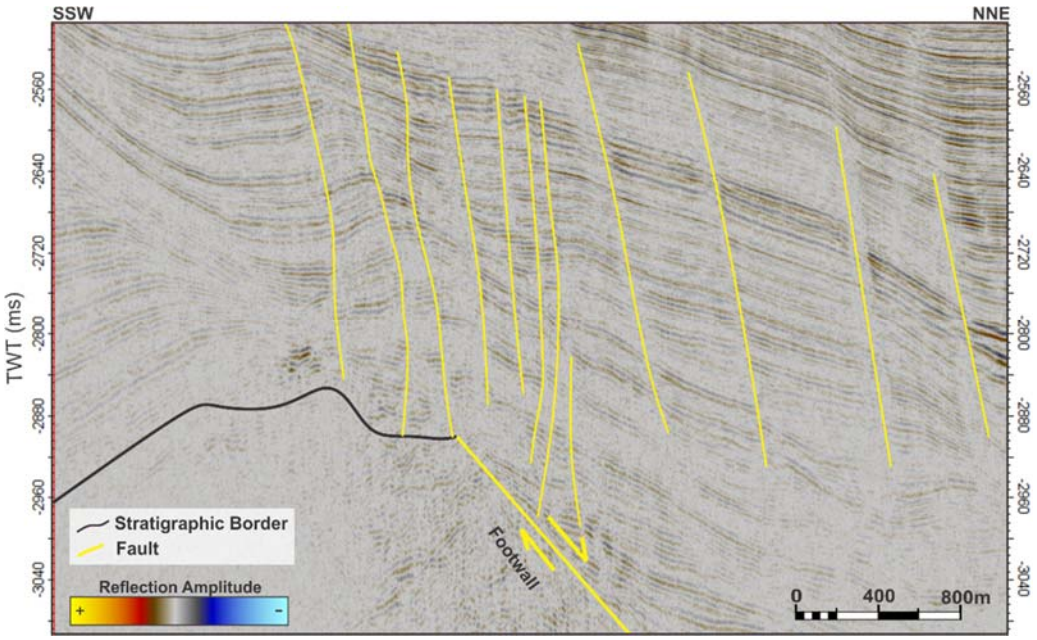

Figure 27. Seismic section of seismic Line 10, illustrating faults (yellow lines) displacing strata close to the basement (black line). Location of this section is indicated in figure 30.

The Svyatogor Ridge lies between the stress regimes of both the MTF and the Knipovich Ridge. The magnitude of tectonic influence from these stress regimes can be induced from an identification of the stress component on faults throughout the 2D seismic dataset, as well as bathymetry data. In the southern extent of the study area, fault are seen as steeply dipping, dip-slip, normal faults (Fossen, 2010) (Figure 27, Figure 29, Figure 30, Figure 31). In the northern extent of the study area, close to the MTF, fault are also seen as steeply dipping normal faults. However, in this area reflectors appear to have small antiforms on the up-thrown side, and synforms on the down-thrown side (Figure 28). Faults in either extension of the study area tend to strike parallel to the crest of the Svyatogor Ridge (Figure 33).

Antiforms and synforms are often indicative of a compressional regime, although dip-slip faults often indicate an extensional regime (Fossen, 2010). Figure 28, shows both these trends in proximity to each other. Throughout the dataset, dip-slip normal faults looks to be the dominant fault type. This can indicate that the Svyatogor Ridge have undergone an extensional regime with a compressional component. Figure 28 also shows a prominent rolling topography of the surface and of layers above the termination of the faults that can indicate deposition of sediments while active faulting.

Zones of higher amplitudes adjacent to faults (bright spots) is found on Line 2 (Figure 28). These features appear to only be adjacent to faults in the northern end of the dataset. Faults may act as migration pathways for subsurface fluids, but they can also act as traps where impermeable matter fills the zone of displacement or when faults brings a permeable layer adjacent an impermeable layer. Bright spots next to faults can indicate either of these scenarios (Selley, 1998).

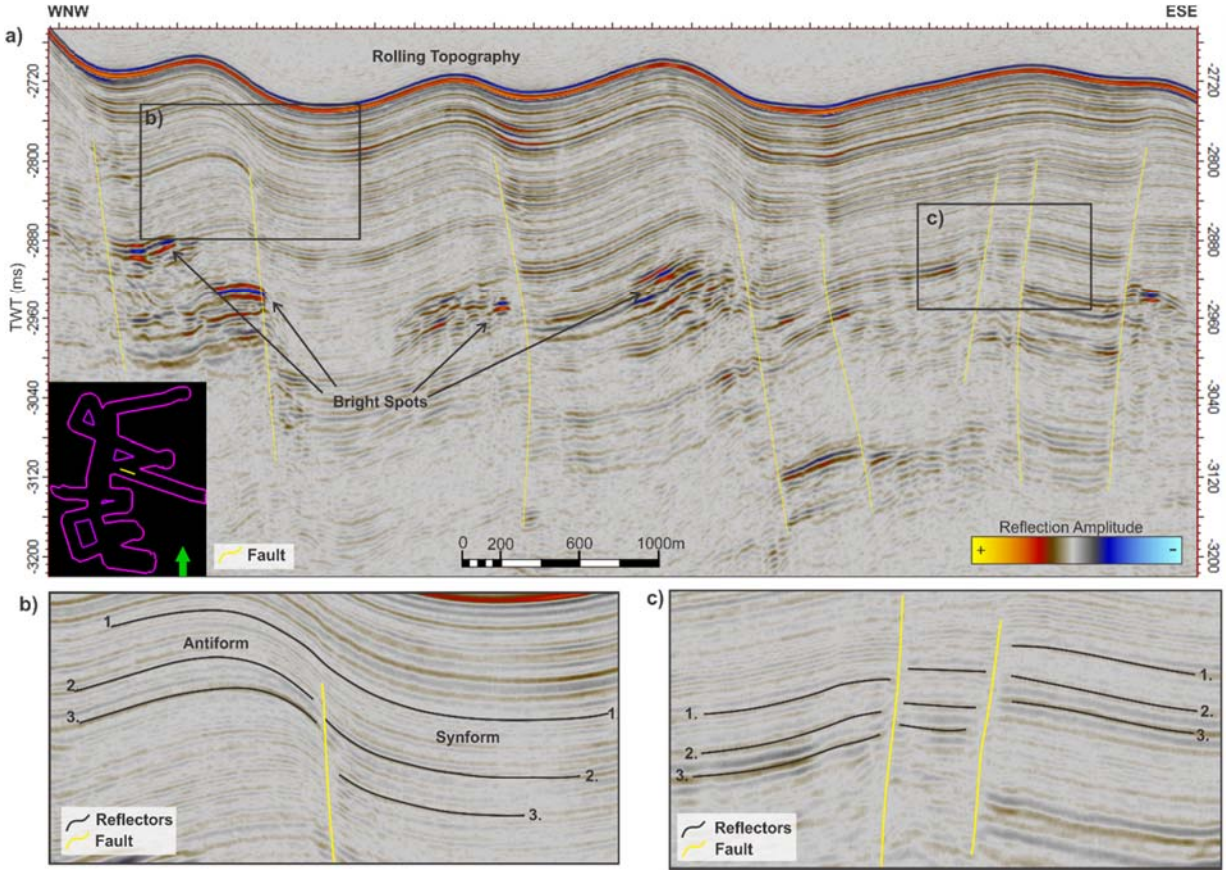

Figure 28. a) Section of 2D seismic Line 2, location indicated by yellow in bathymetry outline bottom left corner. The section shows a rolling topography on the seafloor, and a faulted subsurface with accumulations of high amplitudes. b) Antiforms and synforms adjacent faults. c) Dip-slip normal faults.

5.3 BSR

Several of the seismic lines processed from the crest of the Svyatogor Ridge have shown high negative amplitude reflectors at shallow depths (Figure 29- Figure 31, Figure 35- Figure 38). These amplitudes commonly occur at approximately 150ms (TWT) below the seafloor in its southern extension. As the seafloor dips in a northward direction, the BSR occurs slightly deeper below the seafloor, at approximately 200ms (TWT) at its northern most occurrence. 150ms (TWT) corresponds to 112.5m, using an acoustic velocity of 1500 m/s. The amplitudes have reversed polarity relative to the seafloor reflection, and the top reflector crosscut strata at several events with a parallel to the seafloor, and shows pull-up effect at localized areas. This is indicative of a gas

hydrate-related BSR that marks the base of the GHSZ (C. Berndt et al., 2004; MacKay et al., 1994), and coincides with the base of the hydrate stability zone in the area (Johnson et al., 2015; Rajan et al., 2012). In areas where the BSR does not crosscut the stratigraphy, but follows it, it can be difficult to recognise. To trace the extent through these areas, enhanced reflections of the underlying free gas is used as an indicator for depth. The underlying free gas have been calculated (using a velocity of 1500m/s) to range in thickness between ~40m and 112m.

Four seismic lines (Line 10, Line 9, Line 8 and Line 5) (Figure 29- Figure 31, Figure 35- Figure 38) show a BSR with underlying free gas. Lines 8, 9 and 10 is acquired perpendicular to Line 5, which enables an interpretation of the extent of the BSR through the ridge. Line 10 is interpreted to represent the southern termination, while the northern extension is found by a termination of amplitudes in Line 5 where the seafloor dips towards the MTF. From the southern to northern termination, the BSR is found to have a 34km extension (Figure 33, Figure 32). As the seafloor dips in a northward direction, the BSR occurs slightly deeper below the seafloor, at approximately 200ms at its northern most occurrence.

Throughout the seismic lines acquired from the crest of the ridge, chimney structures and acoustic masking disrupt the BSR. The underlying free gas shows discontinuous high amplitude reflections, and the overlying sediments have lower amplitudes and seen as less defined. Low amplitudes in the overlying sediment can indicate cementation due to gas hydrates (A. Judd & Hovland, 2007). Below the zone of free gas, data shows acoustic blanking, which may be due to the high-energy absorption of gas disrupting the seismic energy (A. G. Judd & Hovland, 1992).

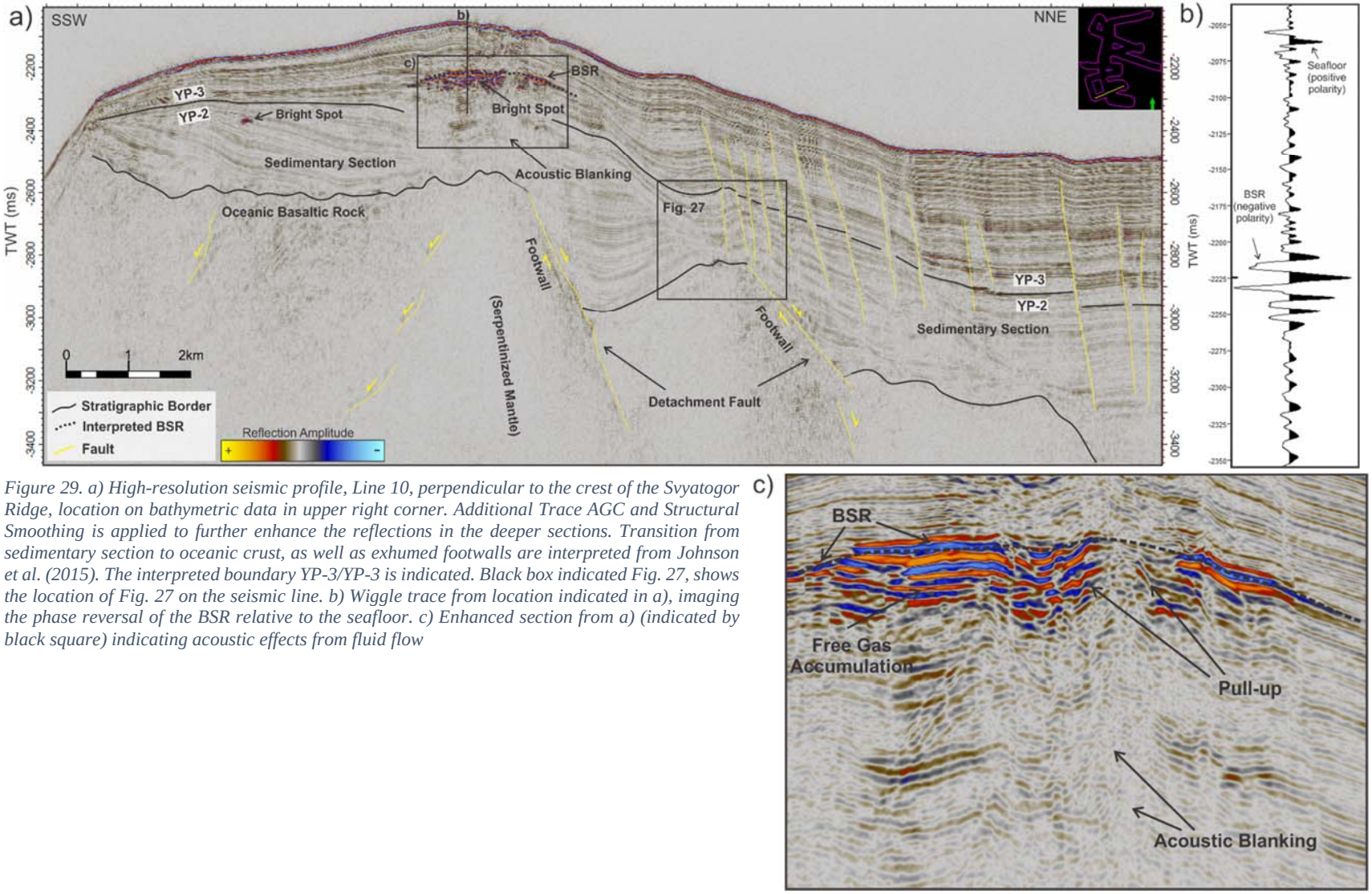

Figure 29. a) High-resolution seismic profile, Line 10, perpendicular to the crest of the Svyatogor Ridge, location on bathymetric data in upper right corner. Additional Trace AGC and Structural Smoothing is applied to further enhance the reflections in the deeper sections. Transition from sedimentary section to oceanic crust, as well as exhumed footwalls are interpreted from Johnson et al. (2015). The interpreted boundary YP-3/YP-3 is indicated. Black box indicated Fig. 27, shows the location of Fig. 27 on the seismic line. b) Wiggle trace from location indicated in a), imaging the phase reversal of the BSR relative to the seafloor. c) Enhanced section from a) (indicated by black square) indicating acoustic effects from fluid flow

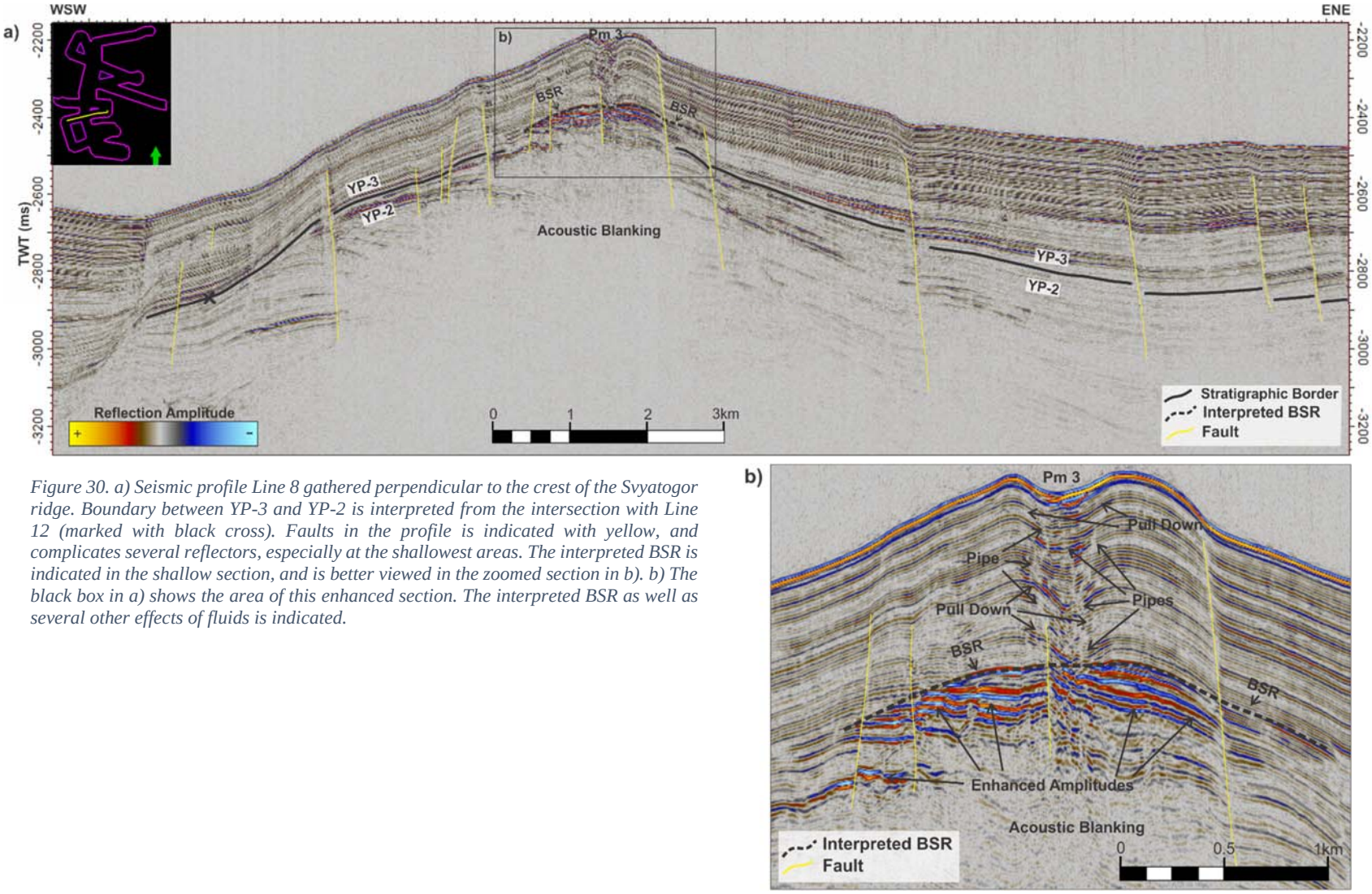

Figure 30. a) Seismic profile Line 8 gathered perpendicular to the crest of the Svyatogor ridge. Boundary between YP-3 and YP-2 is interpreted from the intersection with Line 12 (marked with black cross). Faults in the profile is indicated with yellow, and complicates several reflectors, especially at the shallowest areas. The interpreted BSR is indicated in the shallow section, and is better viewed in the zoomed section in b). b) The black box in a) shows the area of this enhanced section. The interpreted BSR as well as several other effects of fluids is indicated.

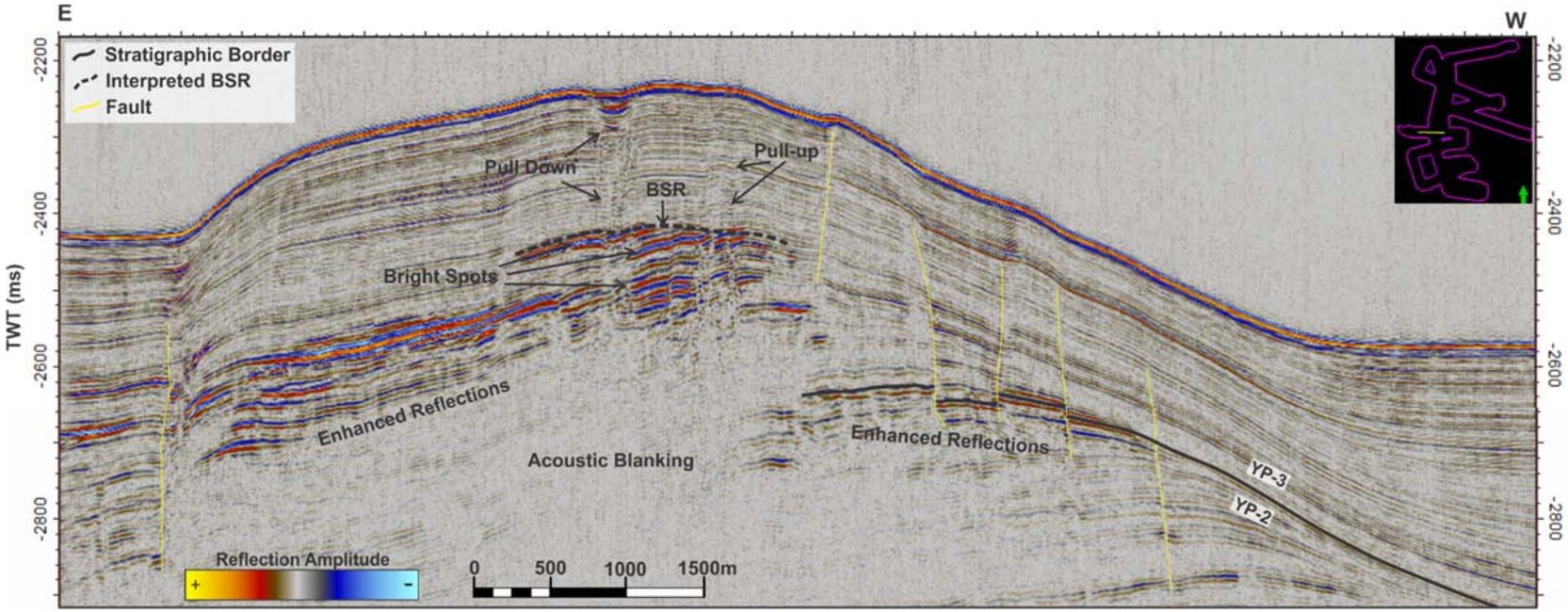

Figure 31. High-resolution seismic Line 6, imaging the continuation of the interpreted YP-3/YP-2 boundary, the interpreted BSR, faults and seismic effects of fluids. Location of profile is indicated in upper right corner.

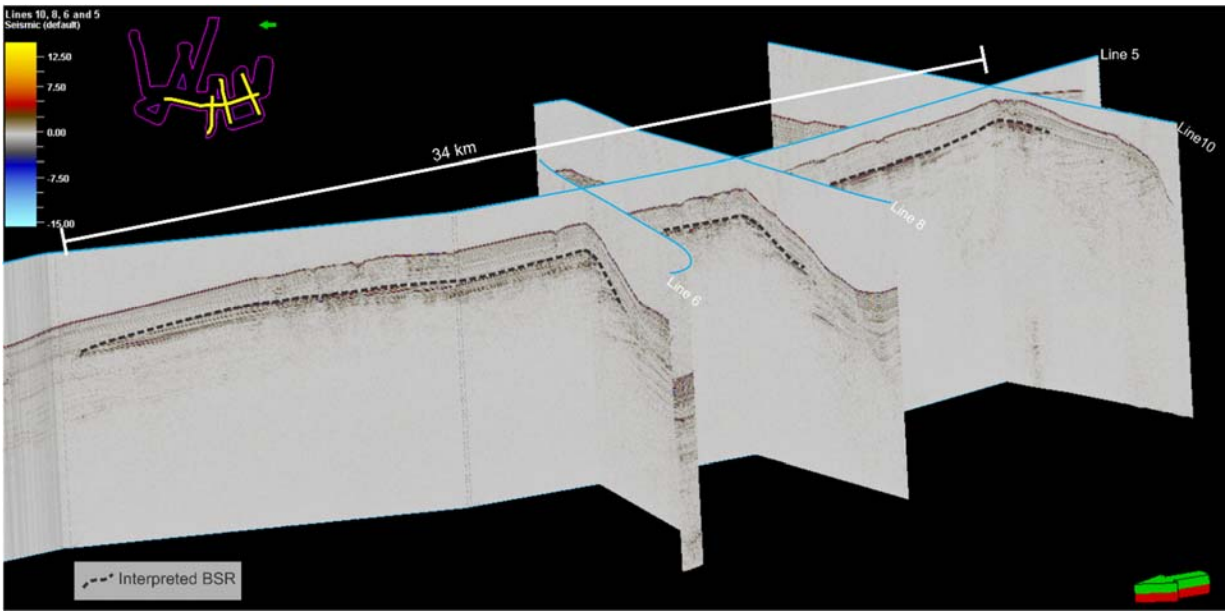

Figure 32. Seismic profiles Line 5, Line 10, Line 8 and Line 6 imaged (locations upper left) together illustrating the extent of the interpreted BSR. From the intersection between Line 10 and Line 5 to the end of the interpretation on the left side, the BSR extends 34 km. The interpreted BSR through Line 5 is traced as a continuous line for illustration purposes, although the reflections are discontinuous.

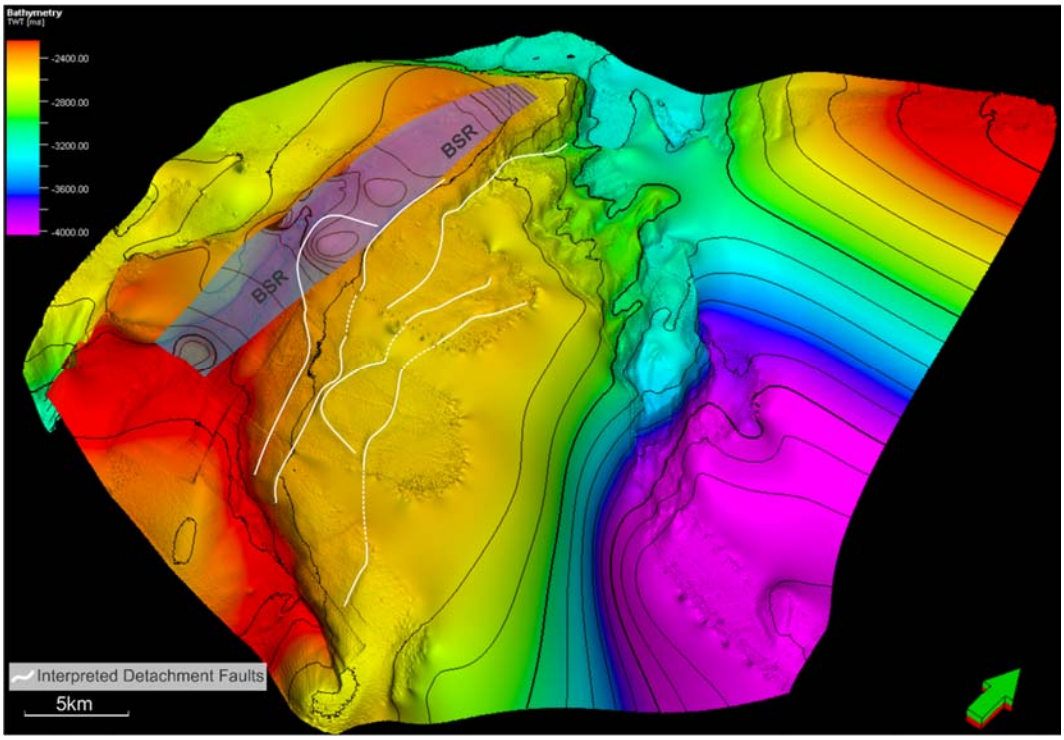

Figure 33. Bathymetry data from the Svyatogor Ridge. Distribution and extent of the interpreted BSR is indicated with a transparent blue color. Interpreted detachment faults are indicated with white lines. Dotted white lines indicate an assumed extension of detachment faults through areas not containing real bathymetry data.

5.4 Pockmarks and Associated Seismic Structures

Throughout the crest of the ridge, there are several (~20-25) circular depressions on the seafloor (Figure 34a). These depressions vary in diameter from approximately 330m to about 460m, and in depth from approximately 6m to 15m (given a P-wave velocity in water of 1480m/s). The depth of the depressions are calculated from the seismic profiles. The apparent trend of the depressions follows the ridge axis, and they occur as single features, although at one location several depressions occur as a group (Figure 34a).

The subsurface stratigraphy shows distinct troughs below depressions, often with underlying acoustic masking (Figure 34b-Figure 38). These troughs are here thought to be pull down effects resulting from a low velocity zone in the overburden, indicating a presence of gas (A. G. Judd & Hovland, 1992). The sections of disturbance in the BSR also correlates with depressions on the seafloor and pull down effects. The depressions on the seafloor are interpreted to be pockmarks (M. Hovland et al., 2002). This interpretation is much based on the presence and extent of the BSR. Based on the shape and size of the identified pockmarks, they are characterized to be normal pockmarks (M. Hovland et al., 2002). Some pockmarks are indicated in figures as Pm-1 – Pm5. This is for location reference, and Pm3 is also indicated in Figure 30.

The sedimentary stratigraphy looks to be highly affected by the presence of gas through the crest of the ridge. This is evident in the shallowest sections of Lines 10, 8 and 6 (Figure 29, Figure 30, Figure 31), and throughout Line 5 (Figure 34b-Figure 38), where the presence of gas have greatly disrupted the sedimentary stratigraphy. The pull down effects below pockmarks tend to be continuous, with no apparent masking inside the convex structures that would indicate an active migration of gas (A. G. Judd & Hovland, 1992). The pull down structures have high amplitudes, and looks to get deeper with depth.

Columnar depressions without seafloor expressions is evident at several locations through the profile, where they terminate at shallow depths. An example of this is indicated in Figure 37. These expressions in the seismic data also disrupts to some extent the BSR below. These features can indicate past gas migration, with a termination at a paleo pockmark, or a buried crater on the seafloor.

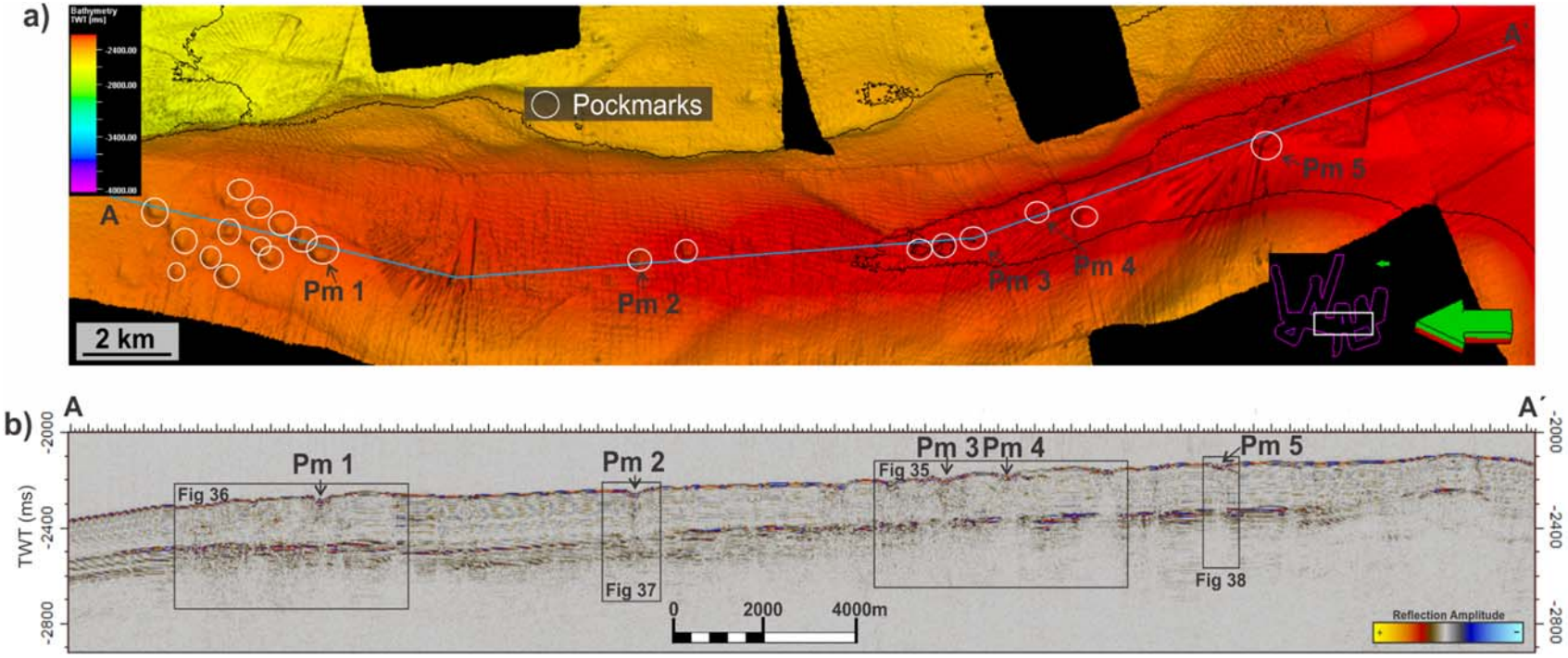

Figure 34. a) Bathymetry map of the crest of the Svyatogor Ridge, location indicated with white square bottom left, illustrating interpreted pockmarks on the seafloor with white circles. Blue line from A to A´ indicating the transect of seismic profile, Line 5, in b). b) Seismic Line 5 acquired through several of the seafloor depressions. Pm 1-5 indicating locations of some of the correlated depressions between bathymetry and seismic. This for a better overview of locations. Enhanced images of the pockmarks indicated by black squares.

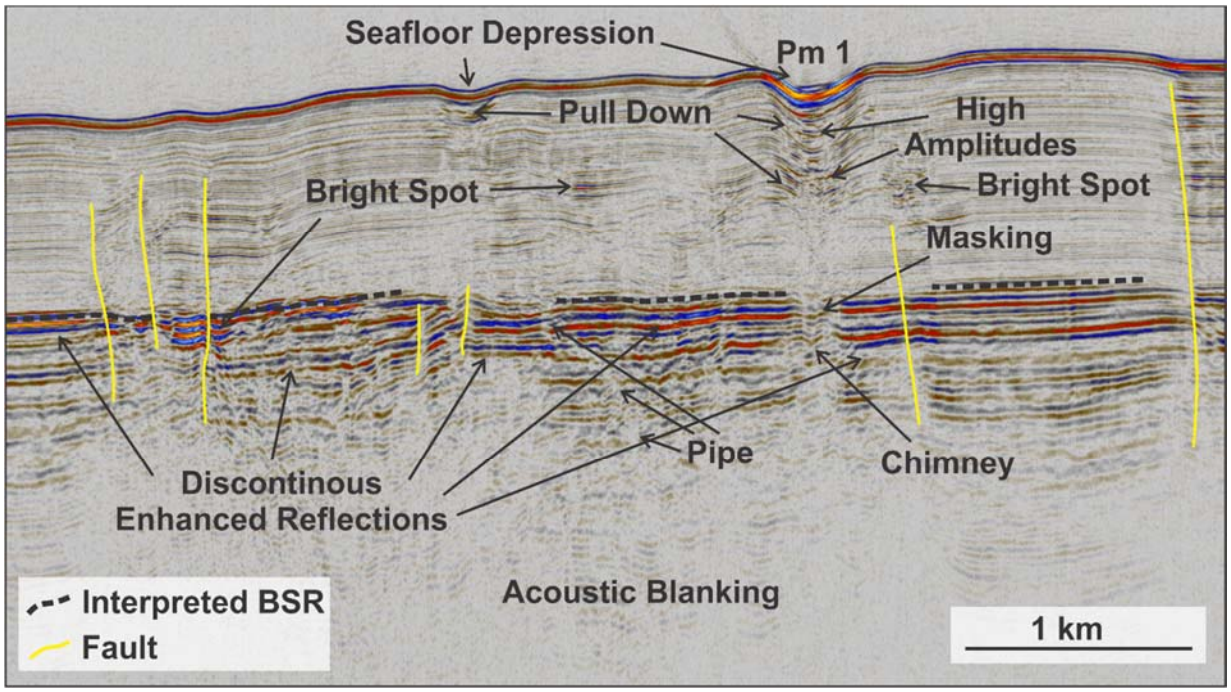

Figure 36. Enhanced seismic section from figure 34b (from Line 5). The interpreted BSR indicated by dotted black lines. Underlying this reflector is discontinuous high amplitudes, complicated by faults, and above is chaotic reflections with pull down effects, high amplitudes and acoustic masking, as well as, seafloor depressions. Pm 1 (pockmark 1) is indicated as a reference with figure 34b. Seismic legend used is the same as in Fig. 34b

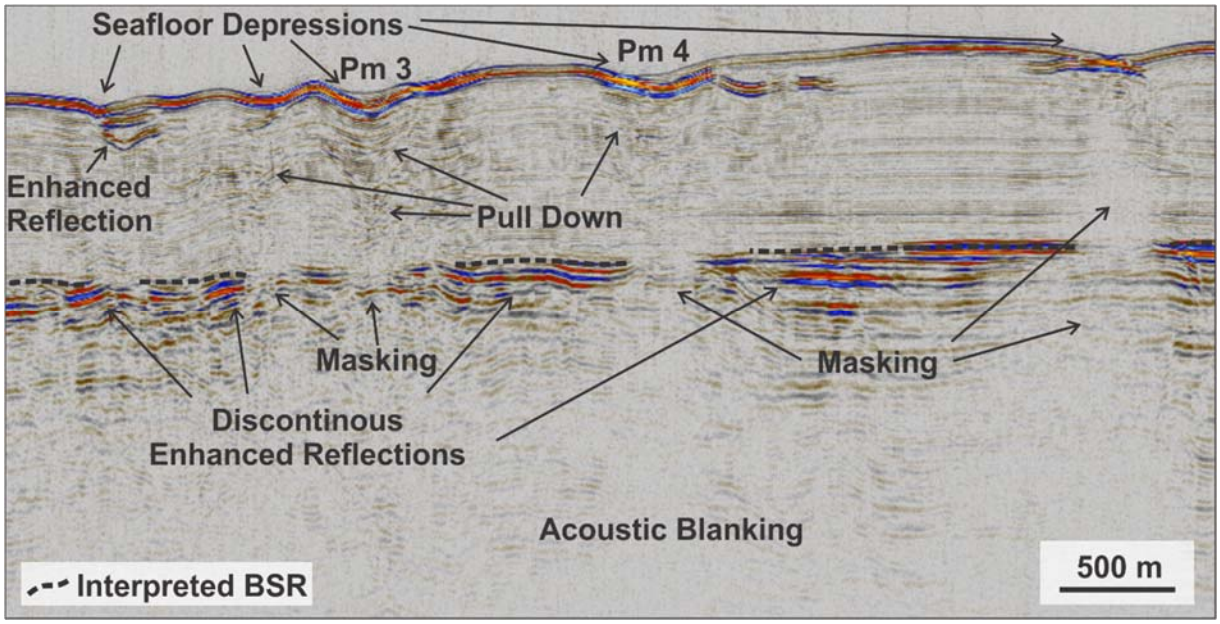

Figure 35. Enhanced seismic section from figure 34b (from Line 5). The interpreted BSR indicated. Acoustic blanking distorts the areas below the free gas, and above the BSR the reflections are complicated with pull down effects, as well as enhanced reflections beneath apparent depressions. Seismic legend used is the same as in Fig. 34b

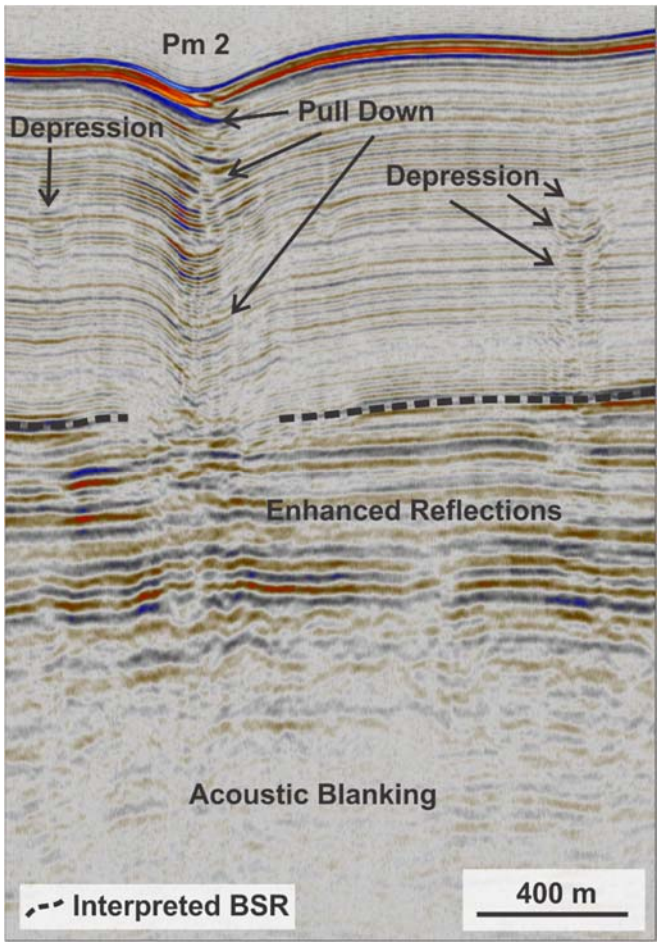

Figure 37. Enhanced section of the seismic below Pm 2 in seismic Line 5 (location in figure.34b). The pull down effects below this pockmark have high amplitudes, and shows great similarities with both Pm 3 and Pm 4. Two depressions below the seafloor is indicated. Seismic legend used is the same as in Fig. 34b

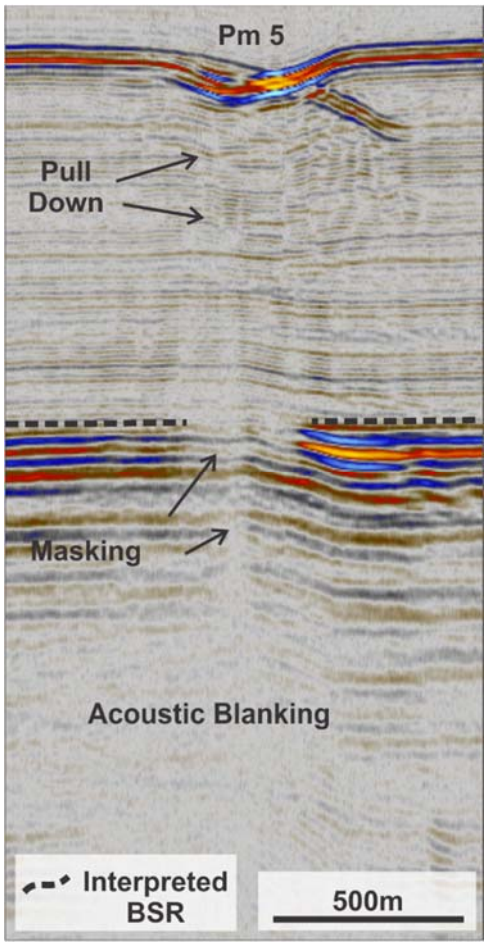

Figure 38. Enhanced section of the seismic below Pm 5 in seismic Line 5 (location in Fig.34b). The seafloor expression of Pm 5 shows a complicated structure. The section below shows small pull down effects and acoustic masking through the BSR.

6 Discussion

The results provided in the previous chapter focus mainly on the seismic profiles gathered from the ridge crest, as well as a stratigraphic interpretation using Line 12 further towards the Molloy Transform. These lines, and the areas they represent, are chosen because of their content of important stratigraphic information and indications of fluid structures. The processed lines cover a larger area than what is interpreted, and so, all finished processed lines can be viewed in Appendix.

6.1 Stratigraphic and Tectonic Setting of the Svyatogor Ridge

From the junction between Line 12 and the correlated stratigraphic boundaries provided by Jochen Knies and Rune Mattingsdal, the YP-2/YP-3 seismic reflectors are traced into the crest of the Svyatogor Ridge.

Stratigraphic unit YP-1 was not traced through seismic data due to its low intersection with Line 12. As this unit is not traced to the ridge, there is an uncertainty of whether or not this unit is present at the ridge. From the reconstruction by Johnson et al. (2015) (Figure 11), the YP-1 sequence might be too old to be present at the Svyatogor Ridge. Table 1 shows that the corresponding age for stratigraphic unit YP-1 is 2.7 - ~11Ma. The reconstruction by Johnson et al. (2015) shows that the deposition of YP-1 was probably prior to the formation of the Svyatogor Ridge.

The presence of the stratigraphic units YP-3 and YP-2 indicates that the age of the sediments on the Svyatogor Ridge correlates with the ages of sediments on the Yermak Plateau and the Vestnesa sediment drift. Hence, YP-3 is of Pleistocene origin (present-1.5 Ma) and YP-2 of Pleistocene-Pliocene origin (~2.7-1.5 Ma) (Knies et al., 2009; Mattingsdal et al., 2014). Figure 39 illustrates the distribution of the sedimentary sequences, and how these are affected by faults on the ridge of the Svyatogor Ridge. This figure shows that the sedimentary packages are thinner on the western flank than on the eastern flank of the ridge. This trend follows through the ridge, but with variations in depositional thickness on both flanks. The distribution of faults is also greater on the eastern flank than that of the western flank.

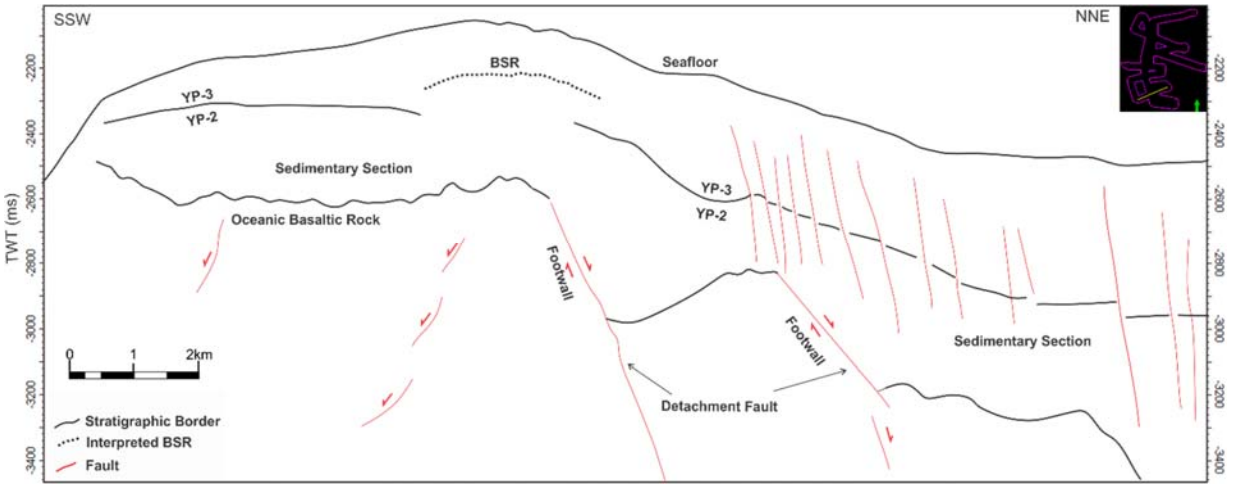

Figure 39. Illustration of the stratigraphic setting of the Svyatogor Ridge showing the traced YP-3/YP-2 sedimentary boundary, interpreted BSR, and faults. Interpreted detachment faults are indicated, other faults are interpreted as predominantly dip-slip faults. This illustration is based on seismic Line 10, and location is indicated in upper right corner.

At about 2.7Ma the West Spitsbergen Current (WSC) experienced a high sediment load as a result of an ice-sheet expansion in the Northern Hemisphere (Gebhardt, Geissler, Matthiessen, & Jokat, 2014). Indicated from the Paleo-position of the WSC at 3-2Ma (Figure 11), much of the sedimentary succession comprising the Svyatogor Ridge may be a result of this increased sediment rate. The WSC underwent an eastward migration over time to its current position on the West Svalbard Continental Slope (Figure 11). 2Ma this current had a direction northwards towards the axis of the Vestnesa Ridge (before the breakup with the Svyatogor Ridge) (Johnson et al., 2015). The westward movement of the Svyatogor Ridge, and the eastward movement of the WSC, will have had an effect on sedimentary supply where the supply decreases significantly with longer offset between the two. From early stages of this offsetting, a higher sedimentation rate on the eastern side of the Svyatogor is likely. At present time, the Svyatogor Ridge may be cut off from sedimentary supply from this current, implying sedimentation rates today to be very low, or even that the Svyatogor Ridge is in a state of non-deposition.

The large amount of normal faults on the eastern side of the Svyatogor Ridge may have had a significant effect on the sedimentary strata. A higher tectonic activity in the form of detachment faults (Figure 29, Figure 33, Figure 39) on the eastern side of the Svyatogor Ridge may be a direct result of the spreading of the Knipovich Ridge. Due to the eastern down-throw of the detachment

faults, normal dip-slip faults can have occurred in the sedimentary strata to accommodate for extra space.

The leftmost detachment fault in seismic Line 10 (Figure 29) indicates that the lowermost sedimentary unit (YP-2) is syn-depositional. The rotation of the YP-2 block immediately left of the fault is rotated downwards whereas on the left side it is marginally rotated upwards. This can indicate that this fault have been recently active, until ~1.5Ma.

The Svyatogor Ridge have been hypothesized to have once been a part of the Vestnesa Ridge (Johnson et al., 2015). Although these sediment drifts once were one drift, the Svyatogor sediment drift now have a very different tectonic regime to that of Vestnesa. Vestnesa lies on a passive margin, and Svyatogor lies on an active margin. Indications of an active margin is seen from the age indicated by the detachment faults, as well as faults reaching close to the surface with an overlying rolling topography. Both the MTF and Knipovich Ridge are active, and the Knipovich Ridge is spreading asymmetrically with the fastest spreading occurring to the west at 7.0 mm/yr, compared with 1 mm/yr on the eastern side (Crane et al., 1991). The interplay between these tectonic regimes have had a great influence on the sedimentation on the Svyatogor Ridge. On the eastern wall of the ridge there is active redistribution of sediments to fill accommodation space created at times of spreading, and on the western side there is much less indications of tectonic activity. The propagation of the MTF into its current position may have cut off the Svyatogor Ridge from a sediment source (the WSC). The Vestnesa Ridge lies closer both to the WSC and the Svalbard continental margin (Figure 11), and will therefore have a higher depositional rate.

6.2 Subsurface Fluid Flow and Seafloor Expressions

Throughout the Svyatogor Ridge, there is a variety of seismic expressions indicating subsurface fluid migration and the presence of fluids. These expressions was found to include BSR, acoustic masking that disrupts the continuity of the BSR (especially evident in Line 5), areas of enhanced reflections, acoustic blanking below enhanced reflections, pull-down effects, bright spots, and acoustic pipes (Figure 29-Figure 31, Figure 35- Figure 38). The sedimentary sections of the ridge is interpreted to be highly affected by the presence of fluids, and the above mentioned indicators

of this occur as both single and interconnected features. Interconnected features can be difficult to distinguish from each other, and therefore identify.

Bathymetric data shows depressions on the seafloor throughout the crest of the ridge (Figure 34), interpreted to be normal pockmarks (M. Hovland et al., 2002) (Figure 4). The pockmarks are interpreted to be a product of gas migration (Løseth et al., 2009). These pockmarks are found to be limited to the crest of the ridge, as is the BSR.

The pull down effects found below pockmarks are, as stated, continuous and very prominent, and interpreted to be a result of low velocity due to gas. As illustrated in Figure 40, these pull downs get deeper with depth. This figure also illustrates the interpretation of the presence of gas hydrates. As stated in section 1.5.2, gas hydrates will commonly result in a pull-up structure (Lee et al., 2005). Another interpretation of these features is that they are a stack of paleo pockmarks. From this interpretation, the deepening of the troughs can be a result of a higher flux of fluids through the oldest pockmarks where the depth is greatest.

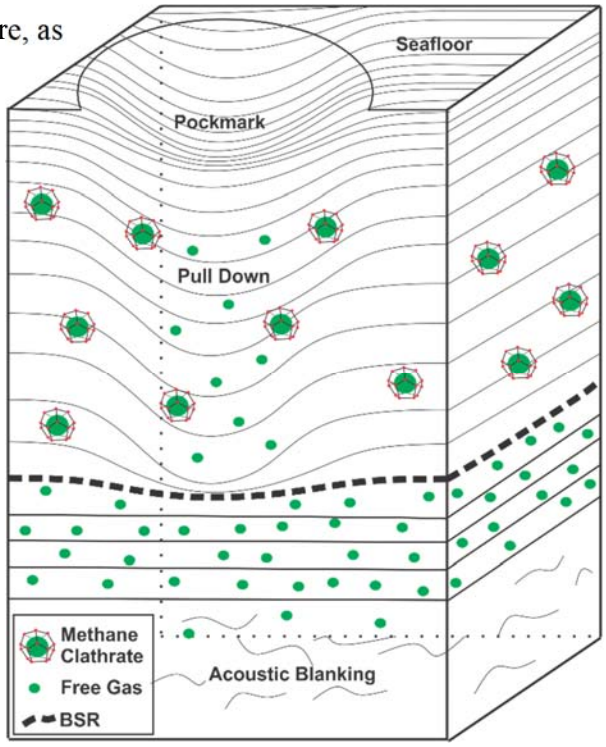

Figure 40. Illustration of the convex structures found below several of the interpreted pockmarks of the Svyatogor Ridge. BSR with underlying free gas, and overlying gas hydrates are indicated. Free gas is also illustrated to be present and trapped within the GHSZ.

Through the BSR and the zone of free gas, vertical zones of acoustic masking is found. This is especially prominent in Figure 35. This can indicate that some gas is migrating through the BSR and into the GHSZ. Gas hydrates forming in sediments greatly decrease permeability as the porosity of the sediments is reduced by hydrate clogging (Nimblett & Ruppel, 2003). This means that free gas migrating into the GHSZ can then be trapped, and hindered from further migration.

Seismic Line 8 shows pipe structures that looks to reach the surface through a pockmark (Pm3, Figure 30), indicating active vertical migration. Line 2, located in the northern extent of the Svyatogor Ridge shows indication of possible migration through faults. This is indicated by bright spots adjacent faults in Figure 28. As stated in section 1.3.1 fluids will migrate towards a lower hydraulic potential (Bjørlykke, 1993), but other than bright spots adjacent faults in seismic Line 2, and a pipe structure in Line 8, there is little evidence of active lateral or vertical migration of fluids. Fluid migration is therefore found to be dominantly vertical migration from the crest of the ridge, into the GHSZ.

Pockmarks are here the only visible features on the surface that are a direct result of gas migrating to the surface. A. Judd and Hovland (2007) gives a characterization of what indicates a low- to high hydrocarbon flux. In this characterization, areas with low hydrocarbon flux are found to often have a well-developed BSR, but few topographic features. Svyatogor Ridge will, according to the findings by A. Judd and Hovland (2007), be characterized by a low hydrocarbon flux. A low hydrocarbon flux can support the lack of active migration found throughout the ridge.

Figure 40 indicates how free gas is proposed to be trapped within stacked paleo pockmark structures in the GHSZ. Stacking of paleo pockmarks indicates that there have been a continuous flux of fluids. The few indications of acoustic masking/chimneys reaching the surface can suggest that the area has little or no active fluid migration systems. This leads to an interpretation of a former active system that is now inactive or have a very low fluid flux. This is a contrast to an highly active gas migration found on the Vestnesa Ridge. Here, Bünz, Polyanov, Vadakkepuliyambatta, Consolaro, and Mienert (2012) reported findings of gas flares reaching a height of 800m above seafloor pockmarks.

The seismic high-resolution 2D profiles cover a large part of the Svyatogor Ridge and surrounding areas, providing a good representation of local fluid systems. But as the seismic data only images a 2D cross-section of a discrete fluid flow system, it is possible that there are discrepancies between interpretations and the real nature of the system (Løseth et al., 2009).

6.3 Origin of Gas

The previous sections have showed that there is some amount of gas, in the form of free gas and hydrates, throughout the subsurface of the Svyatogor Ridge. A conclusive proof of origin of this gas is not possible without geochemical data, although the 2D seismic data can provide some insight on formational possibilities.

Vanneste, Guidard, and Mienert (2005) found that from the Vestnesa Ridge towards the MTF, the geothermal gradient gradually increases from 70°C to 115°C km^{-1}. Considering the size of the Svyatogor Ridge relative to the Vestnesa Ridge, and its close vicinity to the MTF, a constant geothermal gradient of 115°C km^{-1} can represent the Svyatogor Ridge well. The optimum temperature range for hydrocarbons of methanogenetic origin is 35°C to 45°C, and from about 50°C for thermogenetic hydrocarbons (Vially, 1992).

The sediments on the Svyatogor Ridge ranges in depth from ~375m on the ridge crest to ~750m on its walls down to overlying oceanic crust. At a depth of 375m, temperatures reaches ~43°C, with a geothermal gradient of 115°C, and a depth of 750m reaches a temperature of ~86°C. From these calculations the sediments on the crest of the ridge is within the window of hydrocarbons of methanogenetic origin, and the walls of the ridge fall into the window of thermogenetic origin, illustrated in Figure 41. This indicates that there is a possibility that the gas on the Svyatogor Ridge are of biotic origin.

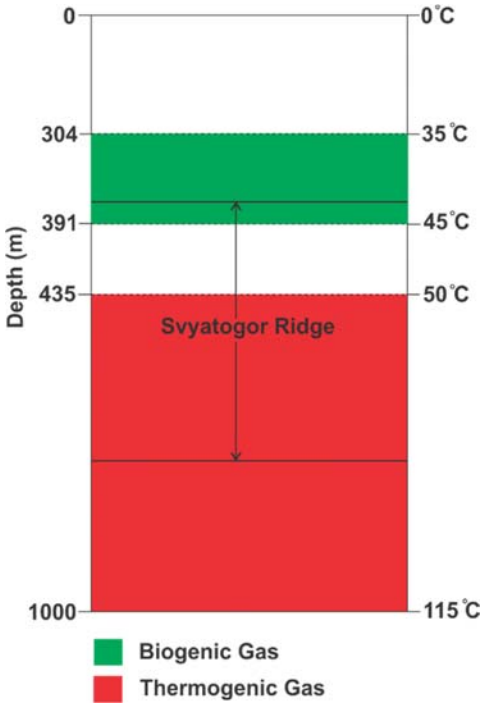

Figure 41. Depth and temperature plot illustrating the biotic gas potential on the Svyatogor Ridge, using a constant geothermal gradient of 115°C

Hydrocarbons found on the Vestnesa Ridge are found to be derived from thermogenic sources (Smith, Mienert, Bünz, & Greinert, 2014). Knies and Mann (2002) used organic-geochemical and microscopic analyses on sediments of Miocene age from ODP Hole 909 in the Fram Strait. From these analyses, they found source rocks providing biotic gas.

Miocene sediments correlates to stratigraphic unit YP-1, which is present on the Vestnesa Ridge (Smith et al., 2014), but are not found on the Svyatogor Ridge and considered here to be too old to be present. The lack of YP-1 differentiate the Svyatogor Ridge from the Vestnesa Ridge in terms maturity of sediments, and shows that the origin of gas is not necessarily the same on the two ridges.

Oceanic crust underlying the Svyatogor Ridge is possibly serpentinized (Kandilarov et al., 2010). Serpentinization of ultramaphic rock have the ability to form abiotic gas (Etiope & Sherwood Lollar, 2013). Detachment faults found throughout the ridge exposes sediments (Figure 29, Figure 39), providing a deeper mixing of water (see section 1.4.2), and a possible fluid pathway. The most prominent indications of active and inactive migrations of gas have been found to occur directly from the underlying crust.

This indicates that there are found possibilities of both biotic and abiotic hydrocarbon production on the Svyatogor Ridge. Although there is not found evidence of active migration of gas from the walls of the ridge, one cannot rule out the possibility of migration of gas from source rocks of higher hydrocarbon potential. One type of origin does not rule out the other, and the presence of both abiotic and biotic gas is here considered to be a likely scenario. Figure 42 illustrates the how an abiotic gas system is proposed to provide gas from ultramaphic rock to the overlying sedimentary rock on the Svyatogor Ridge.

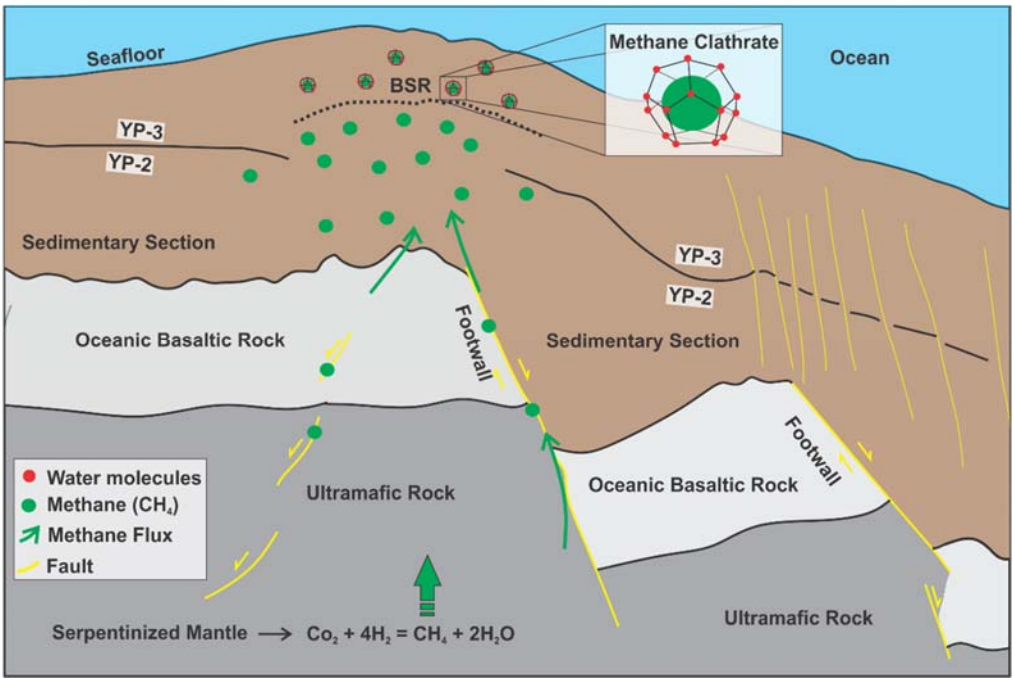

Figure 42. Illustration showing how the interpreted abiotic fluid system of the Svyatogor Ridge is interpreted to operate, where green arrows and dots illustrates the origin (deriving from the chemical equation), migration and trapping of methane under gas hydrates.

7 Conclusion

High-resolution 2D seismic data have been processed and interpreted, together with multibeam bathymetry data and a correlation with ODP borehole 909. From these interpretations, two sedimentary sequences, YP-3 and YP-2, have been identified and traced through the crest of the Svyatogor Ridge, providing age determination of the sediments. Sediments on the ridge are found to be from the Pleistocene-Pliocene. Accumulations of gas have been identified within these sedimentary sequences in the form of free gas and gas hydrates. Seismic indications leading to the interpretation of the presence of hydrocarbons is comprised of bright spots, enhanced reflections, acoustic blanking and a prominent BSR, found to extend 34km through the Svyatogor Ridge. Multibeam bathymetry data shows circular depressions interpreted to be normal pockmarks with an inactive or low fluid flux.

The Svyatogor Ridge is found to be highly affected by tectonic activity. This activity is found to influence the stratigraphic setting, where there eastern wall is more sedimented than the western. This is found to be due to both the eastward migration of the WSC, and the ultraslow spreading of the Knipovich Ridge, where sediments accommodates free space created by extensional faulting.

Sediments on both the crest of the ridge, and its walls have been calculated to be in the window of biotic hydrocarbon production. Although, geochemical data from adjacent areas have found the sediments of Miocene age have highest hydrocarbon prospects, sediments much older than what is present here. Large detachment faults are found to expose ultramaphic rock, and directly underlies high amplitude reflections. This young oceanic crust, have from other studies found to be possibly serpentinized, which leads to a possibility of the presence of abiotic gas. Considered here is the possibility a presence of both abiotic and biotic gas.

References Cited

Al-Shuhail, W. A. M. A. A. (2011). *Processing of Seismic Reflection Data Using MATLAB*: Morgan & Claypool Publishers series.

Amundsen, I. M. H., Blinova, M., Hjelstuen, B. O., Mjelde, R., & Haflidason, H. (2011). The Cenozoic western Svalbard margin: sediment geometry and sedimentary processes in an area of ultraslow oceanic spreading. *Marine Geophysical Research, 32*(4), 441-453. doi: 10.1007/s11001-011-9127-z

Andreassen, K. (2009). Marine Geophysics, Lecture notes for Geo-3123. In U. o. Tromsø (Ed.).

Andreassen, K., Nilssen, E., & Ødegaard, C. (2007). Analysis of shallow gas and fluid migration within the Plio-Pleistocene sedimentary succession of the SW Barents Sea continental margin using 3D seismic data. *Geo-Marine Letters, 27*(2-4), 155-171. doi: 10.1007/s00367-007-0071-5

Berndt, C. (2005). *Focused fluid flow in passive continental margins* (Vol. 363).

Berndt, C., Bünz, S., Clayton, T., Mienert, J., & Saunders, M. (2004). Seismic character of bottom simulating reflectors: examples from the mid-Norwegian margin. *Marine and Petroleum Geology, 21*(6), 723-733. doi: http://dx.doi.org/10.1016/j.marpetgeo.2004.02.003

Berndt, M. E., Allen, D. E., & Seyfried, W. E. (1996). Reduction of CO2 during serpentinization of olivine at 300 °C and 500 bar. *Geology, 24*(4), 351-354. doi: 10.1130/0091-7613(1996)024<0351:rocdso>2.3.co;2

Berner, R. A. (1980). *Early Diagenesis: A Theoretical Approach*: Princeton University Press.

Bjørlykke, K. (1993). Fluid flow in sedimentary basins. *Sedimentary Geology, 86*(1–2), 137-158. doi: http://dx.doi.org/10.1016/0037-0738(93)90137-T

Brown, G., Hawkesworth, C., & Wilson, C. (1992). *Understanding the Earth, a new synthesis*. Great Britain: Cambridge University Press.

Bünz, S., Polyanov, S., Vadakkepuliyambatta, S., Consolaro, C., & Mienert, J. (2012). Active gas venting through hydrate-bearing sediments on the Vestnesa Ridge, offshore W-Svalbard. *Marine Geology, 332–334*(0), 189-197. doi: http://dx.doi.org/10.1016/j.margeo.2012.09.012

Cannat, M., Fontaine, F., & Escartín, J. (2013). Serpentinization and Associated Hydrogen And Methane Fluxes at Slow Spreading Ridges *Diversity Of Hydrothermal Systems On Slow Spreading Ocean Ridges* (pp. 241-264): American Geophysical Union.

Chamov, N. P., Sokolov, S. Y., Kostyleva, V. V., Efimov, V. N., Peive, A. A., Aleksandrova, G. N., . . . Stupin, S. I. (2010). Structure and composition of the sedimentary cover in the Knipovich Rift valley and Molloy Deep (Norwegian-Greenland basin). *Lithology and Mineral Resources, 45*(6), 532-554. doi: 10.1134/S0024490210060039

Chand, S., & Minshull, T. A. (2003). Seismic constraints on the effects of gas hydrate on sediment physical properties and fluid flow: a review. *Geofluids, 3*(4), 275-289. doi: 10.1046/j.1468-8123.2003.00067.x

Crane, K., Doss, H., Vogt, P., Sundvor, E., Cherkashov, G., Poroshina, I., & Joseph, D. (2001). The role of the Spitsbergen shear zone in determining morphology, segmentation and

evolution of the Knipovich Ridge. *Marine Geophysical Researches, 22*(3), 153-205. doi: 10.1023/A:1012288309435

Crane, K., Sundvor, E., Buck, R., & Martinez, F. (1991). Rifting in the northern Norwegian-Greenland Sea: Thermal tests of asymmetric spreading. *Journal of Geophysical Research: Solid Earth, 96*(B9), 14529-14550. doi: 10.1029/91JB01231

Dickens, G. R. (2011). Down the Rabbit Hole: toward appropriate discussion of methane release from gas hydrate systems during the Paleocene-Eocene thermal maximum and other past hyperthermal events. *Clim. Past, 7*(3), 831-846. doi: 10.5194/cp-7-831-2011

Eiken, O., & Hinz, K. (1993). Contourites in the Fram Strait. *Sedimentary Geology, 82*(1–4), 15-32. doi: http://dx.doi.org/10.1016/0037-0738(93)90110-Q

Eldholm, O., Sundvor, E., & Wissmann, G. (1980). *The Continental Margins of the Norwegian--Greenland Sea: Recent Results and Outstanding Problems [and Discussion]* (Vol. 294).

Etiope, G., & Schoell, M. (2014). Abiotic Gas: Atypical, But Not Rare. *Elements, 10*(4), 291-296. doi: 10.2113/gselements.10.4.291

Etiope, G., & Sherwood Lollar, B. (2013). Abiotic Methane On Earth. *Reviews of Geophysics, 51*(2), 276-299. doi: 10.1002/rog.20011

Everett, M. E. (2013). *Near-Surface Applied Geophysics*: Cambridge University Press.

Fossen, H. (2010). *Structural Geology*. U.S.A: Cambridge University Press.

Gebhardt, A. C., Geissler, W. H., Matthiessen, J., & Jokat, W. (2014). Changes in current patterns in the Fram Strait at the Pliocene/Pleistocene boundary. *Quaternary Science Reviews, 92*(0), 179-189. doi: http://dx.doi.org/10.1016/j.quascirev.2013.07.015

Geissler, W. H., & Jokat, W. (2004). A geophysical study of the northern Svalbard continental margin. *Geophysical Journal International, 158*(1), 50-66. doi: 10.1111/j.1365-246X.2004.02315.x

Haacke, R. R., Westbrook, G. K., & Hyndman, R. D. (2007). Gas hydrate, fluid flow and free gas: Formation of the bottom-simulating reflector. *Earth and Planetary Science Letters, 261*(3–4), 407-420. doi: http://dx.doi.org/10.1016/j.epsl.2007.07.008

Holbrook, W. S., Lizarralde, D., Pecher, I. A., Gorman, A. R., Hackwith, K. L., Hornbach, M., & Saffer, D. (2002). Escape of methane gas through sediment waves in a large methane hydrate province. *Geology, 30*(5), 467-470. doi: 10.1130/0091-7613(2002)030<0467:eomgts>2.0.co;2

Hovland, M. (2005). Gas hydrates. *Petroleum Geology*, 261-268.

Hovland, M., Gardner, J. V., & Judd, A. G. (2002). The significance of pockmarks to understanding fluid flow processes and geohazards. *Geofluids, 2*(2), 127-136. doi: 10.1046/j.1468-8123.2002.00028.x

Hovland, M., & Judd, A. G. (1988). *Seabed Pockmarks and Seepages: Impact on Geology, Biology and the Marine Environment*. London: Graham and Trotman.

Johnson, J. E., Mienert, J., Plaza-Faverola, A., Vadakkepuliyambatta, S., Knies, J., Bünz, S., . . . Ferré, B. (2015). Abiotic methane from ultraslow-spreading ridges can charge Arctic gas hydrates. *Geology, 43*(5), 371-374. doi: 10.1130/g36440.1

Judd, A., & Hovland, M. (2007). *Seabed Fluid Flow, The Impact on Geology, Biology and the Marine Environment*. USA: Cambridge University Press.

Judd, A. G., & Hovland, M. (1992). The evidence of shallow gas in marine sediments. *Continental Shelf Research, 12*(10), 1081-1095. doi: http://dx.doi.org/10.1016/0278-4343(92)90070-Z

Kandilarov, A., Landa, H., Mjelde, R., Pedersen, R., Okino, K., & Murai, Y. (2010). Crustal structure of the ultra-slow spreading Knipovich Ridge, North Atlantic, along a presumed ridge segment center. *Marine Geophysical Researches, 31*(3), 173-195. doi: 10.1007/s11001-010-9095-8

Kandilarov, A., Mjelde, R., Okino, K., & Murai, Y. (2008). Crustal structure of the ultra-slow spreading Knipovich Ridge, North Atlantic, along a presumed amagmatic portion of oceanic crustal formation. *Marine Geophysical Researches, 29*(2), 109-134. doi: 10.1007/s11001-008-9050-0

Kastner, M., Keene, J. B., & Gieskes, J. M. (1977). Diagenesis of siliceous oozes - 1. Chemical controls on the rate of opal-A to opal-CT transformation - and experimental study. *Geocheimica et Cosmochimica Acta, 41*, 1041-1059.

King, L. H., & MacLean, B. (1970). Pockmarks on the Scotian Shelf. *Geological Society of America Bulletin, 81*(10), 3141-3148. doi: 10.1130/0016-7606(1970)81[3141:potss]2.0.co;2

Knies, J., & Mann, U. (2002). Depositional environment and source rock potential of Miocene strata from the central Fram Strait: introduction of a new computing tool for simulating organic facies variations. *Marine and Petroleum Geology, 19*(7), 811-828. doi: http://dx.doi.org/10.1016/S0264-8172(02)00090-9

Knies, J., Matthiessen, J., Vogt, C., Laberg, J. S., Hjelstuen, B. O., Smelror, M., . . . Vorren, T. O. (2009). The Plio-Pleistocene glaciation of the Barents Sea–Svalbard region: a new model based on revised chronostratigraphy. *Quaternary Science Reviews, 28*(9–10), 812-829. doi: http://dx.doi.org/10.1016/j.quascirev.2008.12.002

Krooss, B. M., & Leythaeuser, D. (1996). Molecular Diffusion of Light Hydrocarbons in Sedimentary Rocks and its Role in Migration and Dissipation of Natural Gas. *Hydrocarbon Migration And Its Near-Surface Expression*(AAPG Memoir 66), 173-183.

Lee, J. H., Baek, Y. S., Ryu, B. J., Riedel, M., & Hyndman, R. D. (2005). A seismic survey to detect natural gas hydrate in the East Sea of Korea. *Marine Geophysical Researches, 26*(1), 51-59. doi: 10.1007/s11001-005-6975-4

Lien, J. R., & Løvhøiden, G. (2010). *Generell Fysikk for Universiteter og Høgskoler, Bind 1 Mekanikk*. Oslo: Universitetsforlaget.

Ligtenberg, J. H. (2005). Detection of fluid migration pathways in seismic data: implications for fault seal analysis. *Basin Research, 17*(1), 141-153. doi: 10.1111/j.1365-2117.2005.00258.x

Lister, G. S., & Davis, G. A. (1989). The origin of metamorphic core complexes and detachment faults formed during Tertiary Continental extension in the northern Colorado River region, U.S.A. *Journal of Structural Geology, 11*, 65-94.

Liu, X., & Flemings, P. B. (2007). Dynamic multiphase flow model of hydrate formation in marine sediments. *Journal of Geophysical Research: Solid Earth, 112*(B3), n/a-n/a. doi: 10.1029/2005JB004227

Ljones, F., Kuwano, A., Mjelde, R., Breivik, A., Shimamura, H., Murai, Y., & Nishimura, Y. (2004). Crustal transect from the North Atlantic Knipovich Ridge to the Svalbard Margin

west of Hornsund. *Tectonophysics, 378*(1–2), 17-41. doi: http://dx.doi.org/10.1016/j.tecto.2003.10.003

Løseth, H., Gading, M., & Wensaas, L. (2009). Hydrocarbon leakage interpreted on seismic data. *Marine and Petroleum Geology, 26*(7), 1304-1319. doi: http://dx.doi.org/10.1016/j.marpetgeo.2008.09.008

MacKay, M. E., Jarrard, R. D., Westbrook, G. K., & Hyndman, R. D. (1994). Origin of bottom-simulating reflectors: Geophysical evidence from the Cascadia accretionary prism. *Geology, 22*(5), 459-462. doi: 10.1130/0091-7613(1994)022<0459:oobsrg>2.3.co;2

Maslin, M., Owen, M., Betts, R., Day, S., Dunkley Jones, T., & Ridgwell, A. (2010). *Gas hydrates: past and future geohazard?* (Vol. 368).

Mattingsdal, R., Knies, J., Andreassen, K., Fabian, K., Husum, K., Grøsfjeld, K., & De Schepper, S. (2014). A new 6 Myr stratigraphic framework for the Atlantic–Arctic Gateway. *Quaternary Science Reviews, 92*(0), 170-178. doi: http://dx.doi.org/10.1016/j.quascirev.2013.08.022

Milliken, K. (2003). Diagenesis *Sedimentology* (pp. 339-349): Springer Netherlands.

Moore, W. S., & Wilson, A. M. (2005). Advective flow through the upper continental shelf driven by storms, buoyancy, and submarine groundwater discharge. *Earth and Planetary Science Letters, 235*(3–4), 564-576. doi: http://dx.doi.org/10.1016/j.epsl.2005.04.043

Myhre, A. M., Thiede, J., & Firth, J. V. (1995). Chapter 7. SITE 909. *Proceedings of the Ocean Drilling Program, Initial Reports, 151*.

Müntener, O. (2010). Serpentine and serpentinization: A link between planet formation and life. *Geology, 38*(10), 959-960. doi: 10.1130/focus102010.1

Nealon, J. W. (2006). *Dynamics of methane migration in marine hydrate systems: Examples from the Guaymas Transform, Blake Ridge, and Storegga landslide.* (3225307 Ph.D.), University of Wyoming, Ann Arbor. Retrieved from http://search.proquest.com/docview/304975064?accountid=17260 ProQuest Dissertations & Theses Global database.

Nimblett, J., & Ruppel, C. (2003). Permeability evolution during the formation of gas hydrates in marine sediments. *Journal of Geophysical Research: Solid Earth, 108*(B9), n/a-n/a. doi: 10.1029/2001JB001650

Peive, A. A., & Chamov, N. P. (2008). Basic tectonic features of the Knipovich Ridge (North Atlantic) and its neotectonic evolution. *Geotectonics, 42*(1), 31-47. doi: 10.1134/S0016852108010044

Rafaelsen, B. (2005). Seismic resolution and frequency filtering. *Mat, Svalex*.

Rajan, A., Mienert, J., Bünz, S., & Chand, S. (2012). Potential serpentinization, degassing, and gas hydrate formation at a young (<20 Ma) sedimented ocean crust of the Arctic Ocean ridge system. *Journal of Geophysical Research: Solid Earth, 117*(B3), n/a-n/a. doi: 10.1029/2011JB008537

Riedel, M., Spence, G. D., Chapman, N. R., & Hyndman, R. D. (2002). Seismic investigations of a vent field associated with gas hydrates, offshore Vancouver Island. *Journal of Geophysical Research: Solid Earth, 107*(B9), EPM 5-1-EPM 5-16. doi: 10.1029/2001JB000269

Ritzmann, O., Jokat, W., Czuba, W., Guterch, A., Mjelde, R., & Nishimura, Y. (2004). A deep seismic transect from Hovgård Ridge to northwestern Svalbard across the continental-

ocean transition: A sheared margin study. *Geophysical Journal International, 157*(2), 683-702. doi: 10.1111/j.1365-246X.2004.02204.x

Ritzmann, O., Jokat, W., Mjelde, R., & Shimamura, H. (2002). Crustal structure between the Knipovich Ridge and the Van Mijenfjorden (Svalbard). *Marine Geophysical Researches, 23*(5-6), 379-401. doi: 10.1023/B:MARI.0000018168.89762.a4

Rumpfhhuber, E.-M. (2008). *An Integrated Analysis of Controlled- and Passive Source Seismic Data*: ProQuest.

Russel, B. H. (1988). *Introduction to Seismic Inversion Methods*: SEG Books.

Schlüter, H. U., & Hinz, K. (1978). The Continental Margin of West Spitsbergen. *Polarforschung, 48*(1/2), 151-169.

Selley, R. C. (1998). *Elements of Petroleum Geology* (Vol. 2): Gulf Professional Publishing.

Sheriff, R. E. (1991). *Encyclopedic Dictionary of Exploration Geophysics*.

Sleep, N. H., Meibom, A., Fridriksson, T., Coleman, R. G., & Bird, D. K. (2004). H2-rich fluids from serpentinization: Geochemical and biotic implications. *Proceedings of the National Academy of Sciences of the United States of America, 101*(35), 12818-12823. doi: 10.1073/pnas.0405289101

Smith, A. J., Mienert, J., Bünz, S., & Greinert, J. (2014). Thermogenic methane injection via bubble transport into the upper Arctic Ocean from the hydrate-charged Vestnesa Ridge, Svalbard. *Geochemistry, Geophysics, Geosystems, 15*(5), 1945-1959. doi: 10.1002/2013GC005179

Speight, J. G. (2010). *Handbook of Industrial Hydrocarbon Processes*: Elsevier Science.

Talwani, M., & Eldholm, O. (1977). Evolution of the Norwegian-Greenland Sea. *Geological Society of America Bulletin, 88*(7), 969-999. doi: 10.1130/0016-7606(1977)88<969:eotns>2.0.co;2

Thiede, J., Pfirman, S., Schenke, H.-W., & Reil, W. (1990). Bathymetry of Molloy Deep: Fram Strait between Svalbard and Greenland. *Marine Geophysical Researches, 12*(3), 197-214. doi: 10.1007/BF02266713

Upadhyay, S. K. (2013). *Seismic Reflection Processing: With Special Reference to Anisotropy*: Springer Science & Business Media.

Vanneste, M., Guidard, S., & Mienert, J. (2005). Bottom-simulating reflections and geothermal gradients across the western Svalbard margin. *Terra Nova, 17*(6), 510-516. doi: 10.1111/j.1365-3121.2005.00643.x

Vially, R. (1992). Bacterial Gas (pp. 242): Editions Technip.

Vincent, K. K., Muthama, M. N., & Muoki, S. N. (2014). Darcy¡¯s Law Equation with Application to Underground Seepage in Earth Dams in Calculation of the Amount of Seepage. *American Journal of Applied Mathematics and Statistics, 2*(3), 143-149.

White, R. S., McKenzie, D., & O'Nions, R. K. (1992). Oceanic crustal thickness from seismic measurements and rare earth element inversions. *Journal of Geophysical Research: Solid Earth, 97*(B13), 19683-19715. doi: 10.1029/92JB01749

Wiederhold, H. (2006). *Seismic methods - In: BurVal Working Group: Groundwater Resources in Buried Valleys- a Challenge for Geosciences*. Hannover: Leibniz Institute for Applied Geosciences.

References Cited

Yampol'skiy, K. P., & Sokolov, S. Y. (2012). Sedimentary cover and Bouguer anomalies in the northern part of the Knipovich ridge. *Doklady Earth Sciences, 442*(2), 188-192. doi: 10.1134/S1028334X12020109

Yilmaz, Ö. (2000). *Seismic Data Analysis: Processing, Inversion, and Interpretation of Seismic Data*: SOCIETY EXPLORATION GEOPHYSICISTS (OK).

Zayonchek, A. V., Sokolov, S. Y., Mazarovich, A. O., Ermakov, A. V., Razumovskii, A. A., Akhmedzyanov, V. R., . . . Yampol'skii, K. P. (2011). Structure of the transition zone between Hovgaard Ridge and Spitsbergen plateau according to the data obtained during cruise 27 of the RV Academik Nikolai Strakhov. *Doklady Earth Sciences, 439*(2), 1054-1059. doi: 10.1134/S1028334X11080101

Zhou, H.-W. (2014). *Practical Seismic Data Analysis*: Cambridge University Press, New York.

Zou, C. (2012). *Unconventional Petroleum Geology*: Elsevier Science.

Appendix

All results of the processing of the high-resolution 2D multichannel seismic data is shown below.

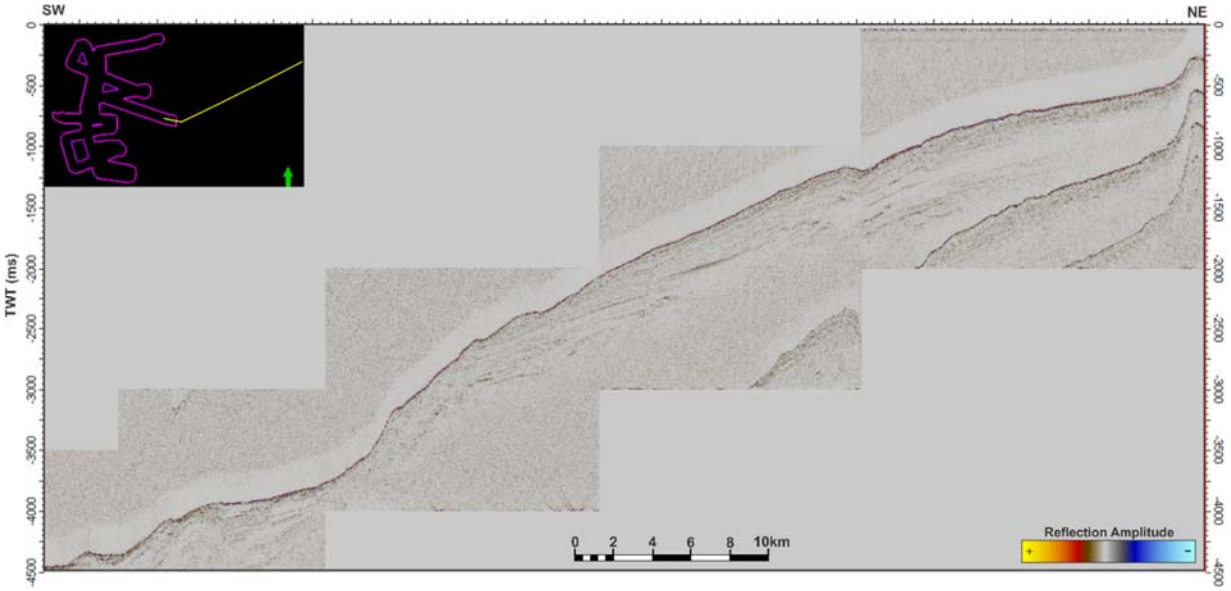

Figure A- 1. High-resolution seismic Line 1.

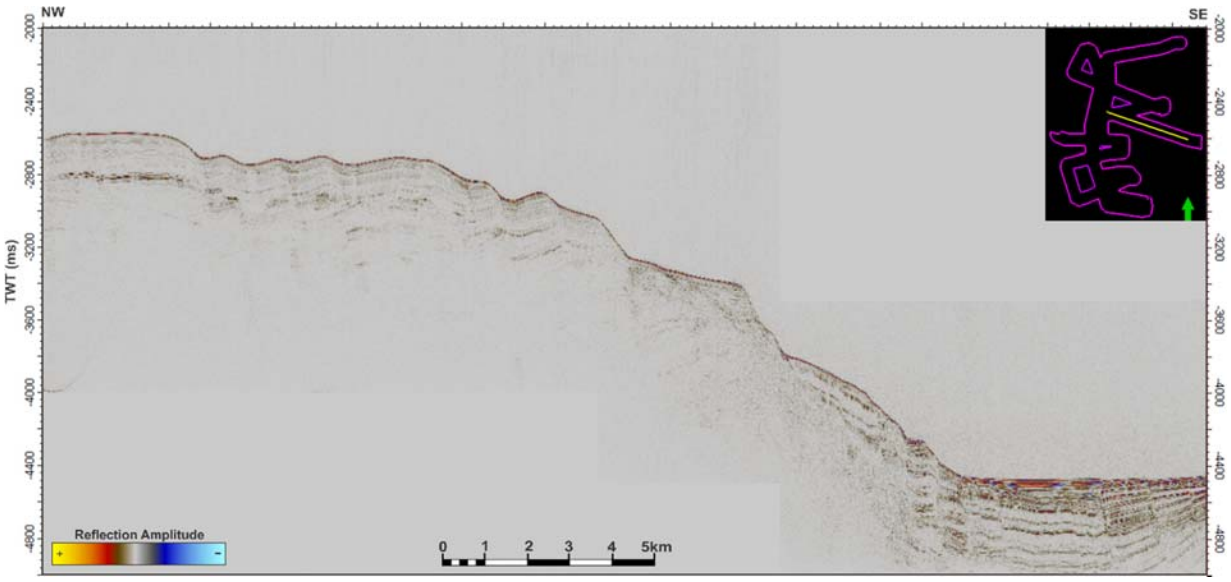

Figure A- 2. High-resolution seismic Line 2.

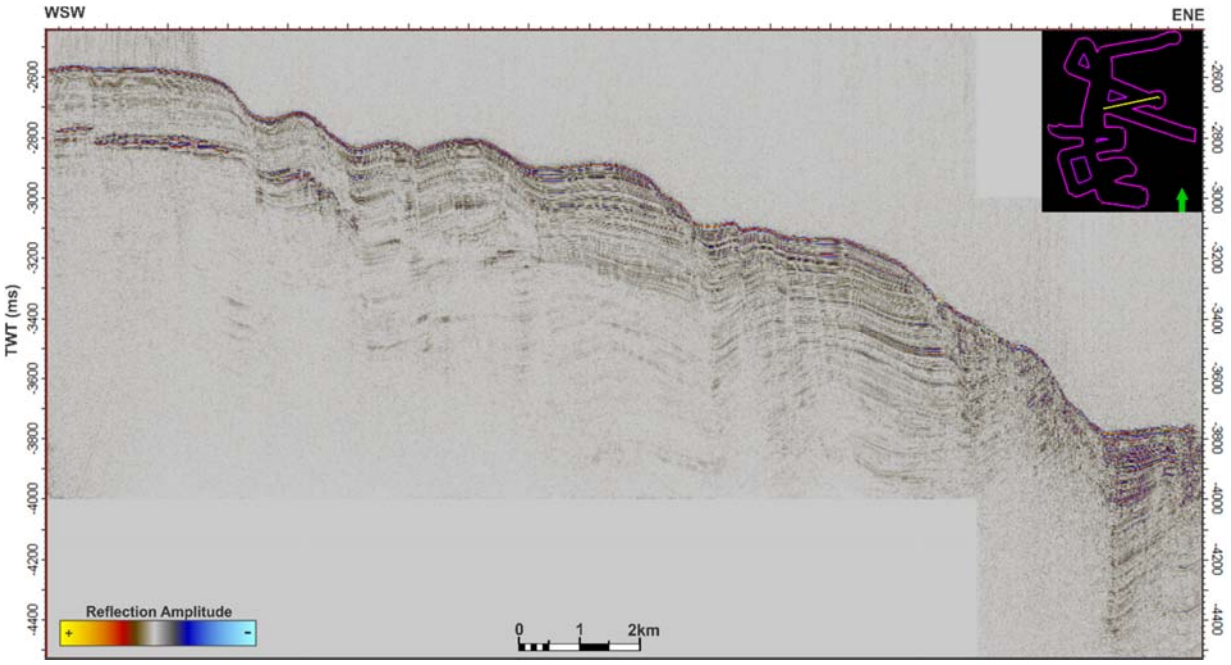

Figure A- 3. High-resolution seismic Line 3.

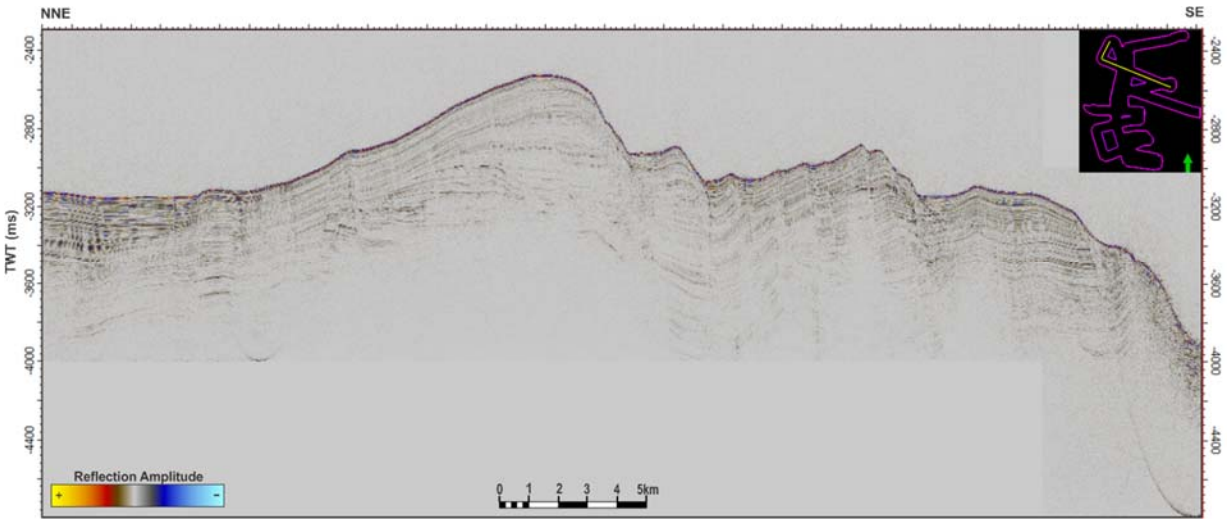

Figure A- 4. High-resolution seismic Line 4.

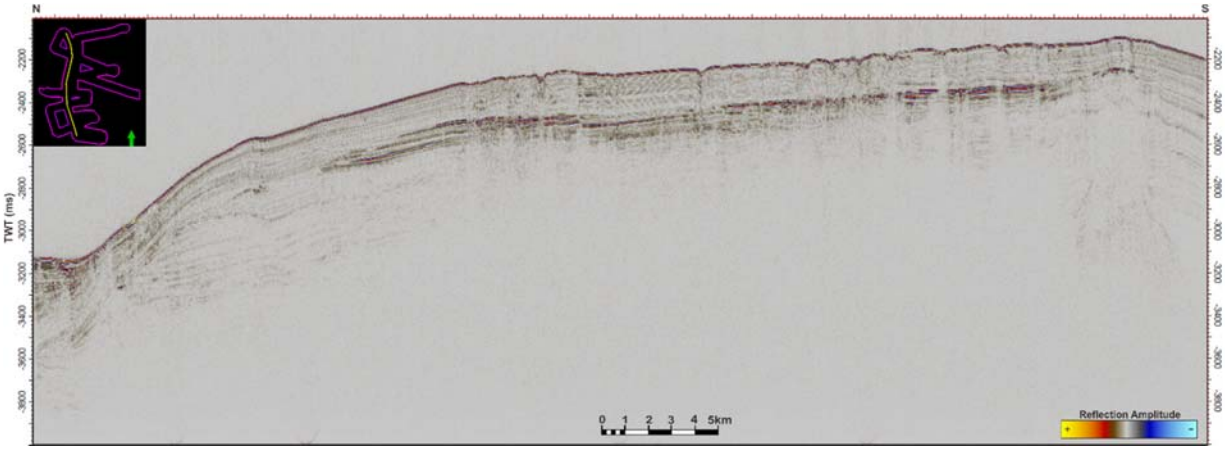

Figure A- 5. High-resolution seismic Line 5.

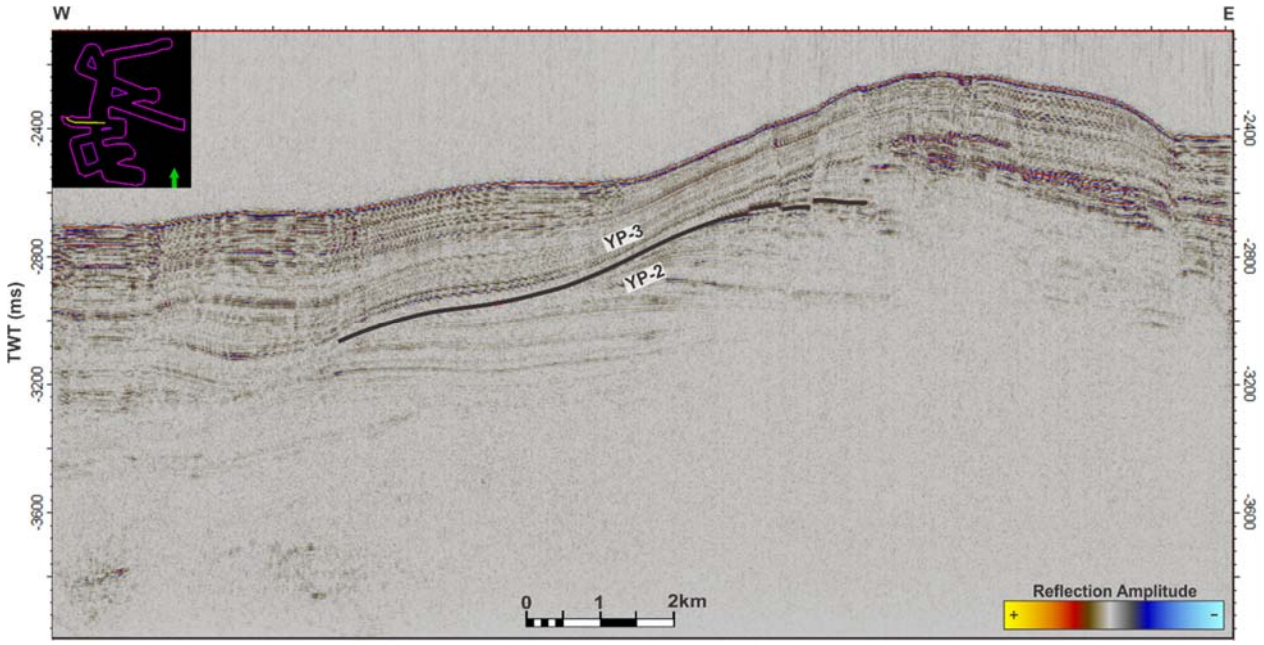

Figure A- 6. High-resolution seismic Line 6. Black line indicates the stratigraphic boundary YP-3/YP-2

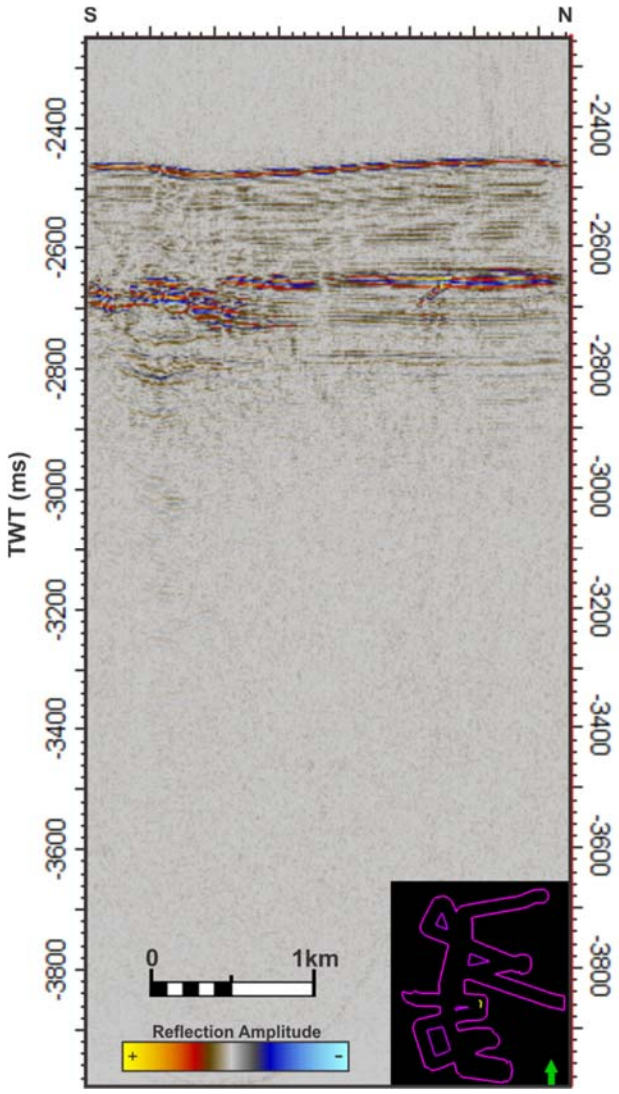

Figure A- 7. High-resolution seismic Line 7.

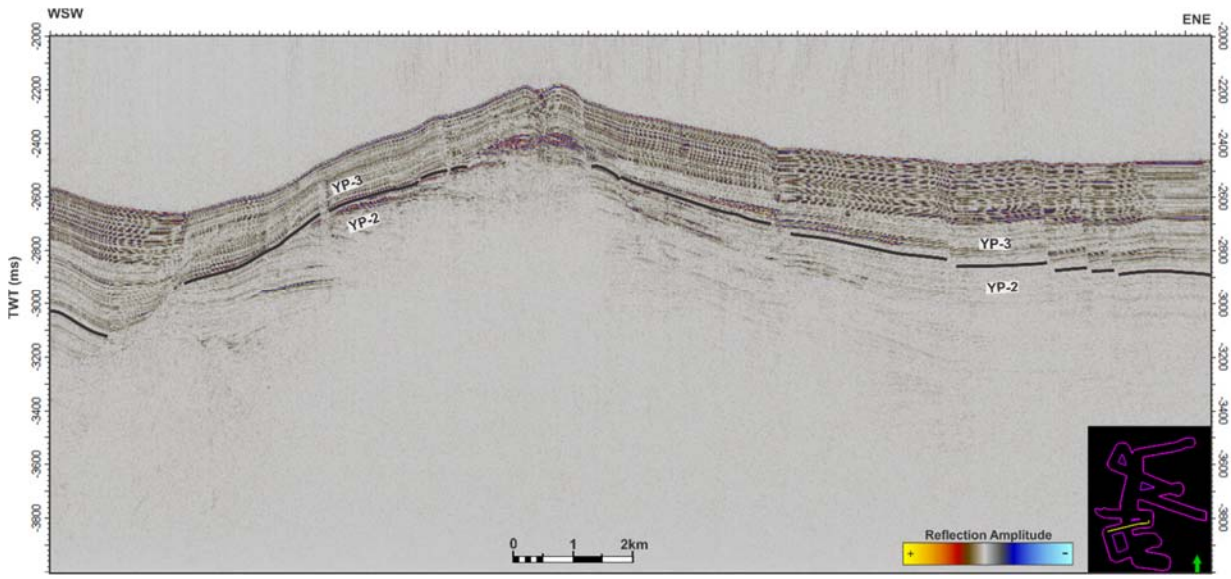

Figure A- 8. High-resolution seismic Line 8. Black line indicates the stratigraphic boundary YP-3/YP-2.

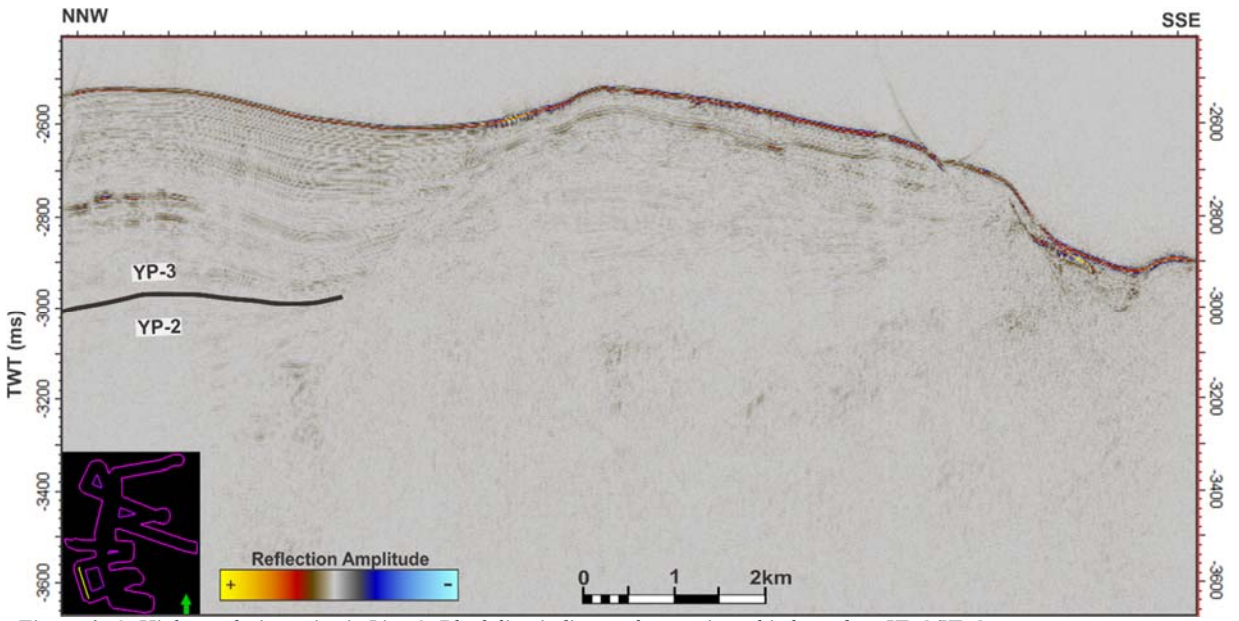

Figure A- 9. High-resolution seismic Line 9. Black line indicates the stratigraphic boundary YP-3/YP-2.

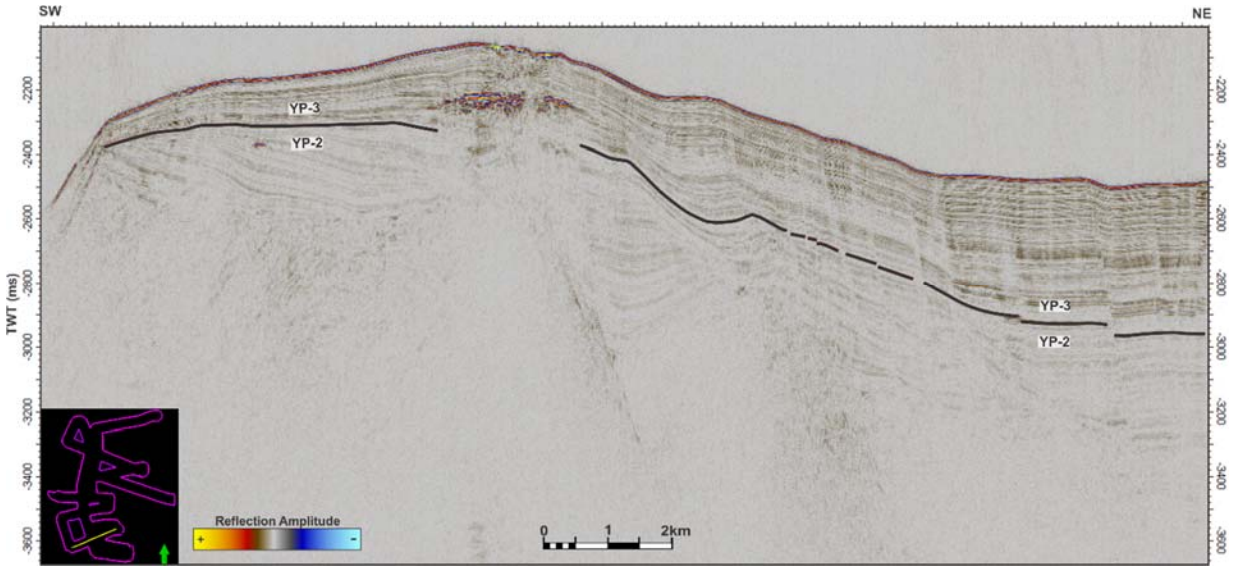

Figure A- 10. High-resolution seismic Line 10. Black line indicates the stratigraphic boundary YP-3/YP-2

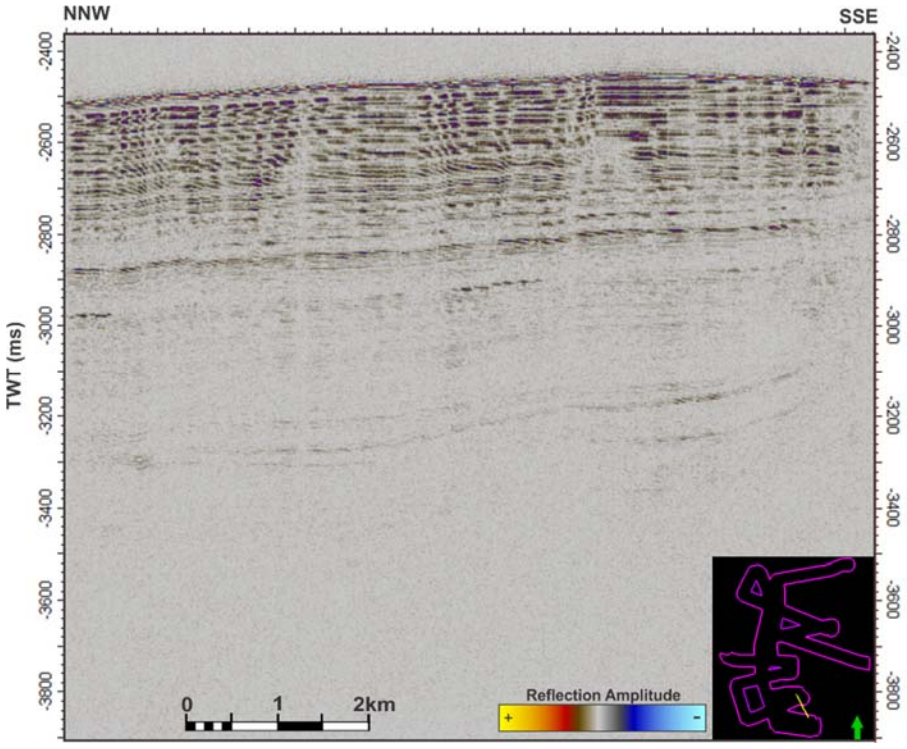

Figure A- 11. High-resolution seismic Line 11.

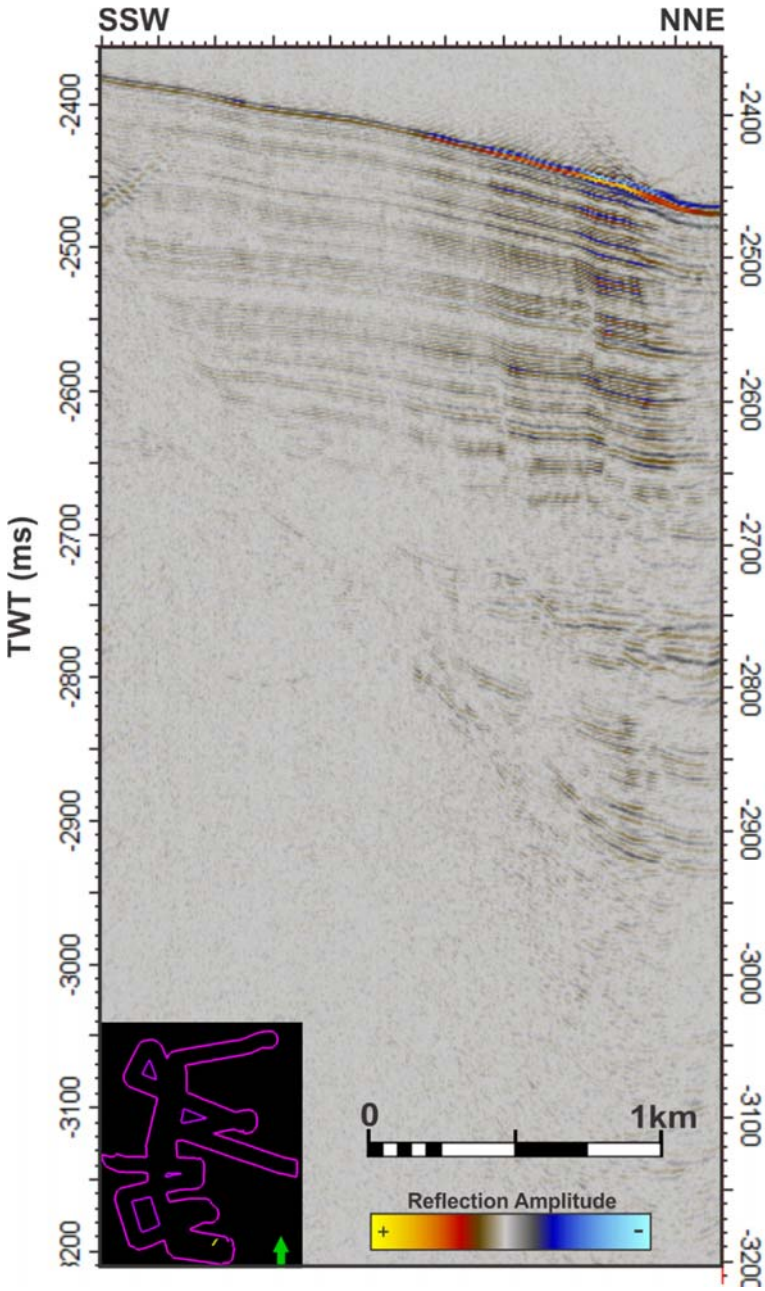

Figure A- 12. High-resolution seismic Line 11b

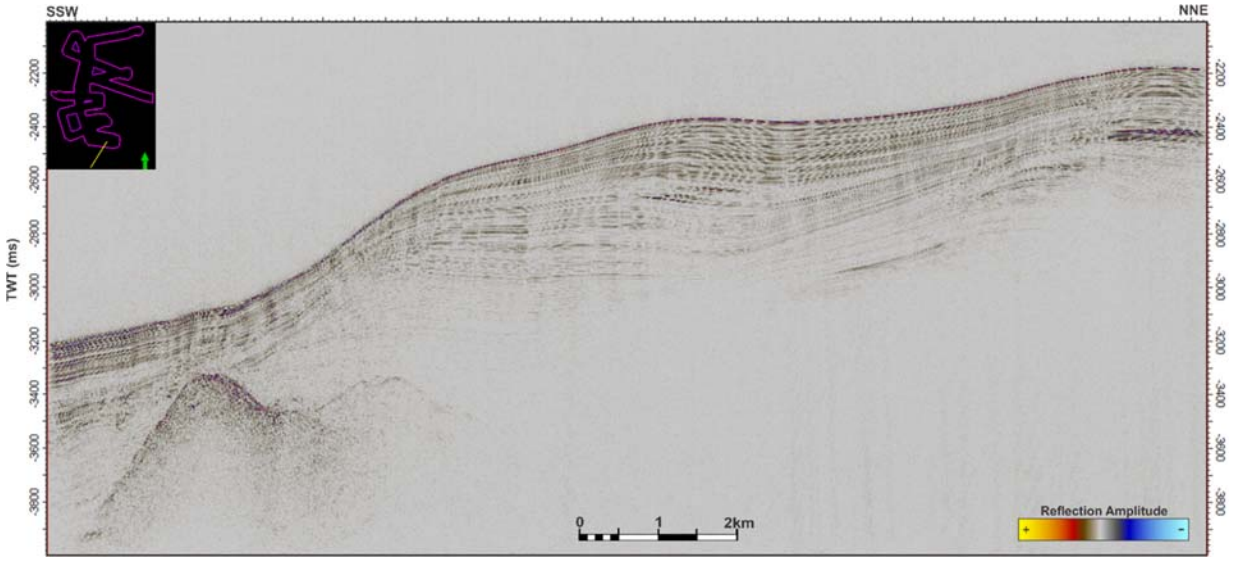

Figure A- 13. High-resolution seismic Line 11c